SYNTHESIS OF CALCIUM CARBIDE IN A PLASMA SPOUT FLUID BED

MUFTAH HASSAN EL-NAAS

Under the Supervision of Prof. R. J. Munz and Prof. F. Ajersch

Department of Chemical Engineering
McGill University

A Thesis Submitted to the Faculty of Graduate Studies
and Research in Partial Fulfilment of the
Requirements for the Degree of
Doctor of Philosophy

ISBN 0-612-19724-7

Canada

SYNTHESIS OF CALCIUM CARBIDE

IN A PLASMA

SPOUT FLUID BED

ABSTRACT

A new plasma fluid bed process to replace the present electric arc furnace for the production of calcium carbide has been studied. A thermodynamic analysis predicted that the solid phase reaction would be complete at 2150 K and that the plasma process could lower the energy consumption by up to 40%. A semi-batch fluid bed reactor with a DC plasma torch was used for the study. Calcium oxide powder with a mean particle size of 170 μm was reacted with two types of graphite, coke and methane. Argon was used to initiate the plasma and hydrogen gas was then added to increase the power and raise the plasma jet enthalpy. The hydrogen concentration in the plasma gas ranged from 33 to 67 (vol%).

The experimental results showed that the reaction took place in the plasma jet zone and that the conversion to calcium carbide increased linearly with reaction time. The rate of conversion increased exponentially with plasma jet temperature, indicating that chemical reaction was the controlling mechanism. The reaction rate was correlated to the shrinking core, reaction control model $1-(1-X)^{1/3} = Kt$ and showed excellent fit for conditions where hydrogen was present in the plasma gas. The apparent activation energy of the reaction was determined to be 377 kJ/mol (90 kcal/mol). Microscopic analysis of the solid product showed that calcium carbide was formed around both reactants. The surface area of the carbon was found to be an essential factor in determining the rate of formation of calcium carbide. Extrapolation of the reaction model and the experimental results indicated that complete conversion can be achieved within a reasonable time in a plasma fluid bed process. Thus, the new process is technically viable and also a more efficient alternative for the production of calcium carbide.

RÉSUMÉ

On a étudié un nouveau procédé de lit fluidizé à plasma pour la production du carbure de calcium afin de remplacer le procédé actuel utilisant une fournaise à arc électrique. Une analyse thermodynamique a prédit que la réaction en phase solide serait complète à 2150 K et que le procédé par plasma pourrait réduire de 40% la consommation d'énergie. Un réacteur à opération semi-intermittente à lit fluidizé équipé d'une torche à plasma à courant continu (DC) à été utilisé pour l'étude. De la poudre d'oxyde de calcium avec une taille de particules moyenne de 170 µm à réagit avec deux types de graphites, du coke et du methane. Le plasma à été initié avec de l'argon et par la suite, de l'hydrogène a été ajouté afin d'augmenter l'enthalpie du jet de plasma. La concentration d'hydrogène dans le gas plasmagène à été variée de 33 à 67 % (volume).

Les résultats expérimentaux ont démontré que la réaction se produisait dans la zone du jet de plasma et que la conversion en carbure de calcium augmentait de façon linéaire avec le temps de réaction. Le taux de conversion augmentait de manière exponentielle avec la température du jet de plasma, ce qui indique que la réaction chimique constituait le mécanisme de contrôle. Le modèle topochimique contrôlé par la réaction chimique représente le taux de reaction de manière excellente pour les conditions où l'hydrogène était ajoutée au gas plasmagène. L'énergie d'activation apparente de la réaction à été déterminée et sa valeur est de 377 kJ/mol (90 kcal/mol). Des analyses microscopiques du produit de la réaction en phase solide ont démontré que le carbure de calcium se situait

autour des particules des deux reactifs Il a été constaté que la surface spécifique du carbone est un facteur essentiel dans la détermination du taux de formation du carbure de calcium L'extrapolation du modèle réactionnel et des résultats expérimentaux indique qu'une conversion complète peut être obtenue dans des délais raisonnables par un procédé plasma à lit fluidizé, ce qui permet de croire que ce type de réacteur est une alternative techniquement viable et plus efficace pour la formation du carbure de calcium.

TO MY MOTHER AND TO MY WIFE

FOR INSPIRING, ENCOURAGING AND SUSTAINING

ACKNOWLEDGEMENTS

I would like to express my utmost appreciation and gratitude to those who contributed directly or indirectly to the completion of this work for their help and support.

I wish to thank my supervisors professor Richard Munz and professor Frank Ajersch for their invaluable guidance and continuous support. I would also like to thank all members of the plasma group, professor D. Berk, professor J.-L Meunier and my fellow graduate students in the group Antonio-Carlos, Jorg, Julie, Munther, Patrice, Sylvain and Tony for the useful suggestions and discussions, and for the friendship.

Thanks are due to Mr. Praveen Prasanna for kindly assisting with some experiments; to Mr. Glenn Poirier of the Department of Geological Sciences for helping with the Microprobe analysis; and to Mr. Slawomir Poplawski of the Department of Mining and Metallurgical Engineering for helping with the X-ray diffraction.

I would like to express my sincere thanks to the staff of the Chemical Engineering Workshop: Charles Dolan, Allen Gagnon and Walter Greenland for constructing and repairing parts of the experimental apparatus and for their valuable suggestions; to the Department of Chemical Engineering technicians: Mr. L. Cusmich, N. Habib, and E. Siliauskas for their technical help; to Mr. Jean Dumont of the Chemical Engineering Purchasing and Stores for making it easier to

find whatever is needed ; and to Pat Fong and Anne Prihoda of the Department of Chemical Engineering for their help and courtesy.

I am grateful for the help and encouragement that my family has always given me. I am deeply indebted to my wife, Mariam, for her patience, understanding and support throughout the ups and downs of this work.

The Road Not Taken

Robert Frost (1874-1963)

Two roads diverged in a yellow wood,
And sorry I could not travel both
And be one traveller, long I stood
And looked down one as far as I could
To where it bent in the undergrowth;

Then took the other, as just as fair,
And having perhaps the better claim,
Because it was grassy and wanted wear;
Though as for that, the passing there
Had worn them really about the same,

And both that morning equally lay
In leaves no step had trodden black.
Oh, I kept the first for another day!
Yet knowing how way leads on to way,
I doubted if I should ever come back.

I shall be telling this with a sigh
Somewhere ages and ages hence:
Two roads diverged in a wood, and I-
I took the one less travelled by,
And that has made all the difference.

TABLE OF CONTENTS

LIST OF FIGURES

LIST OF TABLES

NOMENCLATURE

Ar	Archimedes number $[d_P^3(\rho - \rho_f)\rho\, g/\mu^2]$.
A_S	Particle surface area (m^2).
Bi	Biot number (hL_C/k).
C_1,C_2	Constants in Equation (2.1).
C_P	Heat capacity of plasma gas (kJ/kg.K).
C_{pp}	Heat capacity of particles (mean heat capacity of bed materials, kJ/kg.K).
D	Pore diameter (μm) in Equation (3.2).
d_b, d_s	Diameter of big and small particles (m) in Equation (2.2).
d_{sv}	Surface volume diameter (m).
d_P	Particle diameter (m).
g	Acceleration due to gravity (m/s^2)
G	Gibbs free energy(J).
h	Plasma gas heat transfer coefficient ($W/m^2.K$)
H_J	Plasma net power (kJ/min).
k	Thermal conductivity (W/m.K)
K, K', K"	Global rate constants.
L	Plasma jet height (m).
L_C	Characteristic length (m).
M_G	Plasma gas flow rate (kg/min)
M_P	Particle circulation rate (kg/min).
Nu	Nusselt number (hd_P/k)
P	Applied pressure (psi) in Equation (3.2).
Q	Rate of heat transfer (W)
r	Reaction rate (mol/min).
R_1, R_2	Radii of particles with same conversion in Equation (5.13).
Re	Reynolds number ($d_P v_t \rho/\mu$).
Re_{mf}	Reynolds number at minimum fluidization ($d_P U_{mf} \rho/\mu$) .

t	Run time (s).
t_1, t_2	Reaction times needed for a given conversion in Equation (5.13).
T_B	Mean bed temperature (K).
T_G	Gas temperature in the jet zone (K).
t_h	Time needed for particles to reach T_I in the jet (s).
T_I	Temperature at the jet-bed interface (K).
T_J	Plasma gas temperature as it leaves the torch (K).
T_P	Mean particle temperature (K).
T_{pr}	Product temperature (K).
T_R	Mean reaction temperature (K)
U	Operating superficial velocity (m/s) in Equation (2.2).
U_{mf}	Minimum fluidization velocity (m/s).
$U_{mf(F)}$	Minimum fluidization velocity of floating particles (m/s) in Equation (2.2).
V	Particle volume (m^3) in Equation 7.1.
V_{atm}	Volume intruded at atmospheric pressure (ml/g)
V_B	Volume of the bed zone (m^3)
v_J	Plasma jet velocity (m/s)
V_J	Volume of the jet zone (m^3)
V_S	Sample volume (ml)
v_t	Particle terminal velocity (m/s).
V_t	Total volume intruded (ml/g)
W_S	Sample weight (g)
X	Fractional conversion
x	Fraction of heavy particles in the middle of the bed in Equation (2.2).

GREEK LETTERS

β	Proportionality constant (kg/kJ).
ΔHr	Heat of reaction (kJ/mol).

ε_c	Corrected porosity.
ε_B	Voidage in the bed zone.
ε_J	Voidage in the jet zone.
γ	Surface tension of mercury (dyne/cm) in Equation (3.2).
φ	Solid-mercury contact angle (130°) in Equation (3.2).
μ	Plasma gas viscosity (kg/m.s) at T_G
θ	Temperature difference (K)
ρ	Particle density (kg/m^3)
ρ_f	Plasma gas density (kg/m^3) at T_G
ρ_h, ρ_l	Densities of heavy and light material (kg/m^3) in Equation (2.2).
τ	Particle residence time in the jet (s)

CHAPTER ONE

"Study is like the heaven's glorious sun,
That will not be deep-search'd with saucy looks;
Small have continual plodders ever won,
Save base authority from others' books"

William Shakespeare (1564-1619)

CHAPTER I 1

GENERAL INTRODUCTION

Calcium carbide (CaC_2) is one of the most important high temperature carbides in use today. Its growing industrial applications in the desulphurization of steel and cast iron and in the production of acetylene have given it great importance as a chemical and further enhanced commercial interest in its production. When pure, calcium carbide is an odourless, colourless transparent solid. Commercial grade calcium carbide, however, is usually only about 80% CaC_2; the balance is calcium oxide, carbon and other impurities.

The synthesis of calcium carbide from calcium-zinc alloy and coal was first discovered in 1862 by Wohler. Industrial production of the material in electric arc furnaces was started about twenty years later in France by Moissan and independently in the United States by Morehead and Willson (Kampmann et al., 1985). The world annual production of calcium carbide increased from about 3.4 million metric tonnes in 1936 to 5.9 million tonnes in 1959 (Shine, 1978). This production rate declined in the late sixties when acetylene (for which calcium carbide was a major source) was replaced by ethylene in many chemical processes. However, calcium carbide is still the basis of the acetylene welding-gas industry. It is also used in the production of the fertilizer cyanamide as well as the desulphurization of steel. It is this last application that enhanced commercial interest in calcium carbide and made it an important industrial commodity nowadays, especially in countries with huge steel industries like the United States, Japan and Germany.

Presently calcium carbide is being produced by reacting carbon in the form of coke or charcoal and calcium oxide in the form of lime in large electric arc furnaces at temperatures ranging from 2300 to 2500 K It is believed that the reaction takes place in the liquid phase when calcium oxide, which is dissolved in the melt, diffuses through the surface of the carbon resulting in liquid calcium carbide. The molten product is tapped from the furnace at about 2073 K, cooled, cast and then crushed and ground to the size required for marketing.

A plasma spout fluid bed process has been studied as a replacement of the present process. In this new process, a plasma spout-fluid bed reactor is used instead of an electric arc furnace. The reaction between carbon and calcium oxide takes place in the solid phase at about 2150 K, resulting in a lower energy consumption. The good mixing characteristic of the spout-fluid bed and the confinement of the high temperature plasma within the bed improves heat transfer between the reactants leading to more efficient heating. Also, the sensible heat of the products can be recovered to heat the reactants and hence lower the energy requirements.

The overall objective of the present research project was to study the feasibility of the solid phase formation of calcium carbide in a plasma spout-fluid bed reactor. Included in the study were an investigation of the reaction mechanism and product morphology, the determination of the rate controlling mechanism(s) and the examination of the effect of carbon source and reactivity on the rate of formation of calcium carbide. A semi-batch fluid bed reactor with a DC plasma torch was used for the study. High calcium quicklime was used as a source of

calcium oxide and was reacted with two types of graphite powder, coke powder, and methane.

This thesis was written to be as concise as possible, without compromising the clarity of the presentation. It is divided into eight chapters. A general review of the literature relating to plasma, fluidization and the formation of calcium carbide is given in the second chapter. The third chapter presents a detailed description of the experimental apparatus, procedures and analytical techniques. A thermodynamic analysis of the reactions of calcium oxide and carbon is discussed in Chapter Four, while experimental results are presented and discussed in Chapters Five and Six. Theoretical interpretation and modelling of the results is given in Chapter Seven; and finally conclusions, recommendations and contributions to knowledge are presented in the last chapter.

CHAPTER TWO

"We dance round in a ring and suppose;
But the secret sits in the middle and Knows"

Robert Frost (1874-1963)

CHAPTER II 2

LITERATURE REVIEW

2.1 INTRODUCTION

Plasma processing and synthesis of materials has become a dynamic field of research in the past two decades. The high energy associated with plasma has given it several advantages over traditional processes, since it results in faster reactions and faster physical transformations and therefore higher throughput using smaller equipment. Also, the use of electrical energy for heating allows the separation of process energy and chemistry. The difficulties in plasma-solid reactions have usually been the contacting techniques between the ionized plasma gas and the solid reactants. Plasma fluidized and plasma spouted beds have shown good success in eliminating such difficulties. Plasma spouted and fluidized beds can serve as excellent reactors for gas-solid and solid-solid reactions, since they combine the advantages of plasma: high energy source and transfer medium and a source of reactive intermediates and the advantages of fluidized and spouted beds: good mixing and the fluidity of the bed.

In this literature review, some applications of plasma spouted and/or fluidized beds are discussed. Also the application of plasma in the production of calcium carbide as well as the kinetics of the formation of calcium carbide are reviewed.

2.2 PLASMA AND PLASMA PROCESSES

Plasma history can be traced back to the early studies of discharges in gases in the late nineteenth century. In 1879, William Crookes noticed that gases under electric discharge (ionized gases) possessed unusual physical and chemical properties. This led him to suggest that those gases can be regarded as a fourth state of matter (McTaggart, 1967). In 1928, Langmuir was the first to use the word "plasma" to denote ionized gases.

Plasma is now known as an ionized gas containing molecules, atoms, ions, electrons and photons (Fauchais et al, 1987). The negative and positive charges in plasma are approximately equal making it neutral overall. Plasma can be divided into two different types: thermal or equilibrium plasma and non-thermal or non-equilibrium plasma. In thermal plasmas, the electron temperature is approximately equal to the temperature of the heavy particles. In non-thermal plasmas, the electron temperature is much higher than that of the heavy particles. In some literature these two types are referred to as hot and cold plasmas respectively. Hot or thermal plasmas are formed at atmospheric or higher pressures. Plasmas produced in spray torches, radio frequency inductive torches, and electric arcs are typical examples of hot plasmas. Cold plasmas are formed under reduced pressure; examples of this type include plasmas produced in glow discharges and in corona discharges.

2.2.1 Plasma Processes

Plasmas have been applied to mechanical processes such as welding, cutting and spraying; metallurgical processes such as the production of alloys and the making of refractory materials;

and chemical processes such as the synthesis of acetylene, nitrogen oxides and phosphates as well as the production of new ceramics (Labort et al, 1981). Plasma processes have several advantages over traditional processes due to the high energy associated with plasma, which results in faster reactions and allows the possibility of making new products such as high temperature ultra fine ceramics.

2.2.2 Plasma Generators

Plasma may be generated by applying a high frequency high voltage electric field to a gas. Plasma generating devices can be classified as having electrodes or being electrodeless. Electrode devices (sometimes called thermal or plasma arcs) are characterized by the presence of a cathode and an anode. Transferred arcs and non-transferred arcs are the only two types of thermal arcs. Further details about electrode devices can be found in the works of Mehmetoglu (1980) and Patterson (1983). Electrodeless devices, on the other hand, do not have electrodes, and the plasma is initiated either by capacitive or inductive coupling. A high frequency electric field is used to maintain the discharge in capacitive coupling, whereas in inductive coupling, the discharge is maintained by a time-varying magnetic field. For more details about these devices, readers are referred to the works of Munz (1974), Sayegh (1977), Biceroglu (1978) and Pfender et al (1987).

2.3 FLUIDIZATION

Fluidization is the operation by which a bed of solids is transformed into fluidlike state through contacting with a fluid. This is achieved by the passing of a fluid upward through

a bed of fine particles. As the fluid velocity is increased, the pressure across the bed increases until it reaches a point where it balances the weight of the solids, and all particles become suspended in the upward fluid. This is known as incipient or minimum fluidization, and the fluid velocity at that point is called minimum fluidization velocity. At a higher velocity, bubbles appear in the bed; this fluid velocity is referred to as minimum bubbling velocity. The state or the regime of fluidization depends mainly on the properties of both the solid and the fluid. Liquid-Solid and Gas-Solid systems generally behave differently. In Liquid Solid systems, a liquid flow rate above minimum fluidization results in a smooth progressive expansion of the bed. This type of beds is referred to as a particulate fluidized bed, a homogeneously fluidized bed, a smoothly fluidized bed or simply a liquid fluidized bed. While in Gas-Solid systems, an increase in gas flow rate beyond minimum fluidization leads to instabilities with bubbling and channeling of the gas. At higher flow rates, fluidization becomes more violent and the movement of solids becomes more vigorous. This type of bed is referred to as an aggregative fluidized bed, a heterogeneously fluidized bed, a bubbling fluidized bed or simply a gas fluidized bed (Kunii and Levenspiel, 1969).

2.3.1 Effect of Solid Properties on Fluidization

Particle size and density play an important role in determining fluidization regimes. Geldart (1973) reported that the behaviour of solids fluidized by gases fell into four distinguishable groups, categorized by density difference (ρ_S - ρ_f) and mean particle size as shown in Figure 2.1 for air at ambient conditions. The first group (A) includes materials having a small mean particle size and/or low density (less than 1.4 g/cm^3). Beds of materials in this

group expand considerably before bubbling commences, and when the gas supply is suddenly cut off, the bed collapses slowly. Bubbles in a two-dimensional bed appear to split and recoalesce frequently, and all bubbles rise more rapidly than the interstitial gas velocity. Geldart proposed that for a material to belong to group A (for air fluidization at ambient conditions), the criterion $(\rho_S - \rho_f)d_p \leq 225$ must be satisfied (ρ_S, ρ_f in g/cm^3 and d_p in μm).

The second group (B) contains most materials in the mean particle size and density ranges 40 μm < d_p < 500 μm, 4 g/cm^3 > ρ_S > 1.4 g/cm^3. A bed of material in this group starts bubbling at or slightly above minimum fluidization. Bed expansion is small, and the bed collapses quickly when the gas supply is cut off. Bubbles rise faster than the interstitial gas velocity and bubble size increases linearly with bed height and excess velocity. The third group (C) contains materials which are cohesive. Powders of this type are extremely difficult to fluidize. This difficulty is believed to arise because the interparticle forces are greater than those which the fluid can exert on the particles. Very small particle size, strong electrostatic charges or the presence of wet material in the bed may lead to this kind of difficulty in fluidization.

The fourth group (D) includes material of large particle size and/or high density. Gas flow around solid particles in this group may be turbulent, leading to particle attrition as well as elutriation of the fines produced. This group of material is suitable for spouting. The criterion suggested by Geldart for this group is $(\rho_S - \rho_f)(d_p)^2 \geq 106$.

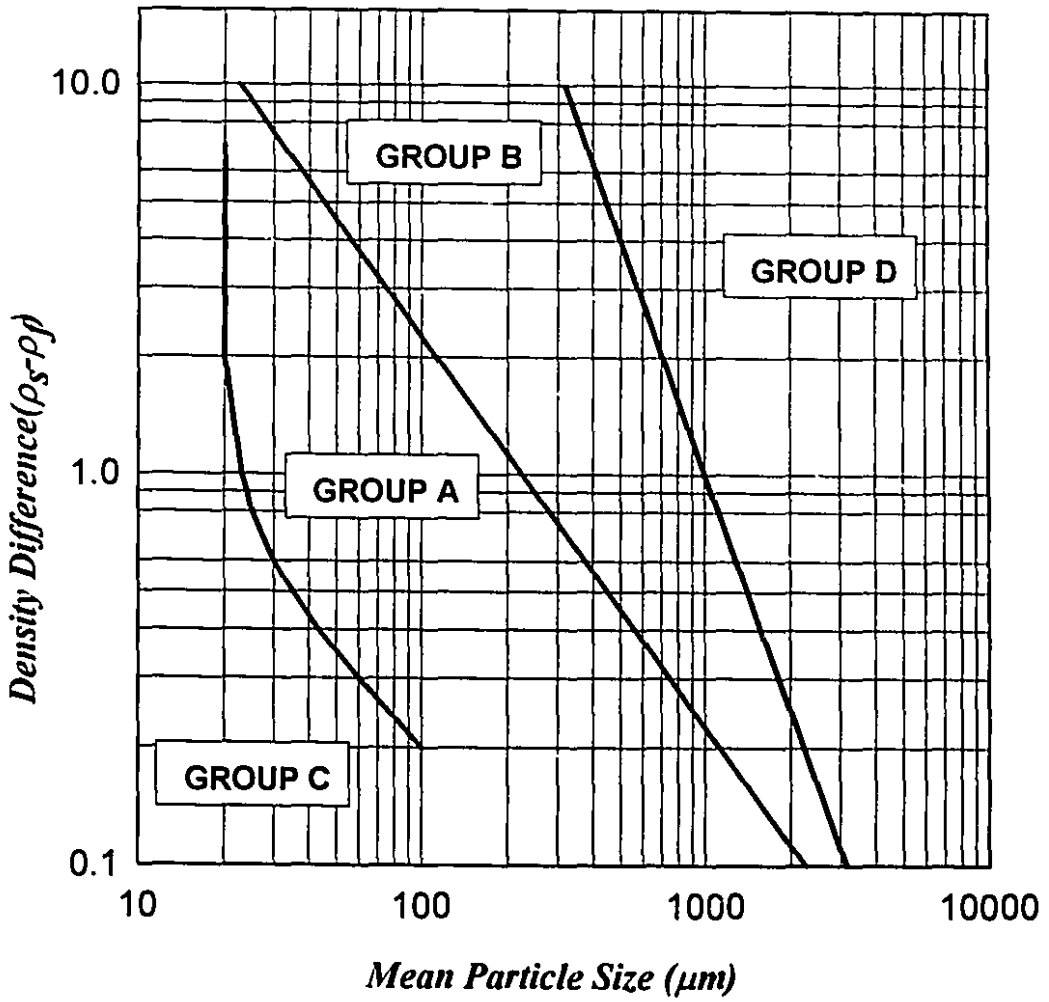

Figure 2.1: Classification of the fluidization characteristics of powders (Geldart, 1973).

2.3.2 Effect of Temperature on Fluidization

The effect of temperature on the behaviour of fluidized and spouted beds has been investigated by many researchers, Mii et al. (1973), Pattipati et al. (1981), Stubington et al. (1984), Nakamura et al (1985), Bin (1985), Bin (1986) and Ye et al. (1992). Mii et al. (1973) reported that an increase in a fluid bed temperature increased the frequency of bubble formation and decreased bed viscosity, resulting in an increase in the fluidity of the bed. Ye et al. (1992) studied the effect of temperature on the hydrodynamics of spouted and spout-fluid bed at temperatures up to 1153 K. They reported that the minimum spouting velocity increased with increasing temperature for large particles and decreased for small particles. Nakamura et al (1985) pointed out that the effect of temperature on the minimum fluidization velocity was only significant for low Re_{mf}, where viscous forces are dominant. U_{mf} is inversely proportional to viscosity, and since viscosity increases with temperature, U_{mf} steadily decreases with temperature, especially for fine particles. The researchers found that most correlations gave reasonable predictions of the minimum fluidization velocity. Several correlations are available in the literature for predicting U_{mf}. The following equation was used by Ye et al. (1992) to estimate the minimum fluidization velocity:

$$Re_{mf} = (C_1^2 + Ar\, C_2)^{0.5} - C_1 \qquad (2.1)$$

This equation was used to estimate the minimum fluidization velocity in the present study, using the same values for C_1 and C_2 as those used by Ye et al. (1992) and recommended by Grace (1982): $C_1 = 27.2$ and $C_2 = 0.0408$.

2.3.3 Mixing in Fluidized beds

Although good mixing is one of the main advantages of fluidized beds, one of the major problems in solid reactions carried out in fluidized beds is segregation of particles. Mixing of solids in a fluidized bed depends largely on particle size, particle density and fluidization velocity. Several researchers have studied mixing and segregation in fluidized beds. Rowe et al. (1972a) studied the importance of particle size and density in segregation of particles. They examined a mixture of heavy small particles and light big particles; all particles were chosen so as to have same minimum fluidization velocity. The study showed that for velocity slightly higher than minimum fluidization velocity, segregation occurred with the heavy particles sinking to the bottom. A concentration of these heavy particles, however, was found in the top layer of the bed; such concentration increased with increasing the fluidization velocity leading to good mixing. An important conclusion of this study was that the most important mechanism was the lifting of particles in the enclosed wake of rising bubbles.

In a further study, Rowe et al. (1972b) proposed a mechanism and derived a model to predict the fraction of heavy particles in the middle section of the bed when equilibrium is reached. The fraction is given by the following expression:

$$x = f(U - U_{mf(F)}).(\rho_h/\rho_l)^{-2.5}.(d_b/d_s)^{-1.5} \qquad (2.2)$$

where,

x = the fraction of heavy particles in the middle section of the bed.

U = the operating superficial velocity.

$U_{mf(F)}$ = the minimum fluidization velocity of the floating particles.

ρ_h, ρ_l = the densities of heavy and light material.

d_b, d_s = the diameter of big and small particles.

The model predicts a stronger influence of density than particle size. The effect of particle shape on segregation was studied by Nienow and Cheesman (1980) and found to be minor relative to that of density. The value of the excess velocity function f in Equation (2.2), was not determined but could be approximated by a linear function such as ($U - U_{mf}$) for low values. The model was applied by Tuot (1976) to predict the state of mixing in a thermoelectrical fluidized bed used to study the production of titanium carbide at 2000 K. The fraction x predicted by the model was 5.02E0-4, indicating poor mixing or segregation. This prediction was in complete contrast with the good mixing achieved experimentally by Tuot. The disagreement was believed to be due to several factors, including the nature of the gas and the shape of the particles. Tuot considered the use of the velocity excess to be the main weakness of the model, because it was unsuitable for high temperature fluidization. As temperature is increased, the minimum fluidization velocity is decreased by a considerable factor, making any reference to excess velocity inappropriate. Also, the model neglected the effect of temperature on the size and the frequency of formation of bubbles, which played an important role in mixing as reported by Rowe et al. (1972a). Tuot (1976) and others (Mii et al., 1973) reported that the size of bubbles decreased with increasing temperature, leading to a higher frequency of bubble

formation and more mixing. The similarity between the system studied by Tuot (1976) and that under study in the present work suggested that good mixing could be expected.

2.4 PLASMA SPOUTED AND FLUIDIZED BEDS

The study of plasma fluidized beds started as early as the 1960's. Goldberger and Oxley (1963) used a fluidized bed to quench plasma reactions. The bed used was a double-walled glass column about 5 cm in internal diameter. A DC motor generator (5 kW) was used to generate the plasma. The plasma formed was injected through the bottom of the column vertically into the bed of fluidized solids. The study found that at steady operation, the measured temperature at any point in the fluidized bed , with the exception of the centre line temperature, fluctuated less than 2 K. The temperature deviation within the bed became more pronounced as the plasma flow rate was increased. There was only limited lateral mixing and less heat transfer from the centre to the wall at higher plasma rates. Deeper beds were found to increase heat transfer from the plasma and hence cause a more uniform temperature distribution in the bed.

Wierenga and Morin (1988) characterized a fluidized bed plasma reactor. The reactor was a double-walled Pyrex glass column 54cm in length and 20 mm in internal diameter. The bed of solids (glass beads 0.17 to 3 mm in diameter) was fluidized at subatmospheric conditions (100 to 6600 Pa) in a resonantly sustained high frequency microwave (2.45 GHz) plasma. The researchers noticed the presence of glowing bubbles in the fluidized bed; they also reported that the centreline temperature of the bed became high enough to melt the glass beads and fuse them together. The bed behaviour was a function of power level, pressure, flow rate, particle

diameter and fluidizing gas. It was found in the study that the main difference between the plasma fluidized bed and the conventional fluidized bed was the dependence of the minimum fluidization velocity on bed temperature. This velocity increased as the plasma temperature was increased. This difference was believed to be due to the interparticle forces which were enhanced by heat softening and adhesion of the glass beads. The enhancement was also believed to be an electromagnetic effect.

A similar study by Rogers and Morin (1991) using the same apparatus showed that in the presence of plasma, nonideal behaviour occurred more frequently due to the uneven temperature profile. Also, the measured pressure drop was greater than the calculated pressure drop required to raise the bed. They also noted that high-frequency, resonantly sustained plasma could influence fluidization through both thermal and electromagnetic effects. In both studies, the researchers did not separate the thermal and the electromagnetic effects. They did not show whether fluidization was affected most by thermal or electromagnetic effect. Thus, other plasma fluidized beds (using other forms of plasma) may show totally different behaviour from those reported by the two studies.

Okubo et al. (1990) used a plasma fluidized bed for the nitriding of titanium particles, ranging in size from 46 to 74 μm. The fluidized bed used was a quartz tube 750 mm in length and 27.5 mm in internal diameter. Radio frequency power (13.56 MHz) was applied from a 500 W crystal-controlled generator. The discharge coil was wound outside the reactor 50 mm above the static bed. Argon and nitrogen were used to fluidize the bed at 100 Pa. The researchers did

not see any change in the state of fluidization due the presence of plasma. The nitriding rate, however, was higher in the presence of plasma than in the conventional thermal reaction.

A study of a plasma spouted bed reactor was carried out by Jurewicz et al. (1985). Alumina particles, ranging in size from 53 to 1000 microns, were spouted in Ar and Ar/N_2 plasma. The reactor was a cylindrical Pyrex tube 168 mm in internal diameter and about a meter in length; this was connected to a conical Pyrex section 160 mm in length. The smaller diameter of the cone was connected, through a 70 mm ID Pyrex tube, to a water-cooled conical brass adapter which housed the anode part of the DC plasma torch. The researchers measured bed temperature, bed stability and particle attrition. They found that those parameters depended on particle size, plasma power, plasma gas composition and volume of the bed. Temperature inside the bed was uniform due to the high level of particle recirculation. A substantial decrease in mean particle size was observed after only ten minutes of spouting in an Ar/N_2 plasma at 28 kW. Bed stability was found to decrease as powder loading was increased beyond 2100 g.

Hydrodynamics and heat transfer in a plasma spouted bed were studied by Flamant (1990). He spouted alumina particles (0.4 to 2.36 mm) with an argon plasma in a 90 mm column at bed temperatures ranging from 573 to 1473 K. The study showed that radial temperature differences were large, while the axial temperature gradients were small; this indicated efficient axial mixing due to the plasma jet but poor mixing in the annulus. Also, the plasma-to-particle

heat transfer efficiency reached values higher than 90% due to the plasma jet confinement inside the bed.

Munz and Mersereau (1990) studied the calcination of vanadium ore concentrate in a plasma spout-fluid bed. They used a 20-kW DC plasma torch with nitrogen and argon as the plasma gases. The study showed that heating and reaction in the reactor occurred primarily as particles passed through the plasma spout. Melting and agglomeration of the particles occurred at high temperature, leading to the destabilization of the bed. A thorough review of different designs of plasma spouted and fluidized bed reactors was presented by Flamant (1993).

2.5 GAS-SOLID AND SOLID-SOLID REACTIONS

Gas-solid and solid-solid reactions include catalytic and non-catalytic reactions. Only non-catalytic reactions will be considered in this review. Non-catalytic gas-solid reactions can be divided into four groups (Wen, 1968):

A- Solid reactant → gas product

B- Solid reactants → gas and solid products

C- Gas and solid reactants → gas products

D- Gas and solid reactants → gas and solid products

Examples of industrially important reactions from these four groups can be found in the work of Doraiswamy and Sharma (1984). The reaction between calcium oxide and carbon belongs to the second group (B), where solid reactants result in the formation of gas and solid

products. Solid-solid reactions usually proceed through gaseous intermediates as in the case of the carbon reduction of metal oxides. An extended review of the various aspects of solid-solid reaction have been given by Tamhankar and Doraiswamy (1979).

2.5.1 Reduction of Metal Oxides

The direct reduction of metal oxides by solid carbon has been studied by numerous researchers; Bodensein (1927); Baldwin(1955); Sharma et al. (1957); Otsuka and Kunii (1969); Rao (1971); Rao (1974); Ajersch (1987); Munz and Chin (1991); and Munz and Chin (1992). It is believed that the reduction takes place through the gaseous intermediates carbon monoxide and carbon dioxide in accordance with the following two gas-solid reactions (Szekely et al., 1976):

$$MeO_n + CO = Me + nCO_2 \qquad (2.3)$$

$$CO_2 + C = 2CO \qquad (2.4)$$

Carbon must pass through the intermediate stage of carbon monoxide before reacting with the metal oxide. It is not known, however, how carbon monoxide is generated in the first place. The regeneration of carbon monoxide according to the Boudouard reaction (2.4) is considered to be the rate controlling step.

2.6 PRODUCTION OF CALCIUM CARBIDE USING PLASMA

Calcium carbide is presently produced in electric arc furnaces by reacting calcium oxide and coke at about 2400 K. The molten product contains about 80% calcium carbide with the balance being calcium oxide, carbon and other impurities. Typical analyses of reactants and the

product are given in Tables 2.1, 2.2 and 2.3 (Kampmann et al, 1985). A typical electric arc furnace operation requires about 4 kWh/kg CaC_2. Several patents, aiming at developing a more efficient process, have been granted for the production of calcium carbide using different furnace designs and different heating mechanisms. In the past decade, seven patents have used plasma as a heat source. Baba and Shohata (1988) patented a process for the production of calcium carbide micropowders using high frequency plasma. A mixture of calcium oxide and carbon is introduced into a plasma flame to produce calcium carbide powder with a uniform grain size of about 0.1 micrometer. Although there was no mention of the energy consumption in the patent abstract, one would expect a high energy consumption due to the low efficiency of high frequency plasma. Another patent using high frequency plasma was granted to Eriksson (1983). Lime with a particle size of less than 2 mm and powdered carbon in a carrier gas of H_2 and CO were injected into an induction plasma furnace. The product was 78% calcium carbide, and the energy consumption was 6 kWh/kg CaC_2. This energy consumption is much higher than that required for a typical electric arc furnace (about 4.0 kWh/kg). In a recent study, Zhu et al (1995), investigated the formation of calcium carbide in a plasma-heated fluid bed by reacted pelletized stoichiometric mixture (3C : 1 CaO) of lime and anthracite (2 mm in diameter) with a grain size of 0.2 mm at an operating temperature of 1673-1723 K and a pressure of 1 atm. The researchers reported a conversion of up to 84%, but did not explain how the reaction rate was measured and what mechanism was controlling the rate of reaction. The calcium carbide produced was described as a good quality carbide.

Table 2.1: Typical Composition of Carbon Used in the Production of Calcium Carbide (wt%).

CARBON[1]	*Metallurgical coke*	*Anthracite*
Non-volatile	89.0	80.0
Volatile	0.8	6.0
H_2O	0.8	8.0
S	0.8	0.8
Ash	9.4	6.0

1 Grain size 3-25 mm.

Table 2.2: Typical Composition of Lime Used in the Production of Calcium Carbide (wt%).

LIME (CaO)[2]	*New lime*	*Recycled lime*[3]
Total CaO	93.8	89.0
Free CaO	93.6	-
$CaSO_4$	0.4	-
SiO_2	1.3	2.9
Fe_2O_3	0.4	0.4
Al_2O_3	0.5	2.4
MgO	0.8	0.8
CO_2	2.7	3.0
P_2O_5	0.015	0.01

2 Grain size 6-50 mm.
3 Recycled $Ca(OH)_2$ after acetylene generation

Table 2.3: Typical Analysis of Calcium Carbide (wt%).

COMPONENT	*Wt %*
CaC_2	80.5
CaO	12.9
Si	1.3
Al	1.1
Fe	0.2
S	0.5
C	0.3

2.7 REACTIONS OF CALCIUM CARBIDE

There are three important reactions which are the bases of the main industrial applications of calcium carbide. The first is the highly exothermic hydrolysis of calcium carbide to form acetylene.

$$CaC_2 + 2H_2O = C_2H_2 + Ca(OH)_2 \qquad (2.5)$$

In this reaction, excess water is needed for the heat of reaction to be safely absorbed; limited quantities of water may lead to explosive conditions (Shine, 1978). This hygroscopic property of calcium carbide can be utilized to determine the water content in pyrolysis gases (Lindblom et al., 1992). The second important reaction is that of calcium carbide with sulphur:

$$CaC_2 + S = CaS + 2C \qquad (2.6)$$

This reaction is the basis of the application of calcium carbide in steel desulphurization. Fine particles of calcium carbide are injected into a ladle or a torpedo car to react with the sulphur present in the molten metal. A small particle size is essential for this reaction, providing a large surface area to react quickly with sulphur. The sulphur content of steel can be reduced from 0.02 to 0.005% (Kampmann et al., 1985).

The third reaction is that of calcium carbide with nitrogen to produce the fertilizer calcium cyanamide:

$$CaC_2 + N_2 = CaCN_2 + C \qquad (2.7)$$

Nitrogen gas is passed over finely ground calcium carbide and reacted at about 1273 K. Cyanamide also reacts with carbon to produce calcium cyanide, which is used for gold refining.

2.8 KINETICS OF THE FORMATION OF CALCIUM CARBIDE

Calcium carbide is generally formed according to the following overall reaction:

$$CaO + 3C = CaC_2 + CO \qquad (2.8)$$

Tagawa and Sugawara (1962) studied the kinetics of the above reaction in the solid phase at temperatures ranging from 1873 K to 2073 K. A mixture of calcium oxide and carbon (1:3 molar ratio) was compressed into a small cylindrical pellet (20 mm in diameter and 30 mm in height) and reacted in a vacuum electrical furnace at CO pressures ranging from 0.07 to 0.26 atm.

The study showed that the reaction followed parabolic kinetics. It was also found that in addition to reaction (2.8), there existed a decomposition reaction whose rate was zero order, and which increased linearly with time and temperature. The velocity of the forward reaction depended strongly on carbon monoxide pressure. The velocity decreased with increasing CO pressure. This led the researchers to conclude that the kinetics was controlled by the diffusion of CaO into C and vice versa as well as the diffusion of CO through the product layer. One can understand that the diffusion of the solid reactants through each other would represent the major resistance. The diffusion of CO through the product layer would present a much smaller diffusional resistance. A similar study by Brookes et al. (1975) showed that resistance to CO diffusion through the product layer was small due to the high porosity of the layer. It should be noted here that a thermodynamic analysis (conducted for the present project) of reaction (2.8) indicated that the reaction was complete at 2150 K, and it would not proceed below 1600 K at atmospheric pressure.

Brookes et al. (1975) modelled the kinetics of the formation of calcium carbide in solid pellets assuming that the reaction rate was controlled macroscopically by heat transfer. The study was carried out for the temperature range (1923 to 1993 K) using pellets similar to those used by Tagawa and Sugawara (22.2 mm in diameter and 31.8 mm in height); the CO pressure was fixed at 0.07 atm. The study showed that the decomposition of calcium carbide, within the product layer, took place at a rate dependent upon the local temperature. The researchers used the following two-step mechanism proposed by Kameyama (1956):

$$CaO + C = Ca(g) + CO \qquad (2.9)$$

$$Ca(g) + 2C = CaC_2 \qquad (2.10)$$

The reverse of reaction (2.10) is zero order and depends on temperature and time. This may explain the negative effect of increasing the CO pressure on the production of CaC_2. Increasing the CO pressure would force reaction (2.9) to the left resulting in less Ca produced and hence less CaC_2. A study by Mu and Hard (1987) showed that the decomposition of CaC_2 took place even at atmospheric pressure, and it was slowed down by decreasing the partial pressure of CO (in a gas mixture of Ar and CO). The effect of CO partial pressure, however, appeared to be negligible for temperatures above 2173 K.

The study by Mu and Hard (1987) was conducted for the temperature range (1853 to 2223 K) and for CO partial pressures ranging from 0 to 1 atm. The reaction was carried out in an induction furnace and in a rotary kiln. The reactants were pelletized from a mixture of calcium hydroxide, coke and limestone. The product was characterized as being black with low bulk density and very porous; it contained 50-60% CaC_2 and up to 15% free carbon. Mu and

Hard (1987) reported higher conversion with low-grade coal and found that the conversion increased with the amount of volatiles in the coal. This is mainly due to kinetic effects, and it suggests that addition of methane to reaction (2.8) improves the reaction rate in the solid phase reaction.

Although the studies mentioned above may give sufficient explanation of the kinetics of CaC_2 formation in solid pellets, they do not give a complete account of the reaction at the microscopic level. This is especially true for a reaction taking place in a plasma spout-fluid bed. Reactants in a pellet are in direct contact at the start of the reaction. The resistance to the reaction, however, is expected to increase as a product layer is formed around one or both of the reactants. In a plasma spout-fluid bed, the reactants have only short contact times in the reaction zone. It is expected that a product layer will form around one or both of the reactants as they react. This layer may be stripped off by attrition due to the movement in the bed making the reactants free to react upon further contact. It is also expected that the presence of the plasma species would improve the reaction rate as was reported by Okubo et al. (1990). Thus, the kinetics of the solid phase formation of CaC_2 in a Plasma Spout-Fluid bed Reactor (PSFR) may prove to be different from those reported in the literature for conventional reactors. A thorough understanding of this kinetics is needed. It is the aim of the present study to investigate the feasibility of the solid phase formation of calcium carbide in a plasma spout fluid bed and to understand the reaction morphology and the rate controlling mechanisms.

CHAPTER THREE

"Attempt the end and never stand to doubt;
Nothing so hard but search will find it out"

Robert Herrick (1591-1674)

CHAPTER III 3

EXPERIMENTAL METHODS

This chapter presents a description of the main components of the experimental apparatus as well as the experimental procedure. Materials used in the work including the solid reactants and the plasma gas are also described. Experimental techniques used to analyze the reactants and the solid products are described at the end of the chapter.

3.1 EXPERIMENTAL APPARATUS

The experimental set-up consisted of a power supply, a DC plasma torch, a fluid bed, a CO analyzer and a temperature measuring system. A schematic diagram of the apparatus is shown in Figure 3.1.

3.1.1 Power Supply and Plasma Torch

Power was supplied by a DC welding rectifier with an open circuit voltage of 400 V rated at 70 kW. The rectifier was connected to a control console, manufactured by Metco Inc., which controlled plasma gas flow rate and power to the torch. The console was equipped with a safety interlock device which required a pre-set plasma gas pressure of 345 kPa. The console was also equipped with a safety shut-off system which could be deployed in case of an emergency.

The plasma torch was manufactured by the Plasma Technology Research Centre (CRTP) of Sherbrooke University. It had a conical thoriated tungsten cathode and an annular copper

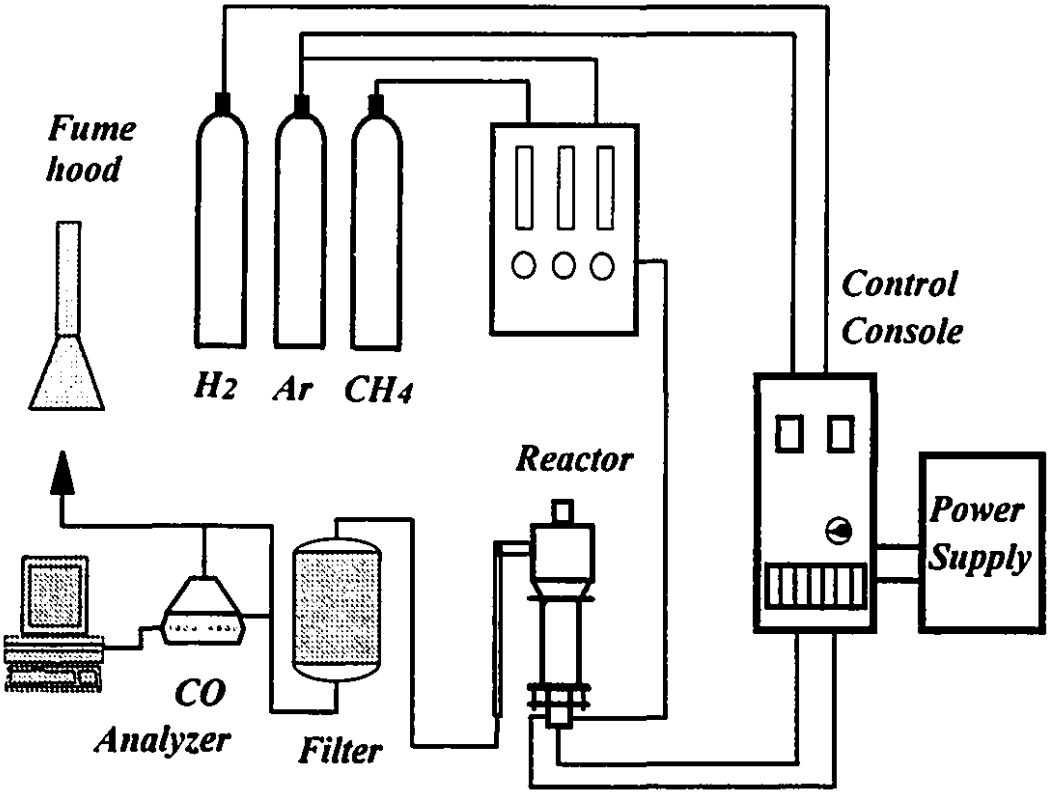

Figure 3.1: A Schematic Diagram of the Experimental Apparatus.

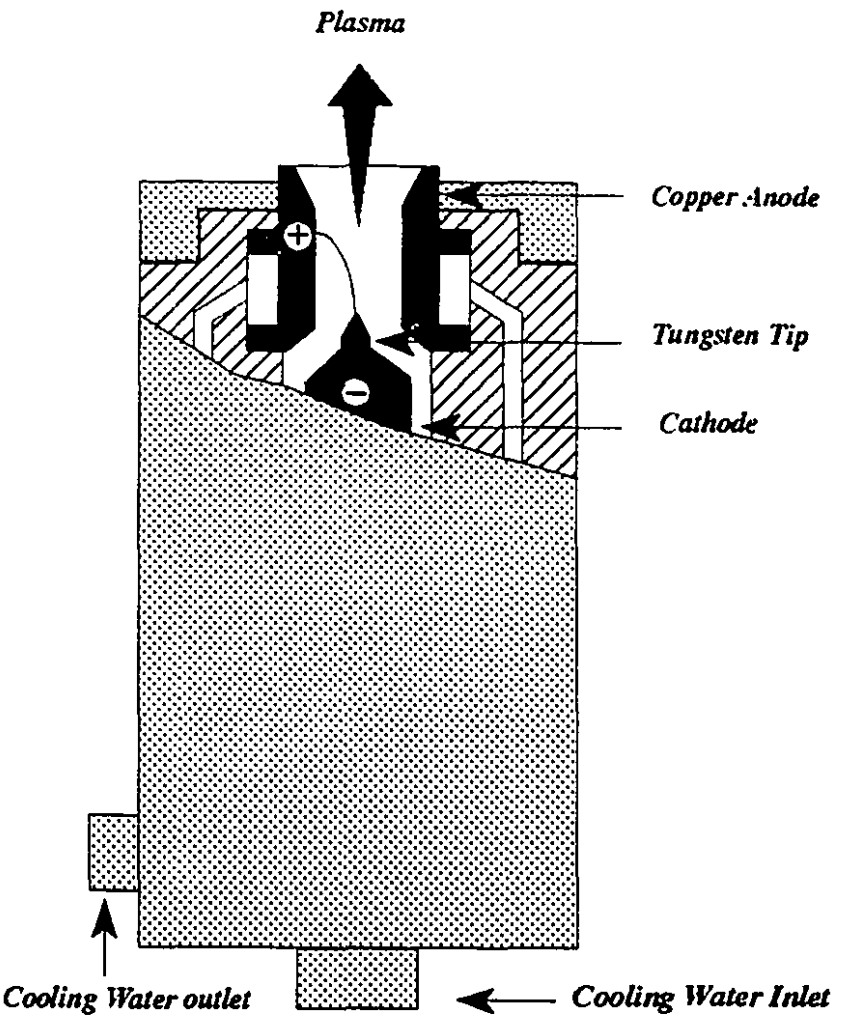

Figure 3.2: Configuration of the Plasma Torch.

anode as shown in Figure 3.2. The design power of the torch was of the order of 20 kW, and the power to the torch was controlled by varying the current. Argon at a flow rate of 40 L/min at 345 kPa (50 psi) was used to initiate the arc, and hydrogen was then added, keeping the total flow rate fixed at 40 L/min., to increase the arc voltage and hence raise the power and plasma enthalpy.

3.1.2 Fluid Bed

The fluid bed system consisted of two parts: the reactor section and the disengaging section. The inner part of the reactor is a graphite cylinder (8 cm in internal diameter and 35 cm in height) surrounded by a 2 cm of graphite felt insulation. The cylinder and the felt are contained within a stainless steel cylinder (13 cm in internal diameter) which is also insulated on the outside to minimize heat loss. The lower part of the reactor housed the distributor and the plasma torch. The distributor is made of type 304 stainless steel, and consists of a water-cooled flange, three tangential gas entries (spouting) and a fluidization gas distributor plate. The tangential gas entries (0.635 mm in internal diameter) provide a means for direct injection of a gaseous reactant into the plasma jet and also allow quenching of the jet and hence, a power-independent control of the plasma temperature. The plasma torch is bolted to the distributor, where the tip of the copper anode is positioned at the centre of the distributor through a 2.54 cm hole. The lower part of the distributor is water cooled through three V-shaped passages (0.635 mm in internal diameter). A drawing of the distributor is shown in Figure 3.3.

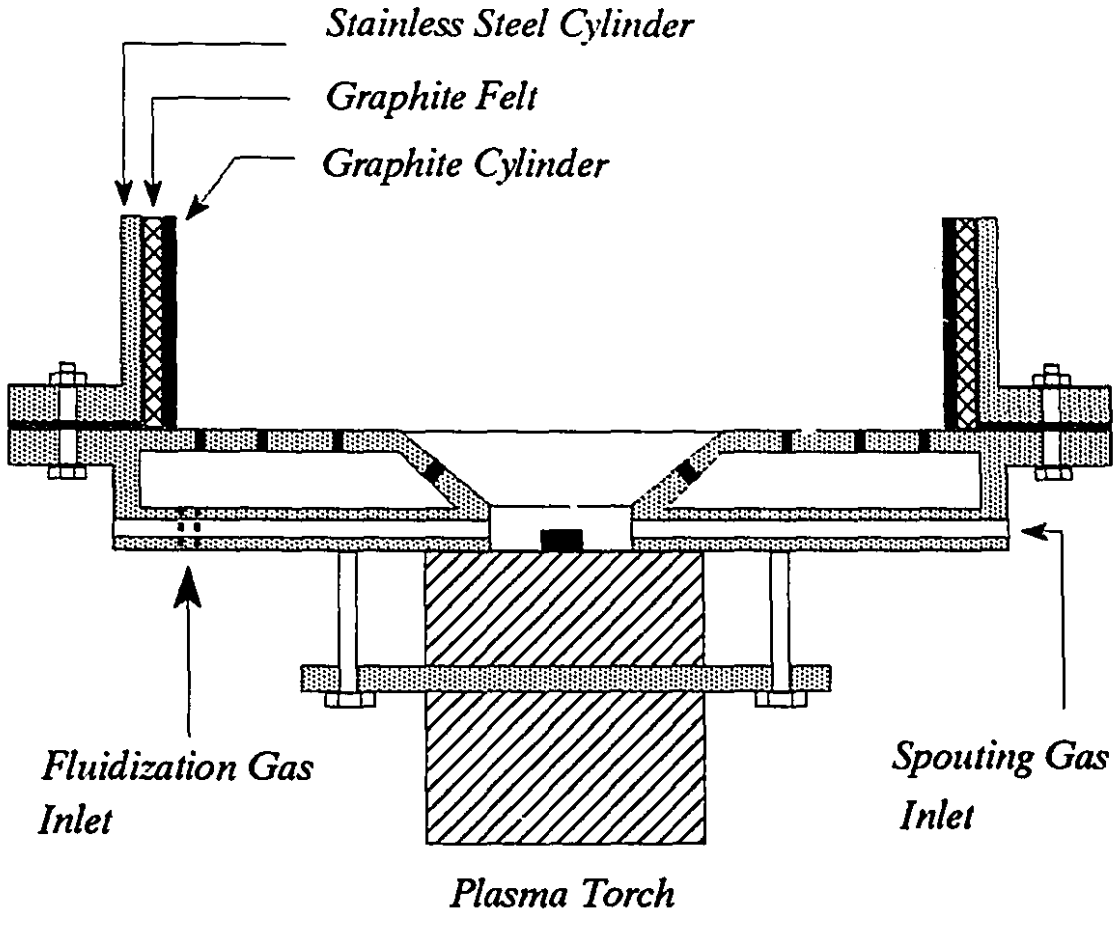

Figure 3.3: A Cross Section of the Gas Distributor.

The disengaging section is a stainless steel cylinder 25 cm in internal diameter and 25 cm in height. The large diameter lowers the gas velocity and minimizes elutriation of particles. This section was connected to the reactor through a stainless steel cylinder with an internal diameter that increases from 13 cm to 25 cm. The three sections were bolted together and sealed with high temperature gaskets. A swivel support was fixed to the middle section to allow easy movement of the bed from a vertical to a horizontal position. This arrangement facilitated the loading of the reactants and the unloading of the product. An iron pipe frame (190 cm in length, 100 cm in width and 245 cm in height) was constructed to provide stable support for the reactor. A detailed drawing of the fluid bed reactor is shown in Figure 3.4

The reactor was operated in a semi-batch mode, in which the solid reactants were charged into the reactor before each run. Gaseous products leave the reactor with the plasma gas, where they pass through a heat exchanger and a baghouse filter before evacuation into a fume hood.

3.1.3 Carbon Monoxide Analyzer

Gaseous products leaving the filter were continuously analyzed for carbon monoxide using a Horiba Mexa-201GE CO analyzer. The measuring range of the analyzer was 0.0 to 10 volume percent, and the repeatability was ± 0.04 volume percent or 2% of the reading whichever was greater. The output of the analyzer was 0 to 1 volt and was recorded on a strip chart recorder (Graphtec Corp. Model SR6211). The analyzer was calibrated after every five experimental runs using a CO calibration cylinder supplied by Analagas Systems, Scarborough, Ontario.

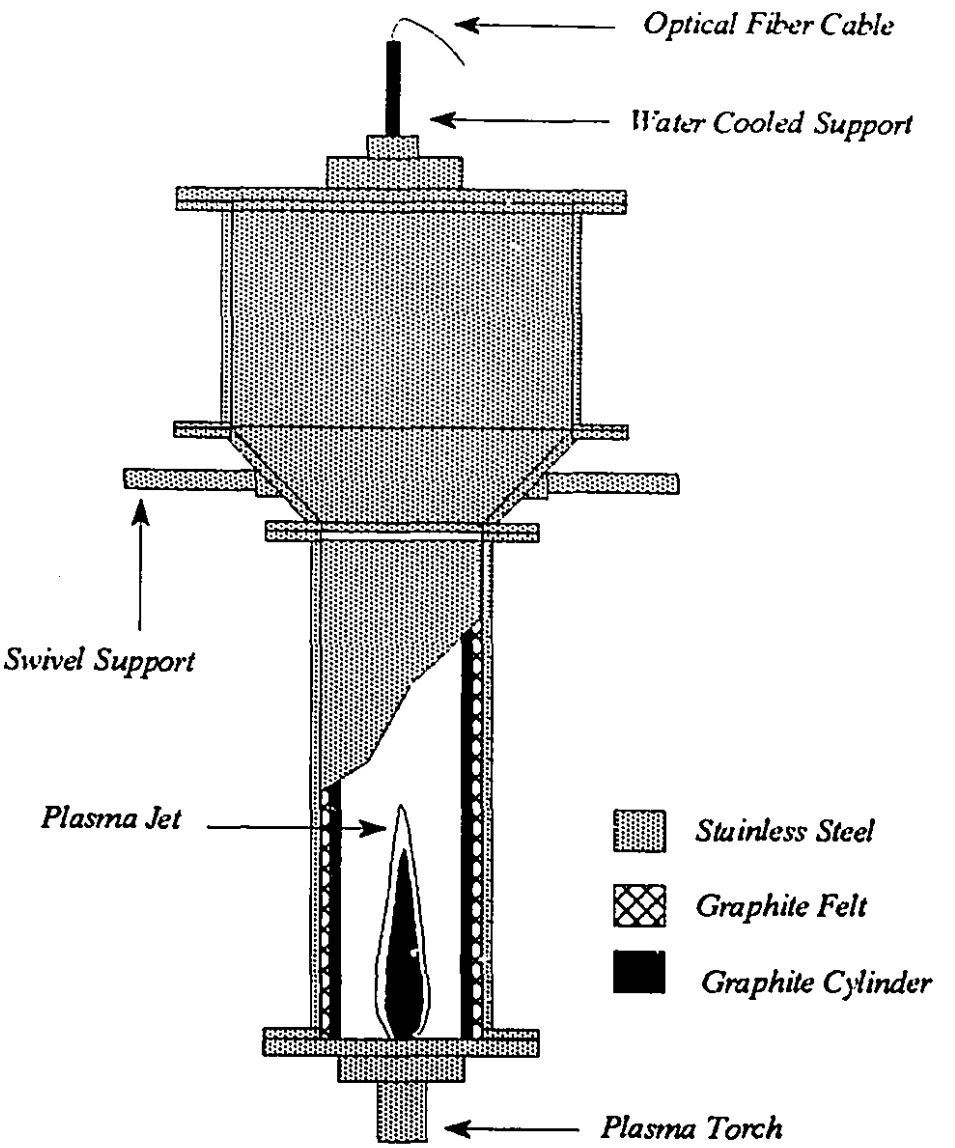

Figure 3.4: A Detailed Representation of the Fluid Bed Reactor.

3.1.4 Temperature Measuring System

The bed temperature was measured using Accufiber High Temperature Measurement and Control System Model 100C. The system is supplied by Luxtron Corporation, Accufiber Division, Beaverton, Oregon, USA. Three different probes can be used with the Accufiber system: Lightpipe Sensor, Blackbody Sensor and Optical Pyrometer. Only the Lightpipe Sensor was used in this work.

The theory of operation of the Accufiber system is based on the emission of radiant energy as a result of temperature. All substances at temperatures above absolute zero emit radiant energy as a result of the atomic and molecular agitation that is associated with the temperature of the substances. The rate of emission per unit area increases with increase in temperature (Harrison, 1960). The lightpipe sensor consists of a single crystal sapphire (aluminium oxide) rod that is optically polished on the end, where the angle of acceptance for the sensor is approximately 52 degrees. The sensor is placed in close proximity to the measurement target . The sensor transmits the radiant energy to a low temperature optical fiber, which in turn transmits it to an optical detector. The detector then converts the radiation to an electrical signal; a microprocessor is then used to convert the signal into the target temperature.

The lightpipe sensor was connected to the optical detector through a flexible optical fiber transmission cable about 3 meters in length. Both sensor and cable were calibrated together by the manufacturer. For each lightpipe sensor, the user has to enter a sensor number, a cable number and a sensor factor. The lightpipe sensor used in this work was recalibrated in a

furnace against a type K thermocouple. The optical fiber transmission cable is limited to a maximum temperature of 338 K, above which the cable could be damaged. For this reason, a water cooled support was made to protect the transmission cable from damage during operation as shown in Figure 3.5

3.2 MATERIALS

3.2.1 Calcium Oxide Source

High calcium quicklime, supplied by BeachviLime Limited of Beachville Ontario, was used as a source of calcium oxide. It is a white porous solid obtained by the calcination of limestone. Analysis of the material as given by the supplier is shown in Table 3.1 The powder had particle sizes ranging from 40 to 1400 μm. Fines less than 53 μm and large particles greater than 1100 μm were removed; the remaining powder had a mean particle size of 170 μm.

Table 3.1: Analysis for the calcium oxide source.

Material	*Average Wt.%*
Calcium Oxide (CaO)	96.00
Magnesium Oxide (MgO)	1.00
Silica (SiO_2)	0.75
Ferric Oxide (Fe_2O_3)	0.10
Alumina (Al_2O_3)	0.10
Total Sulphur (S)	0.03
Carbon Dioxide (CO_2)	1.50

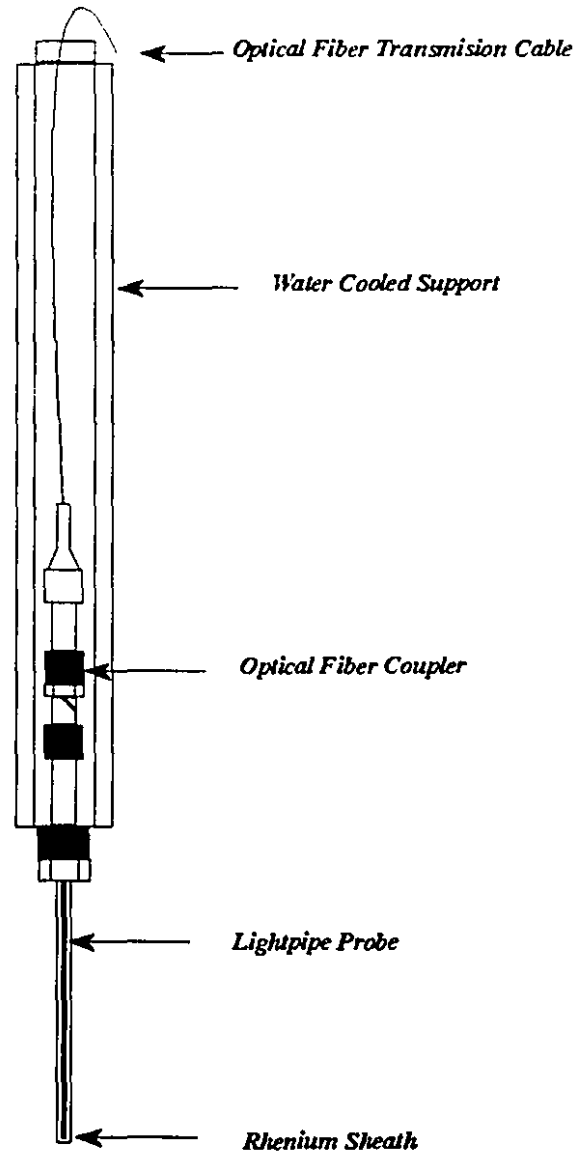

Figure 3.5: A Diagram of the Lightpipe Probe.

The particle size was determined by screening to obtain the weight fraction of each sized fraction. The average diameter was calculated using the surface volume diameter d_{sv}, which gives more weight to fine particles (Pell, 1990). The surface volume diameter is the diameter of a sphere with the same surface area per unit volume as the particle and is given as:

$$d_p = d_{sv} = \frac{1}{\sum_i x_i / d_{pi}}, \quad \text{where} \qquad (3.1)$$

d_p = average particle diameter; x_i = weight fraction of average screen size d_{pi}

3.2.2 Carbon Source

Three sources of carbon were used in this work: graphite powder, coke powder and methane. Graphite was the main source of carbon used in most experiments. It was supplied by FILTREX of Ville d'Anjou, Quebec, and had a mean particle size of 130 μm. A second type of graphite with a larger mean particle size (350 μm) was used in two experiments. This type was previously used by Chin (1989) in the carbothermic reduction of pyrochlore and Nb_2O_5 and is referred to in this work as graphite II (G-II). Metallurgical coke with a mean particle size of 200 μm was supplied by Dofasco of Hamilton, Ontario. Analysis (CHN) of graphite I, graphite II and the coke is given in Table 3.2. Particle size distributions for calcium oxide and graphite I are shown in Figure 3.6 and Figure 3.7 respectively.

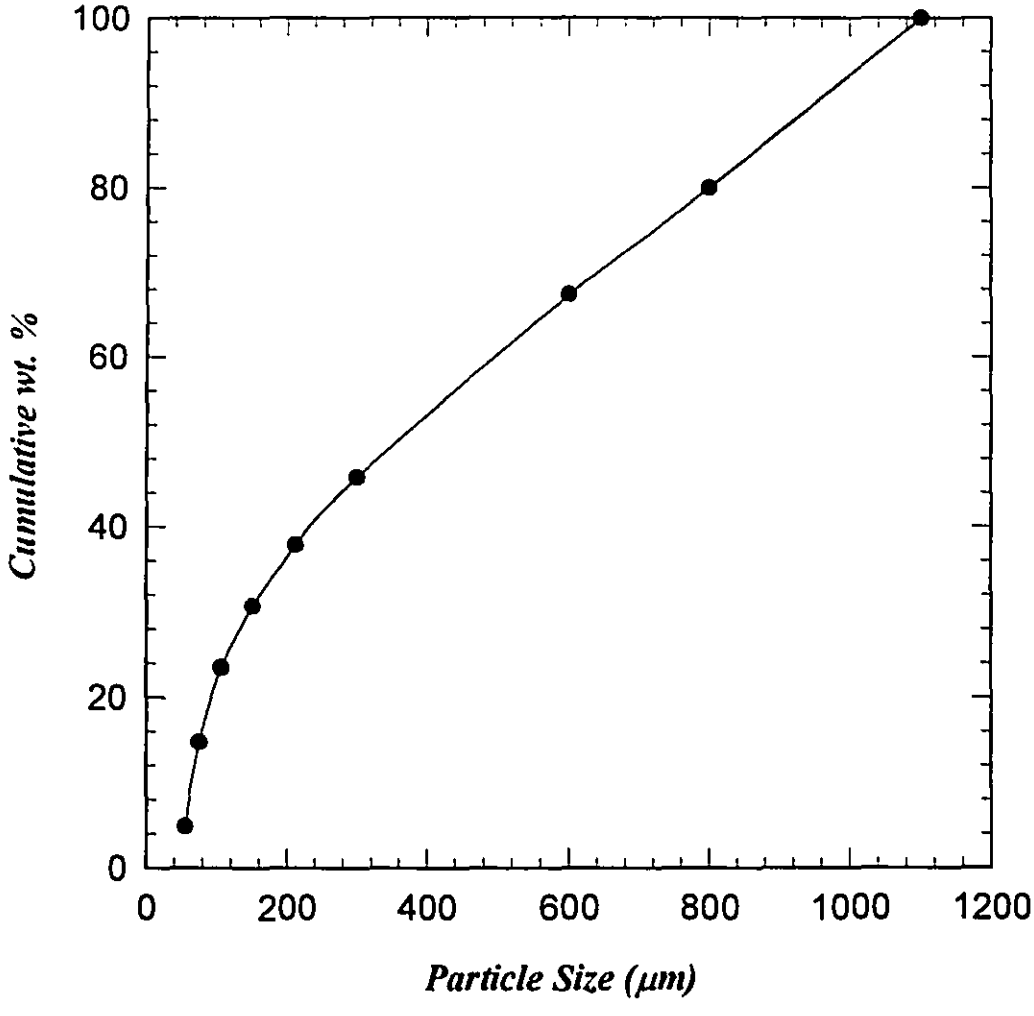

Figure 3.6: Particle size distribution for calcium oxide powder.

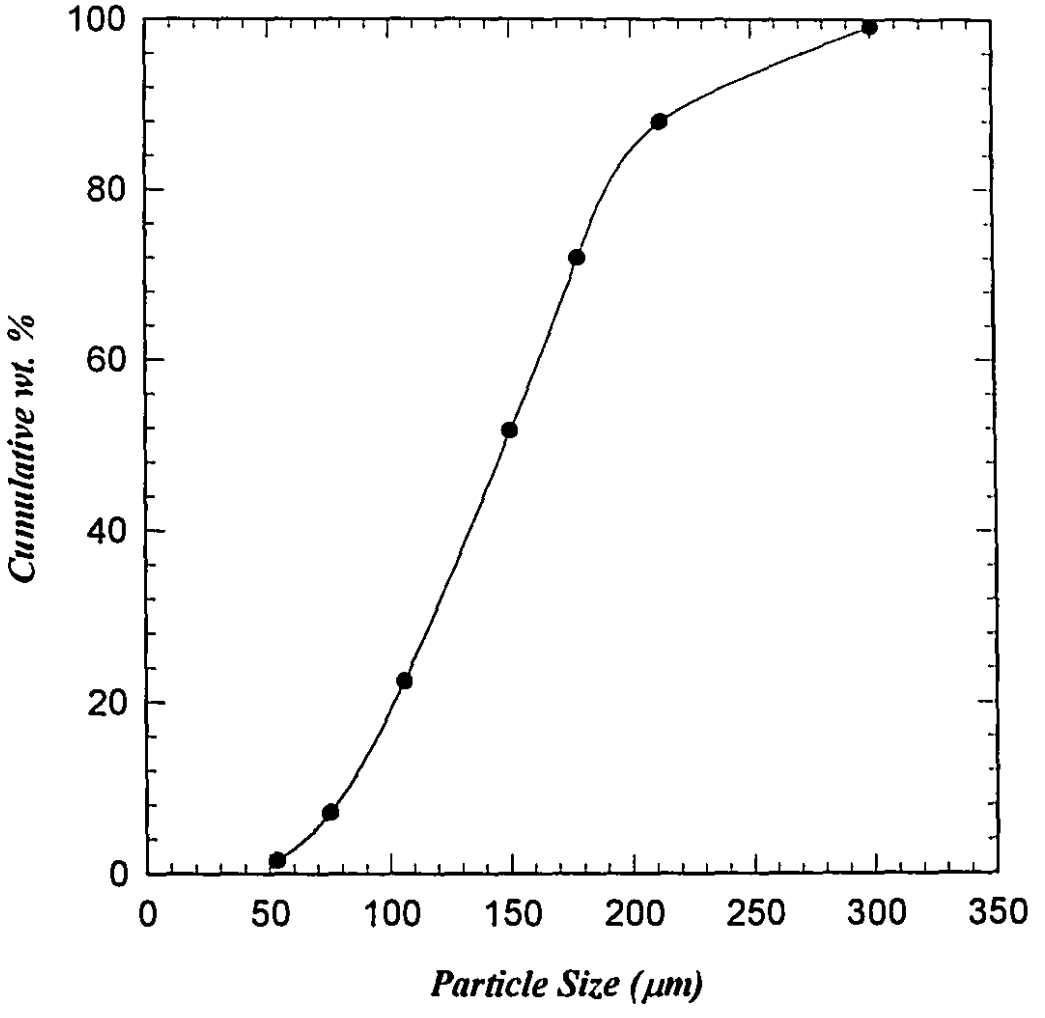

Figure 3.7: Particle size distribution for graphite (G-I) powder.

Table 3.2: CHN analysis for Graphite I, Graphite II and Coke.

Material	*Graphite I*	*Graphite II*	*Coke*
Carbon	85.60	97.79	90.08
Hydrogen	0.50	0.20	0.50
Nitrogen	1.07	0.15	1.15
Residue	12.84	1.87	8.27

3.2.3 Plasma Gases

High purity argon (99.995%) at 345 kPa (50 psig) was used as the principal plasma gas throughout the work. It was also used as the fluidizing gas in all experiments except in the methane runs, where methane gas was used as a source of carbon and as a fluidizing gas. The other plasma gas was high purity hydrogen (99.99%), which was added to argon to increase the voltage and raise the plasma power. While keeping the total plasma gas flow rate fixed at 40 L/min., hydrogen was added at three concentrations (vol.% in argon): 33%, 45% and 67%.

3.3 EXPERIMENTAL PROCEDURE

The experimental procedure can be divided into two parts: preparation and experiments.

I- Preparation

The following preparatory steps were carried out before each experimental run:

- The fluid bed was thoroughly cleaned and placed into the horizontal position. The distributor and the plasma torch were also cleaned and fastened to the reactor.

- The Accufiber temperature probe was fixed in position inside the reactor and connected to the optical detector. Power cables, gas lines and water lines are connected to the system. The cooling water was turned on and the system was checked for water leaks. The grounding of the system was also checked.
- Calcium oxide was screened to the desired particle size and about 610 g were loaded into the reactor. If needed, the stoichiometric amount of graphite was added.
- The reactor was then tightly sealed and purged with argon for about three minutes (about 10 gas changes of reactor volume). At the same time, the CO analyzer was connected to the sampling port.

II- Experiments

The experimental runs were carried out as follows:

- The main power to the rectifier and power to the control console were turned on. Before starting the plasma torch, power to the measuring instruments (i.e. Temperature measurement system) was turned off to prevent damage by the high frequency field.
- The plasma gas flow rate was set at 40 L/min. (Argon at 50 psi), and the plasma torch was ignited. The reactor was swivelled to the vertical position. Hydrogen was immediately added at the desired flow rate and the current was adjusted to the predetermined setting. A stop watch was started to record the run time.

- During the run, both voltage and current were monitored to ensure constant power. Carbon monoxide concentration, bed temperature, reactor wall temperature and exhaust gas temperature were continuously monitored and recorded.
- After running the experiment for 30 to 40 minutes (depending on the conditions and the bed stability), the plasma torch was turned off and the reactor was immediately swivelled back into the horizontal position. Hydrogen was turned off, while the argon flow was continued for a few minutes to cool the bed and purge the system. Power to the system was turned off and the reactor was allowed to cool for about 3 to 4 hours.
- Once the reactor reached room temperature, power cables and cooling lines were disconnected. The plasma torch and the distributor were removed from reactor. A representative sample of the bed materials (about 25 g) was immediately taken, sealed in a sampling vial, labelled and stored in a dessicator.
- The bed materials were emptied into a dry container, weighed and stored. The fine powder in the filter was collected, weighed and a sample was taken for analysis. The fluid bed, the heat exchanger and the filter were cleaned and prepared for the next run.

3.4 ANALYTICAL TECHNIQUES

The reactants and the solid products were analyzed using the following techniques: porosity analysis, CHN analysis, FTIR, X-ray diffraction, microscopic analysis and acetylene formation test. The first two techniques were used to analyze the reactants, while the remaining techniques were used for identifying and analyzing the solid product.

3.4.1 Porosity Analysis

The porosities of the calcium oxide particles and of graphite were determined using Micromeritics mercury porosimeter (PoreSizer 9320). The instrument measures the volume distribution of pores in materials by mercury intrusion at a high pressure up to (30,000 psi) 207 MPa, covering the pore diameter range from approximately 360 to 0.0066 μm. The unit has two built-in low pressure ports and one high pressure chamber.

A powder sample (about 0.2 to 1.0 g) was accurately weighed and placed in a special sample holder called "penetrometer". The weight of the sample depended on the material and its porosity, and hence a trial run was needed for each material to determine the weight range. The penetrometer and the sample were placed in a low pressure port and the pressure was lowered to about (50 μmHg) 6.7 MPa. The aim of this procedure was to degas the sample and remove any moisture. The pressure in the chamber was then raised to atmospheric and mercury was introduced to the sample while increasing the pressure to about 30 psi. The penetrometer, which was filled with mercury, was placed in the high pressure chamber where pressure was increased to up to 30,000 psi, pushing the mercury into the internal pores of the particles. For both low pressure and high pressure runs, data were continuously collected as a function of pressure. These included: cumulative intrusion, incremental intrusion, differential intrusion, pore diameter, incremental pore area and cumulative pore area.

3.4.1.1 *Theory of Operation*

Mercury intrusion porosimetry is a convenient method of determining pore size distribution and porosity of materials. Mercury has a high surface tension and is non-wetting to most materials. This causes a mercury surface in contact with a solid to assume the minimum surface area and the largest radius of curvature possible at a given pressure. Raising the pressure shifts the balance between the surface tension and the surface area causing the radius of curvature to become smaller. When the radius of curvature equals that of the pore entrance, then the mercury fills the volume within the pore. The pore diameter (D) is related to the applied pressure (P) through the Washburn equation (Washburn, 1921):

$$D = -(4/P)\gamma\cos\varphi \qquad (3.2)$$

where γ is the surface tension of mercury and φ the solid-mercury contact angle. The above equation is based on the capillary law and assumes cylindrical pores. The generally accepted value for γ is 485 dynes/cm and that of the contact angle (φ) is 130. The volume of mercury V intruded into the pores is measured directly as a function of applied pressure. Mercury porosimetry measures the volume of pores in a solid but not voids. A void is defined as an empty space which occurs where there is a discontinuity in the array of atoms and molecules. A pore is a special class of void which is connected to the surface of the solid; it comes from the Greek word πορος, which means a passage (McEnaney and Mays, 1989).

3.4.1.2 *Pore Surface Area*

The pore surface area can be calculated on the basis of cylindrical geometry or on the basis of the work required to immerse a solid surface in mercury. The work (dW) required to immerse an area (dA) of a solid in mercury is given by (Rootare and Prenzlow, 1967):

$$dW = \gamma \cos\varphi \, dA \qquad (3.3)$$

For mercury porosimetry, work is supplied when pressure(P) forces a volume of mercury (dV) into the solid pores. Thus,

$$PdV = -\gamma \cos\varphi \, dA \quad \text{or} \quad dA = -\int PdV/\gamma\cos\varphi \qquad (3.4)$$

From pressure-volume data, $\Sigma\Delta A = \Sigma P\Delta V/\gamma\cos\varphi$. (3.5)

This equation gives the cumulative pore area as a function of pore volume and the applied pressure.

3.4.2 CHN Analysis

The carbon, hydrogen and nitrogen content of the two types of graphite and coke was determined using the Control Equipment Elemental analyzer model 240-XA. The unit consists of a combustion tube, a reduction tube, and a series of thermal conductivity detectors. The analyzer is accurate within 0.3 % (absolute), and it can be used to determine elemental analysis for carbon, hydrogen, nitrogen, oxygen and sulphur. Different arrangements of tubes are used for oxygen and sulphur analysis (EL-Naas, 1991).

For carbon-hydrogen-nitrogen analysis, a sample of 1-3 mg is accurately weighed (±0.0005 mg), loaded into the analyzer and combusted in pure oxygen. The products of combustion (water vapour, carbon dioxide, nitrogen oxides and other gases) are carried by helium through the reduction tube and then through the analytical train. Water vapour is removed by a water trap located between the first pair of thermal conductivity cells. The change in signal by the detectors reflects the water or hydrogen content of the sample. Another trap between the following pair of detectors removes carbon dioxide and determines the carbon content. Nitrogen oxides are converted into molecular nitrogen in the reduction tube, and the nitrogen content of the sample is determined by the last two detectors.

3.4.3 Product Analysis

Three analytical techniques were employed to identify the solid product. Samples of the product were analyzed by Fourier Transform Infra Red (FTIR) and X-ray diffraction. The results were compared with analyses of samples of calcium carbide ordered from Anachemica. Also, an acetylene test was used to determine the calcium carbide content of the solid product.

An accurately weighed sample of the solid product (about 2 g) was placed in a 250 ml flask which was connected, through plastic tubing, to a second 250 ml flask filled with water. The second flask was also connected to an empty beaker. A known volume of water was added to the sample (excess water was used to absorb the heat of reaction and

keep the temperature near ambient). Calcium carbide reacts with water to produce calcium hydroxide and acetylene according to the following reaction:

$$CaC_2 + 2H_2O \rightarrow Ca(OH)_2 + C_2H_2 \qquad (3.6)$$

The evolved acetylene displaced water from the second flask into the beaker. The volume of the displaced water was equal to the volume of acetylene, water added and water vapour. The moles of acetylene and hence the conversion was determined.

3.4.4 Microscopic analysis

Microscopic analysis of the reactants and the solid product was also carried out using the Microprobe Laboratory of the Department of Geological Sciences. A sample of the solids was mixed with a resin (a polymer) and placed in a shallow plastic cylinder (about 2.5 cm in diameter and 0.5 cm in height) and allowed to harden for 24 hours. The solid mixture was then polished and cross sections of the reactants (before reaction) and partially reacted graphite and calcium oxide particles were examined. The mixture was polished with alumina using an organic solvent (Freon) as a lubricant. Spot analysis and mapping for carbon, oxygen and calcium were carried out for some particles.

CHAPTER FOUR

"God does not care about our mathematical difficulties.
He integrates empirically"

Albert Einstein (1879-1955)

CHAPTER IV 4

THERMODYNAMIC ANALYSIS

A thermodynamic analysis of the reaction of calcium oxide and carbon was carried out using FACT (Facility for Analysis of Chemical Thermodynamics, Bale et al., 1979). The aim of this analysis was to determine the equilibrium chemical composition of the reaction at different plasma temperatures and to estimate the theoretical energy requirement for the plasma spout fluid bed process.

4.1 EQUILIBRIUM COMPOSITION

Equilibrium calculation is based on the minimization of the Gibbs free energy (G). For any chemical system to be at equilibrium, G must be at a global minimum at the given thermodynamic conditions of fixed pressure and temperature. One of the most widely used approaches is the nonstoichiometric formulation first described by White et al., (1958). In this method, the Gibbs free energy is minimized for fixed temperature and pressure in terms of n mole numbers and subject to m elemental-abundance constraints (Smith and Missen, 1982).

The FACT subprogram EQUILIB was used for the equilibrium calculations. It was assumed that only pure substances (carbon and calcium oxide) were present to react in a closed system. Other substances assumed to be present at equilibrium included: CaC_2, CO and Ca; no solutions were considered for the calculations. The temperature was varied from 1500 to 2200 K. The equilibrium analysis was carried out for the following three reactions:

$$CaO + 3C = CaC_2 + CO \quad (4.1)$$

$$CaO + 2C + CH_4 = CaC_2 + 2H_2 + CO \quad (4.2)$$

$$CaO + 3CH_4 = CaC_2 + 6H_2 + CO \quad (4.3)$$

When calcium vapour is not considered to be present, the equilibrium composition is the same for the three reactions; the reactions do not take place below 2150 K. Above this temperature, however, the reaction is complete, giving calcium carbide and carbon monoxide as shown in Figure 4.1 (for reaction 4.1). The only difference for the other two reactions is the presence of 2 and 6 moles of hydrogen for reactions 4.2 and 4.3 respectively.

The presence of calcium vapour at equilibrium has no effect on the equilibrium composition for reaction (4.1). The other two reactions, however, proceed at temperatures lower than 2150 K in the presence of calcium vapour, but no carbide is formed below 1600 K. The conversion to CaC_2 reaches its maximum at 2100 K and 2000 K for reactions 4.2 and 4.3 respectively as shown in Figures 4.2 and 4.3. The decline of CaC_2 after reaching a maximum and the rise of carbon after reaching a minimum could be an indication of the decomposition of CaC_2 at high temperatures. It could also be due to the presence of acetylene at the range where it would be stable (2000-2500 K). The presence of Ca vapour lowers the carbon monoxide partial pressure, making the reaction proceed at lower temperatures. Similarly, the presence of hydrogen dilutes the concentration of CO and hence lowers its partial pressure.

One would expect that the addition of an inert gas to reaction (4.1) would have a similar effect. To verify this, two moles of argon were added to reaction (4.1). The equilibrium composition

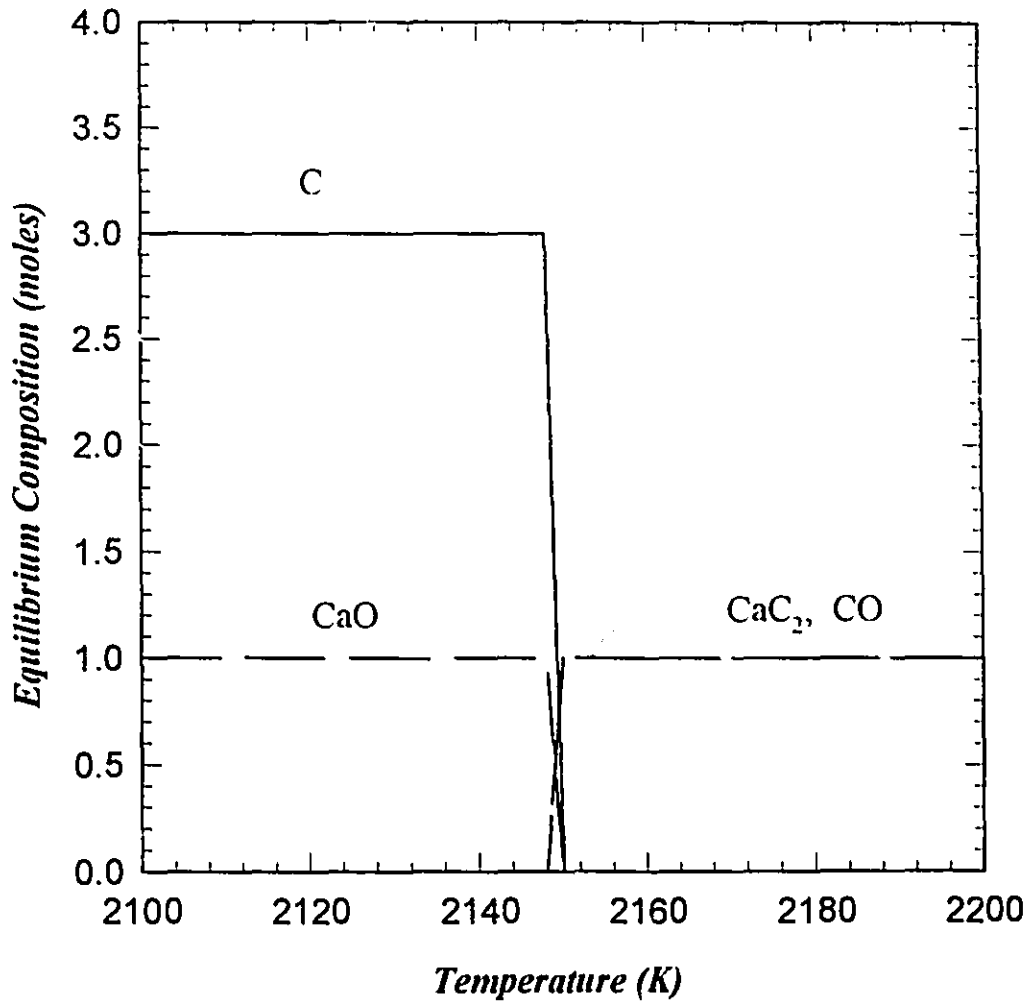

Figure 4.1: Equilibrium composition as a function of temperature for Reaction (4.1).

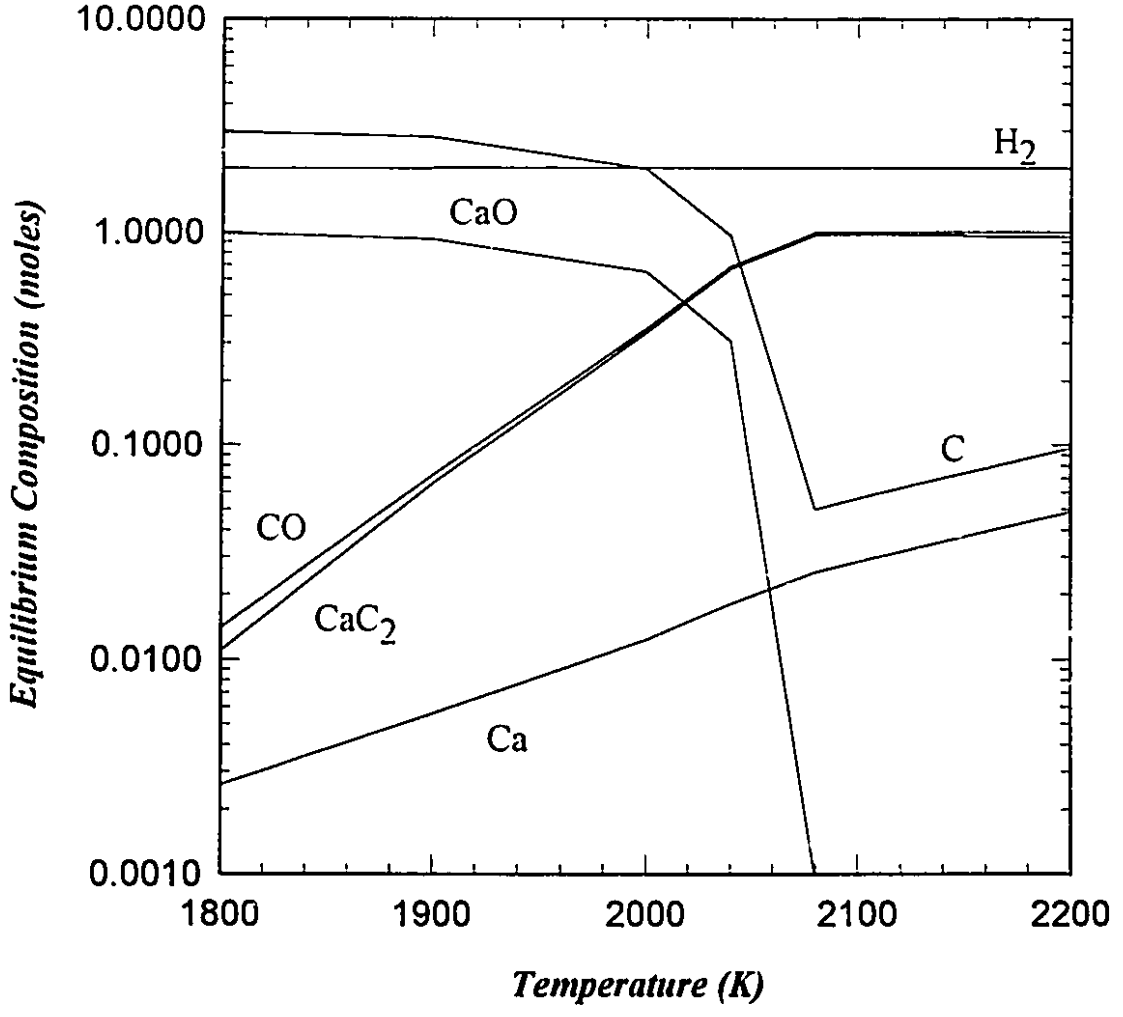

Figure 4.2: Equilibrium composition as a function of temperature for Reaction (4.2) with calcium vapour.

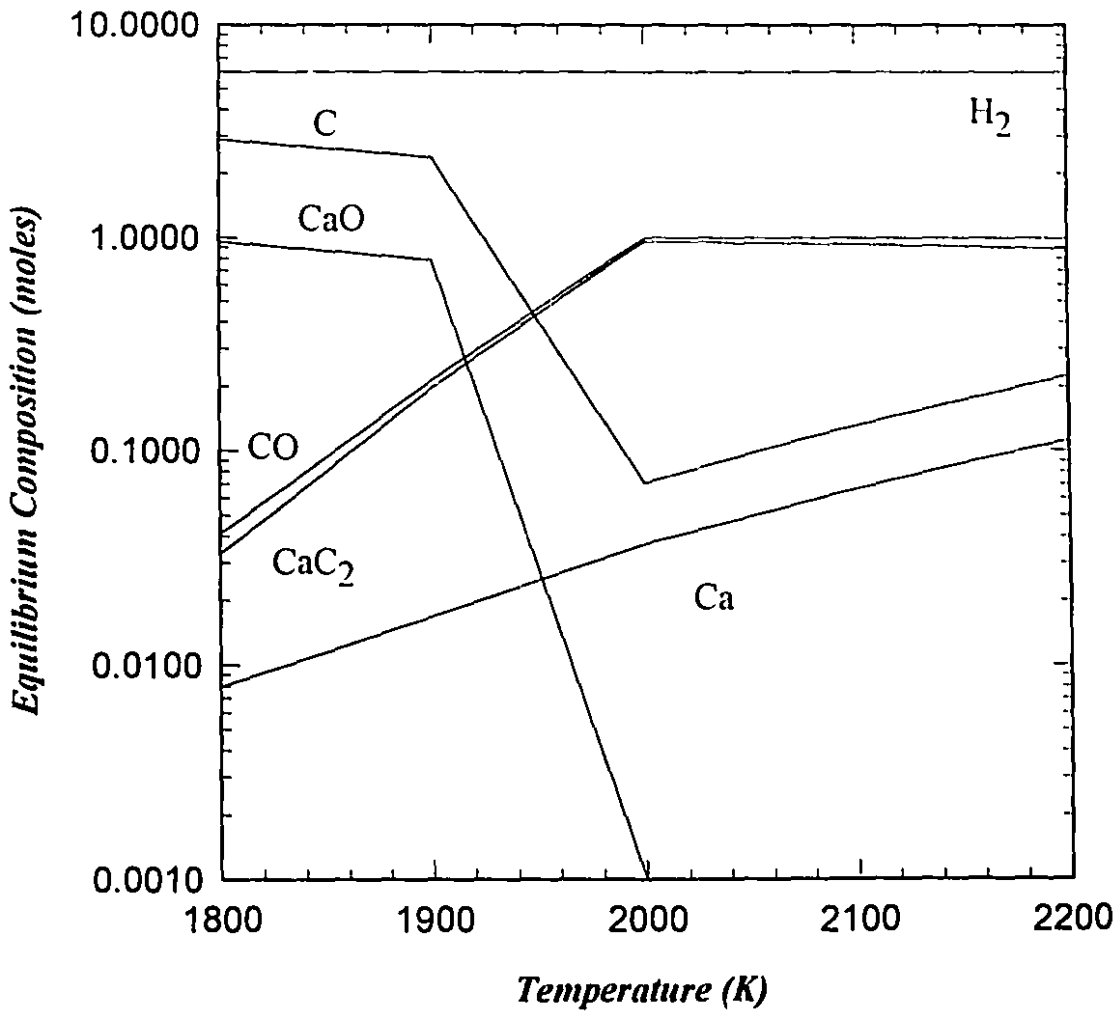

Figure 4.3: Equilibrium composition as a function of temperature for Reaction (4.3) with calcium vapour.

is shown in Figure 4.4. Comparing this to Figure 4.2, one can see that the profiles are similar; however, there is no decline in the moles of CaC_2 and no carbon or calcium vapour is present above 2150 K in Figure 4.4. Since there is no hydrogen present, no acetylene is present; thus, all the carbon and the calcium are converted to calcium carbide. It is worthwhile noting at this point that the addition of a larger amount of argon (20 moles) to Reaction (4.1) lowers the partial pressure of carbon monoxide and makes the equilibrium conversion of calcium carbide even higher at the same temperature as shown in Figure 4.5. However, the reaction still does not take place below 1600 K. FACT analysis for Reaction 4.1 is included in Appendix A.

4.2 PHASE STABILITY

Phase stability diagrams at different temperatures were drawn for the system of calcium carbide, calcium oxide and carbon as a function of the partial pressures of calcium vapour and carbon monoxide, using the Outokumpu HSC Chemistry Program (Roine, 1994). A phase stability diagram at 2000 K is shown in Figure 4.6. Calcium carbide is stable above a minimum calcium vapour pressure and below a maximum carbon monoxide pressure, which depend on temperature. Those pressure limits were determined for different temperatures from 1000 to 2200 K and plotted in Figure 4.7. The two curves in the figure are the minimum calcium vapour pressure (I) and the maximum carbon monoxide pressure (II). According to the phase stability diagrams, calcium carbide is stable when the calcium vapour pressure is higher than curve (I) and the carbon monoxide pressure is lower than curve (II). This clearly indicates that the stability range of calcium carbide is above 1600 K, where the two curves cross. This agrees well with the equilibrium calculations, where no calcium carbide is formed below 1600 K.

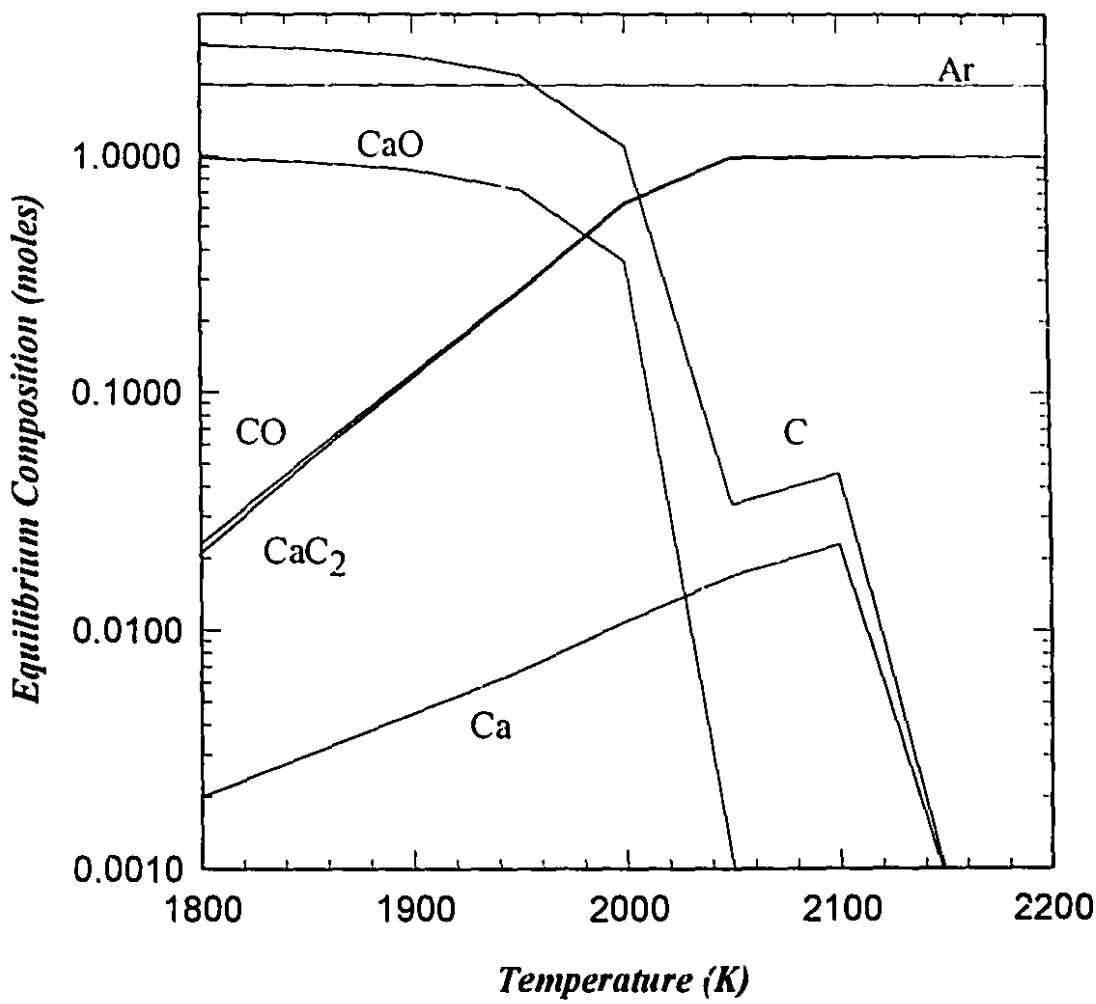

Figure 4.4: Equilibrium composition as a function of temperature for Reaction (4.1) with the addition of two moles of argon; with calcium vapour.

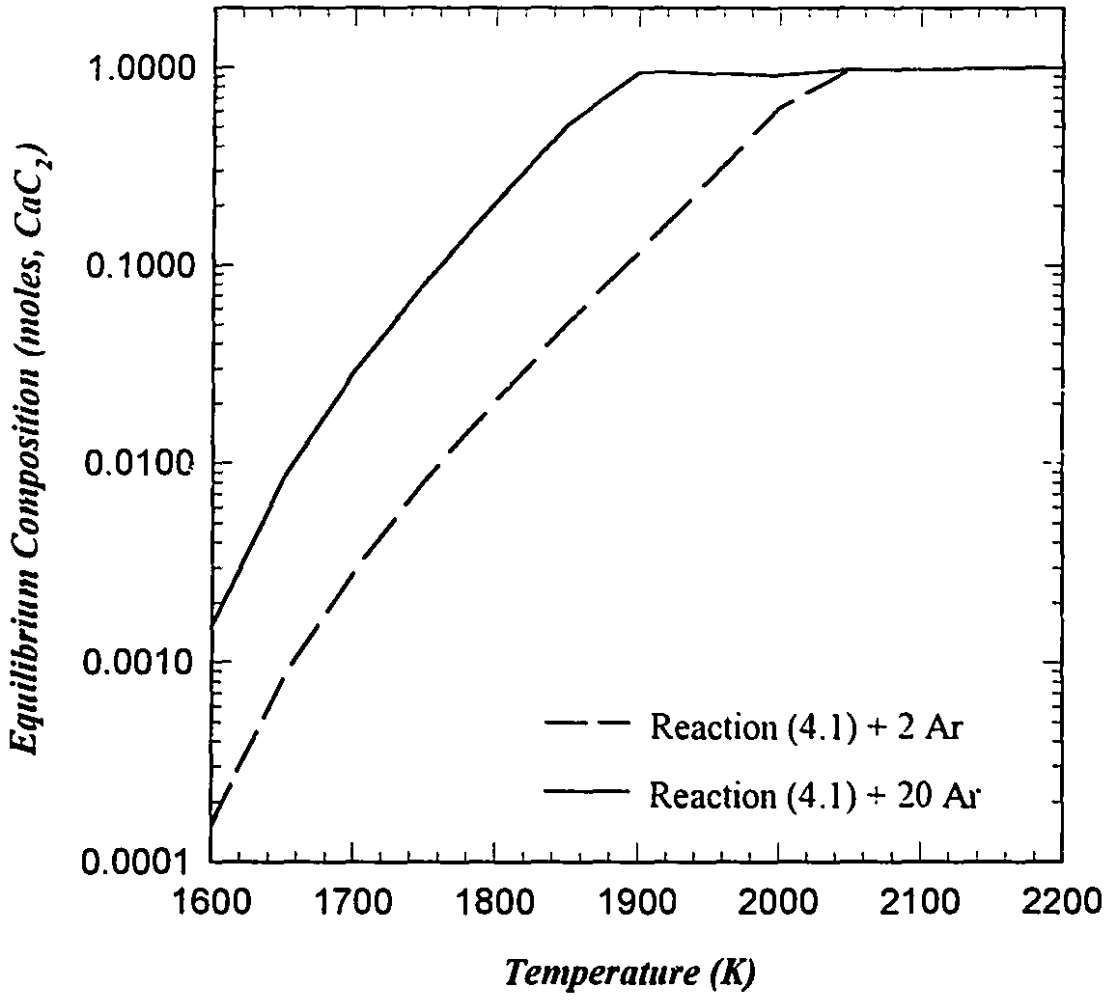

Figure 4.5: A comparison between the equilibrium composition for Reaction (4.1) with two moles and with twenty moles of argon; with calcium vapour.

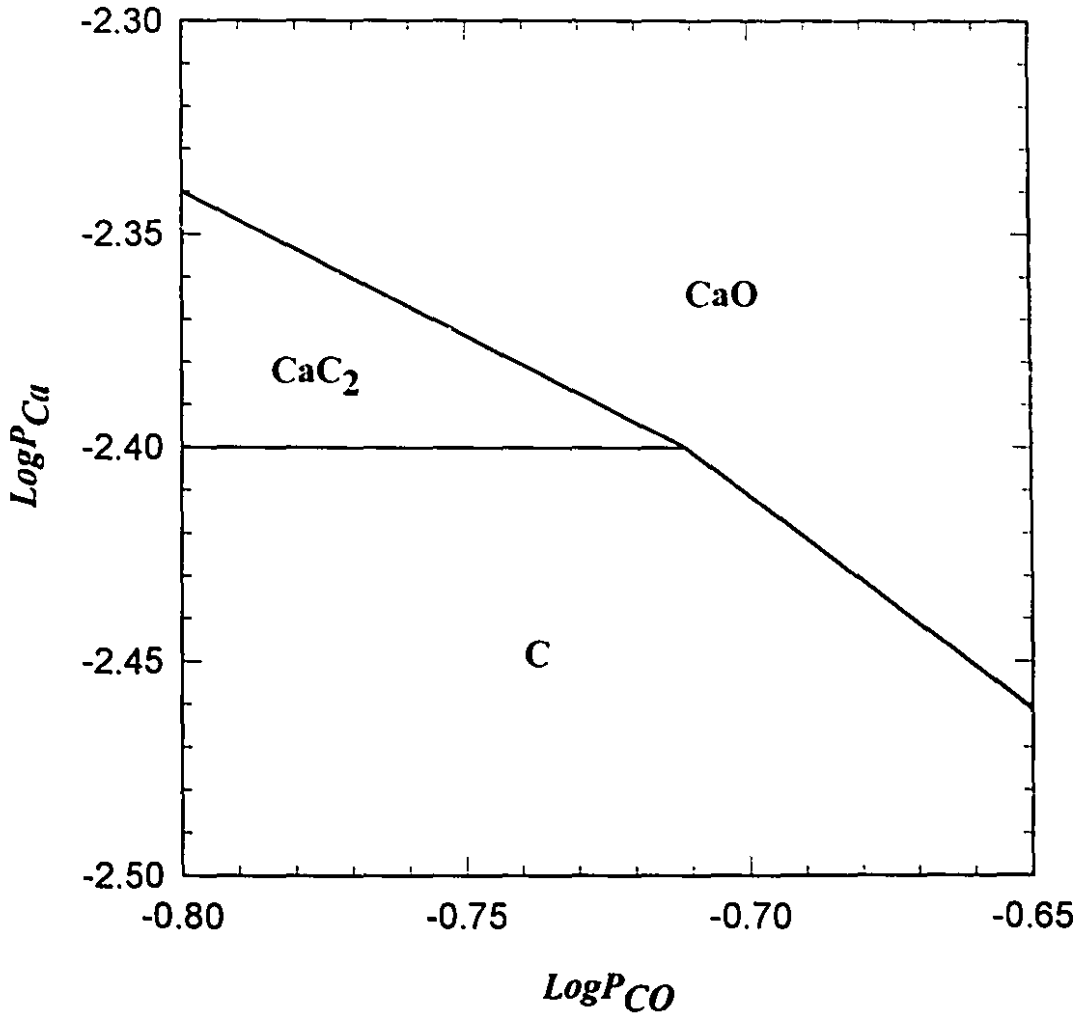

Figure 4.6: A phase stability diagram for calcium carbide, calcium oxide and carbon at 2000 K.

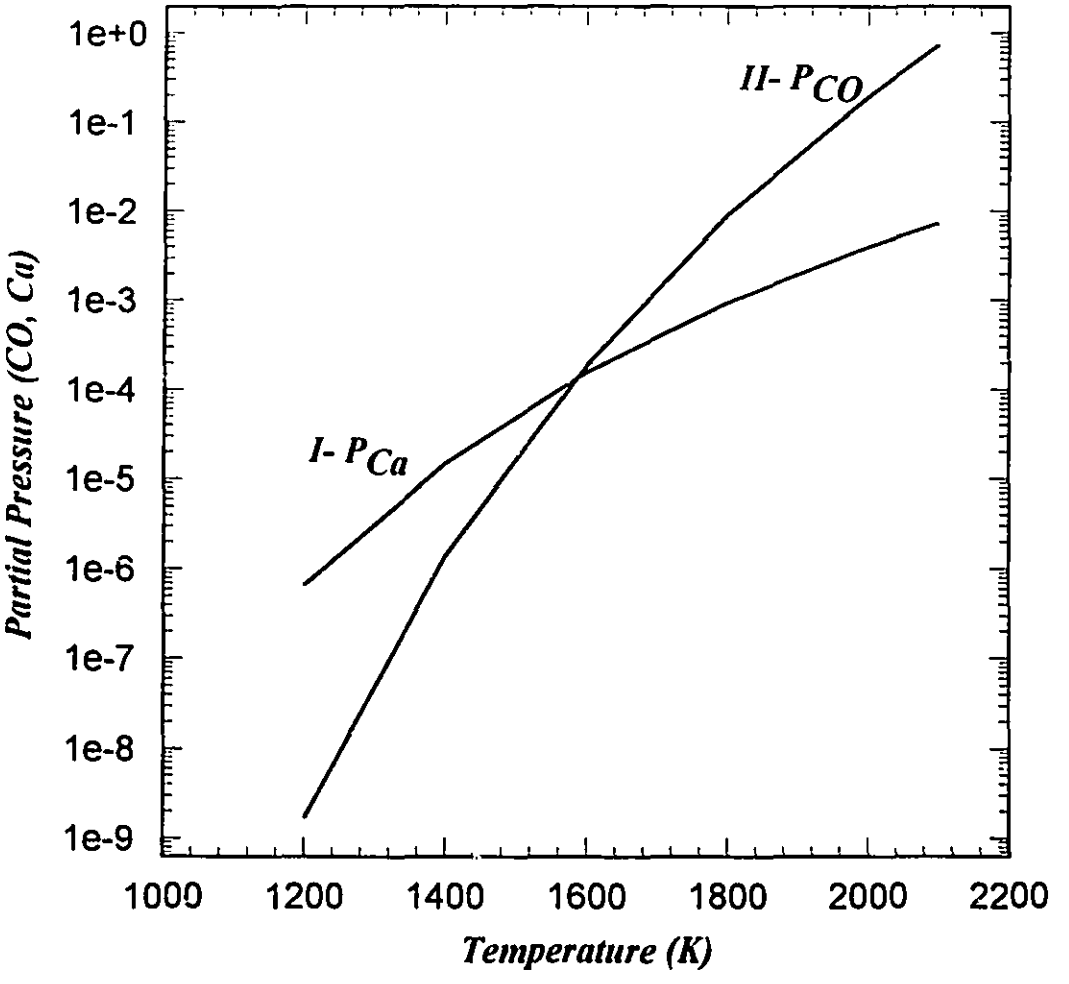

Figure 4.7: Partial pressure limits for calcium vapour and carbon monoxide for the stability of calcium carbide.

4.3 ENERGY BALANCE

A heat balance for the plasma process was conducted using the FACT subprogram REACTION. The balance was done for the three reactions. The theoretical required enthalpy for the process is the sum of the enthalpy required to heat the reactants from room temperature (300 K) to the reaction temperature (chosen as 2150 K) and the enthalpy of the reaction (at 2150 K) minus the enthalpy that could be gained by cooling the products to a temperature T_{pr}. This net required enthalpy for the three reactions is plotted against product temperature in Figure 4.8.

It is shown that if the products are withdrawn at 2150 K, the theoretical enthalpy for the process for Reaction (4.1) is 2.9 kWh/kg CaC_2. If the products are cooled to 300 K, the enthalpy requirements will be lower at 2.0 kWh/kg CaC_2. Assuming torch efficiency of 80%, the net energy requirements will be 3.6 and 2.5 kWh/kg CaC_2 for 2150 K and 300 K respectively. The energy requirement for a typical electric arc furnace is of the order of 4.3 kWh/kg CaC_2. This indicates that the plasma process could achieve up to 40% saving even without including the enthalpy of combustion of the product gases. Reaction (4.1) requires the least energy of the three reactions. A considerable amount of energy is needed to heat the methane gas to the reaction temperature. Thermodynamically, the addition of methane has no effect on the equilibrium composition. The overall effect of adding one of mole methane is just like adding two moles of hydrogen to reaction (4.1), because methane dissociates completely to carbon and hydrogen below 1000 K. From the kinetics point view, however, this may not be the case. As was mentioned before in Chapter 2, the presence of volatiles in the carbon increased the conversion.

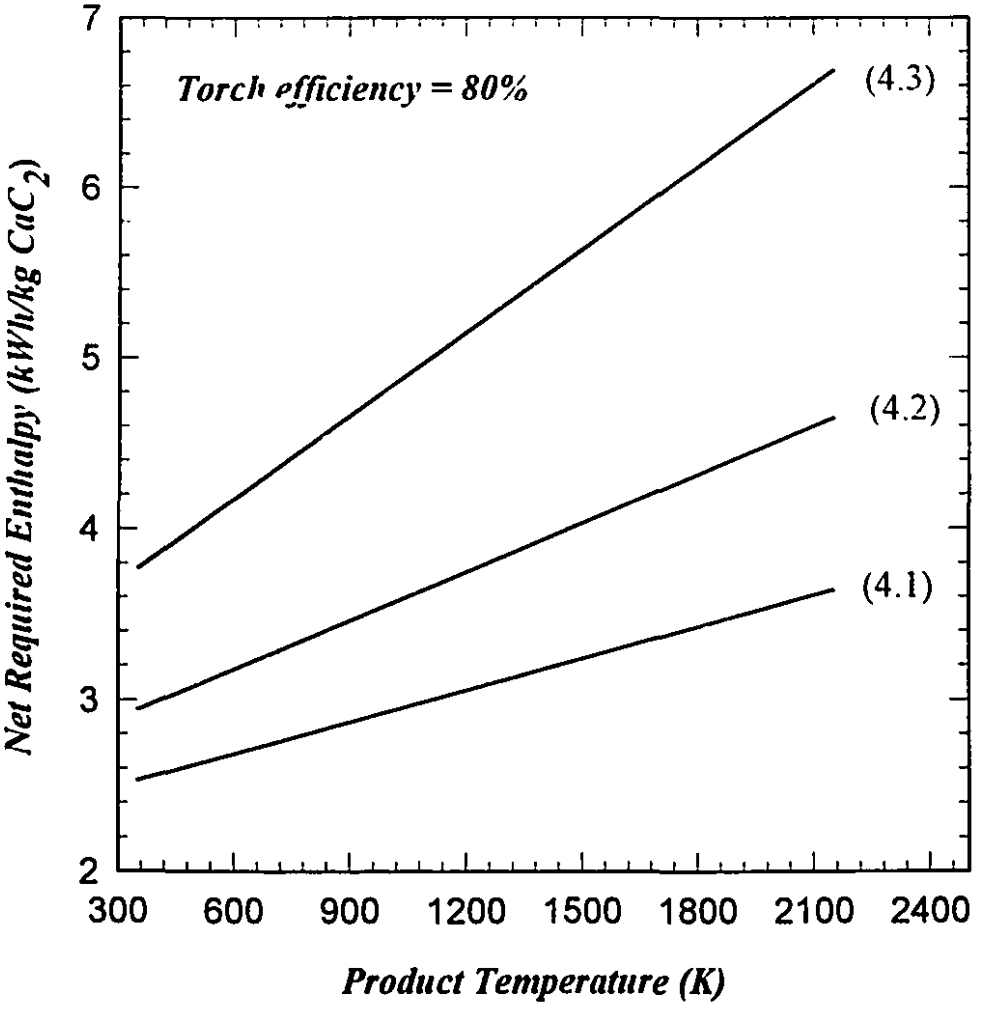

Figure 4.8: Net energy requirements for reactions 4.1, 4.2 and 4.3 versus product temperature T_{Pr}.

Thus, the above analysis clearly confirms the thermodynamic feasibility of the solid phase formation of calcium carbide. The reaction between calcium oxide and carbon does not proceed below 1600 K, and it is complete at 2150 K. Calculation of the theoretical energy requirements for the plasma process indicated that the process could lower the energy consumption for the production of calcium carbide by up to 40%. Addition of an inert gas to the reaction lowers the carbon monoxide partial pressure and increases the equilibrium conversion to calcium carbide.

CHAPTER FIVE

"If you can't stand the heat, get out of the kitchen"

Harry Truman (1884-1972)

CHAPTER V 5

EFFECT OF PLASMA TEMPERATURE AND REACTION STOICHIOMETRY

5.1 INTRODUCTION

Experiments were carried out in a plasma spout fluid bed with a DC plasma torch. The reactants were graphite and calcium oxide powder with a mean particle size of 150 μm. Other carbon sources including methane and coke were also used in the study. The reactor was operated in a semi-batch mode; the reactants were fed to the reactor before each experimental run, and the solid products were collected at the end of the run. The exhaust gas leaving the reactor was continuously analyzed for carbon monoxide to measure the rate of reaction.

Experimental results will be presented and discussed in this chapter and the next. Results based on the conversion of calcium oxide to carbon monoxide and microscopic analysis of solid product are presented. The effect of plasma gas temperature, the effect of reaction stoichiometry, and microscopic analysis will be discussed in this chapter.

5.2 CONVERSION

It is essential at the beginning of this chapter to define ***conversion*** as it is used in the thesis. Conversion was calculated based on the amount of carbon monoxide produced. The concentration of carbon monoxide in the exhaust gas was continuously measured and hence the integral volume of CO was determined. Thus, conversion at any time was

calculated as *the moles of carbon monoxide produced per mole of calcium oxide initially fed to the reactor*. The conversion determined by this method was confirmed by analysis of the solid product (acetylene test) according the procedure described in Chapter 3.

5.3 REACTION MECHANISM

Calcium carbide is formed by reacting calcium oxide and carbon according to the following reaction:

$$CaO + 3C \rightarrow CaC_2 + CO \qquad (5.1)$$

This reaction is believed to proceed according the following two-step mechanism first proposed by Kameyama (1956):

$$CaO + C = Ca(g) + CO \qquad (5.2)$$

$$Ca(g) + 2C = CaC_2 \qquad (5.3)$$

Tagawa and Sugawara (1962) studied the solid phase reaction of carbon and calcium oxide in pellets and found that interdiffusion between the two reactants occurred at temperatures above 1273 K and resulted in a solid interstate compound CaO.C. The diffusion of carbon into calcium oxide and vice versa was believed to be the controlling step. Mukaibo and Yamanka (1955) studied the kinetics of reaction (5.2) by heating pellets of calcium oxide and carbon between 1473 and 1673 K under vacuum. They found the reaction to be zero-order and the reaction rather than diffusion was the rate limiting step.

It is accepted that reaction (5.3) is an essential step in the formation of calcium carbide through the surface reaction of calcium vapour and carbon. However, the mechanism by which calcium vapour and carbon monoxide are formed in a solid phase reaction is not well understood. There has not been any experimental evidence in the literature that supports the direct diffusion of carbon into calcium oxide, nor has there been any proof of the generally used two-step mechanism. Hellmold and Gordziel (1983) proposed a model based on the following ionic interdiffusion:

$$O^{2-} + C_n = CO + C^{2-}_{n-1} \qquad (5.4)$$

$$C^{2-}_{n-1} + Ca^{2+} = Ca(g) + C_{n-1} \qquad (5.5)$$

This idea of ionic diffusion was also discussed by Müller (1990a) who proposed a crystallographic model describing lime as a composite of two equal crystal forms of oxide: cubic [CaO(c)] and expanded [CaO(n)]. Müller indicated that ionic diffusion is the only means of carbon transport into the CaO lattice and of reducing the oxide to Ca (g). The reaction sequence starts by ionization of the carbon materials; diffusion of ions into the oxide lattice and formation of an "interstate" compound (CaC_3O); and reaction with the expanded oxide as follows:

$$\text{I} \qquad n(C_3 \rightarrow C_2^{2-} + C^{2+}) \qquad (5.6)$$

$$\text{II} \qquad -Ca^{2+}\text{-}C_2^{2-}\text{-}C^{2+}\text{-}O^{2-}\text{-} = CaC_3O \qquad (5.7)$$

$$\text{III} \qquad CaC_3O + 2CaO(n) = 3Ca(g) + 3CO \qquad (5.8)$$

According to Müller (1990c), it is the role of the carbon materials to provide the C_3 molecules to initiate the ionization, form CaC_3O and eventually form calcium vapour.

Once formed, calcium vapour reacts with either the diffused carbon at the surface of the oxide or with the free carbon to form calcium carbide. In either case, it is this surface reaction that controls the overall rate of formation of calcium carbide. The initiation of the reaction and therefore the initial rate depends on the ability of the carbon to ionize and diffuse into the oxide lattice.

In carbon reduction of most metal oxides, the slowest and the controlling step in the mechanism is the Boudouard reaction (Chapter 2). Carbon dioxide is also believed to play an important role in the reduction of calcium oxide to form calcium carbide, but the reduction mechanism is expected to be different from that of other oxides. The metal, calcium vapour, is a reactant that is involved in the gas-solid reaction. Thus, the formation of calcium carbide is expected to proceed through the following two stages:

Stage I: Initiation step: generation of calcium vapour and carbon monoxide through ionic diffusion

$$\mathbf{CaO + C \rightarrow Ca(g) + CO} \qquad \mathbf{(5.9)}$$

Stage II: Formation of calcium carbide through gas-solid reactions:

$$\mathbf{CaO + CO \rightarrow Ca(g) + CO_2} \qquad \mathbf{(5.10)}$$

$$\mathbf{C + CO_2 \rightarrow 2CO} \qquad \mathbf{(5.11)}$$

$$\mathbf{Ca(g) + 2C \rightarrow CaC_2} \qquad \mathbf{(5.12)}$$

The surface reaction between calcium vapour and carbon (5.12) is the slowest and the rate controlling step. Thus, the ability of the carbon materials to react with calcium is an essential factor in determining the rate of formation of calcium carbide as will be discussed in the next chapter.

5.4 EFFECT OF PLASMA JET TEMPERATURE

Argon at a flow rate of 40 L/min was used to initiate the arc and start the plasma torch. Argon is one of the most commonly used gases in plasma generation. As temperature increases the particle density of argon atoms decreases due to the ionization process, which is completed at about 15000 K (Boulos et al., 1994). The maximum power that was achieved with argon plasma, however, was too low to provide a high enough temperature for good conversion to calcium carbide. Hydrogen was then added to the plasma gas to increase the arc voltage and hence raise the plasma power. For a fixed current (240 A), the arc voltage increased with hydrogen addition, resulting in a power increase from 5kW with pure argon to 18 kW with 67% hydrogen. This increase in plasma power was found to be linear with increasing hydrogen concentration in the plasma gas as shown in Figure 5.1. Hydrogen addition increases the power as well as the thermal conductivity and the heat capacity of the plasma gas. This results in an increase in both the enthalpy and the temperature of the plasma jet. The jet temperature was calculated by energy balance, over the plasma gas, using a torch efficiency of 60%, which was measured experimentally. The temperature is plotted versus hydrogen concentration in Figure 5.2.

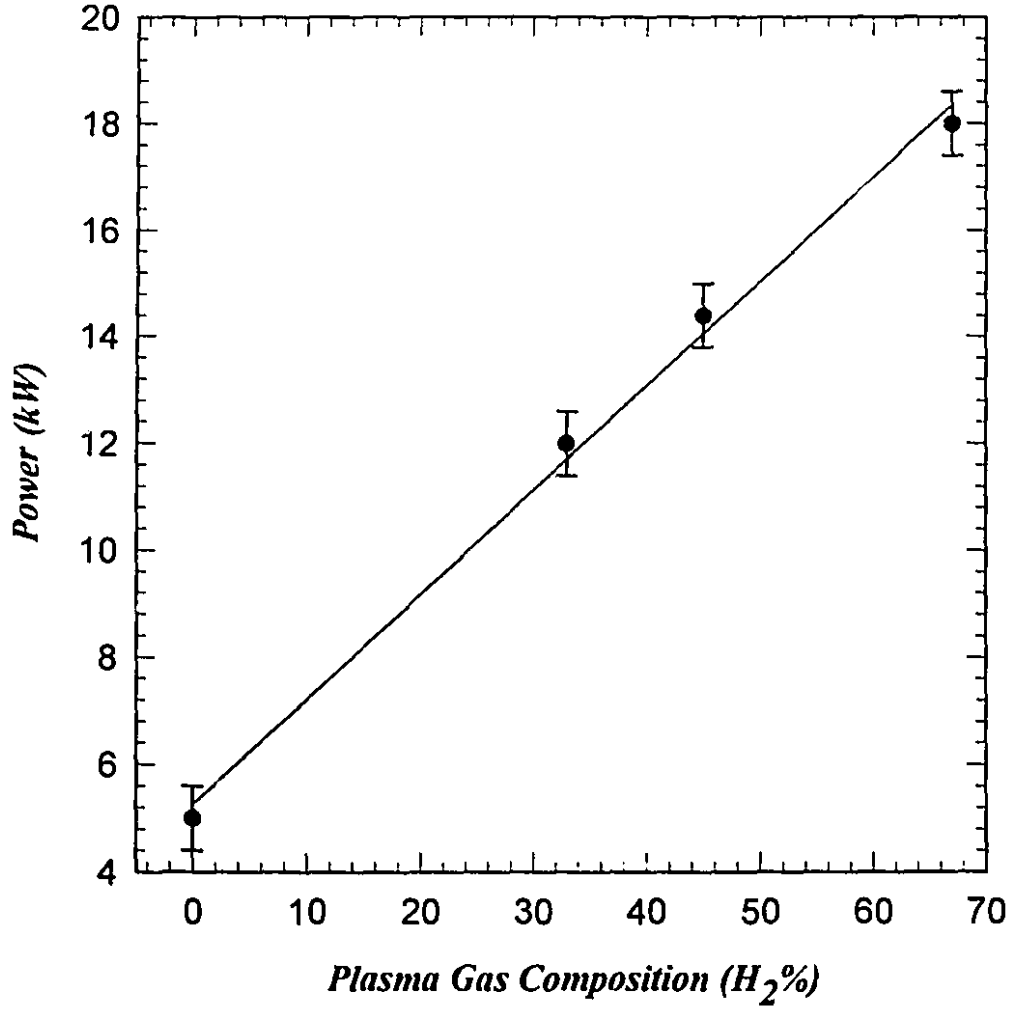

Figure 5.1: Plasma power versus plasma gas composition. Total plasma gas flow rate was 40 L/min and current was 240 A.

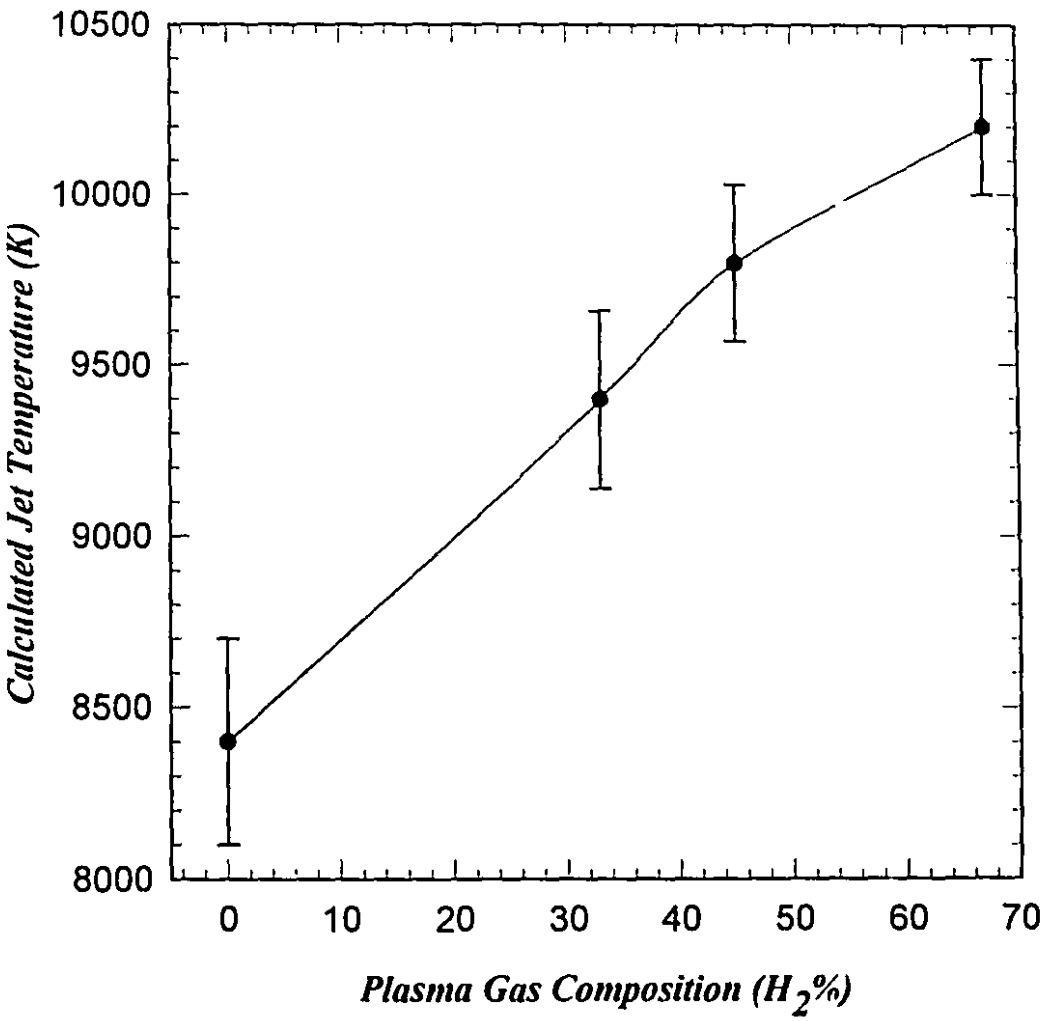

Figure 5.2: Calculated plasma jet temperature versus plasma gas composition. Total plasma gas flow rate was 40 L/min and current was 240 A.

While keeping the current fixed at 240 A, experiments were conducted for different plasma powers by varying the hydrogen concentration in the plasma gas. Figure 5.3 shows a plot of the integral conversion of calcium oxide as a function of run time for four plasma gas compositions (H_2, vol% in Ar): 0%, 33%, 45% and 67%. The conversion increased linearly with time, and the rate of conversion increased with plasma power or hydrogen concentration in the plasma gas (EL-Naas et al., 1995). The rate of conversion at any time represents the instantaneous global rate of reaction. This rate was found to be constant for a fixed power (fixed plasma jet temperature) and increased exponentially with increasing plasma jet temperature as shown in Figure 5.4. The reaction rates at different conditions are shown in Table 5.1. One would expect that the rate of conversion would increase with time, since the bed is heating up and the bed temperature is increasing with the run time as shown in Figure 5.5. The fact that the rate is constant indicates that the change in reaction temperature with time is negligible. A plot of conversion versus bed temperature for different conditions is shown in Figure 5.6. The highest conversion (30%) occurred at a bed temperature of 1573 K, which is less than the temperature required thermodynamically for the reaction to proceed (Chapter 4). This clearly indicates that the reaction between the calcium oxide and the graphite did not take place in the bed, but in the vicinity of the plasma jet where the temperature was high enough for reaction. Thus, the fluid bed reactor consists of two different zones: a high temperature jet zone and a well-mixed isothermal bed zone. The size of the jet zone depends on the plasma conditions, mainly the plasma jet enthalpy. Estimation of the size of the plasma jet zone for the different conditions is discussed in Chapter 7.

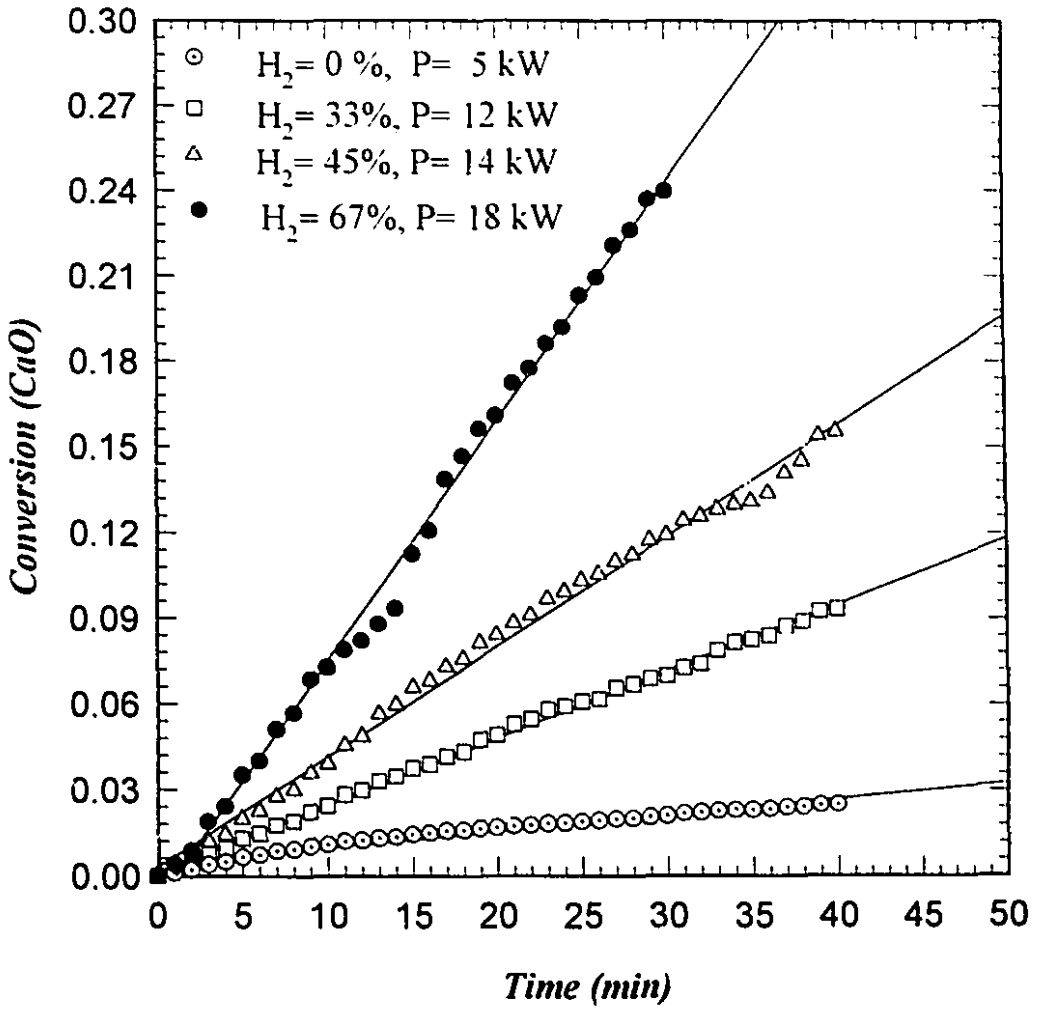

Figure 5.3: Conversion of calcium oxide to carbon monoxide as a function of run time for different plasma powers. Carbon to calcium oxide molar ratio was 3:1 and plasma gas flow rate was 40 L/min.

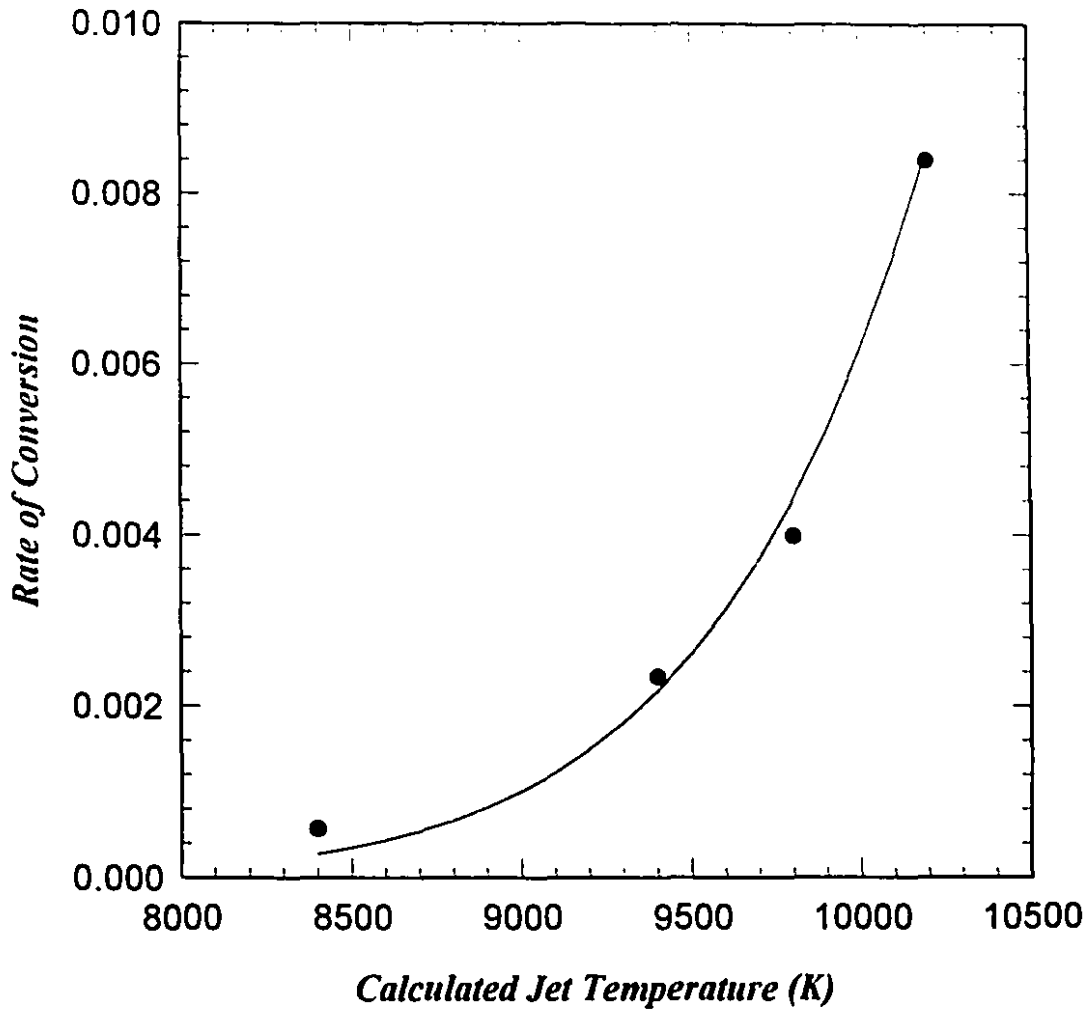

Figure 5.4: Rate of conversion versus calculated plasma jet temperature.

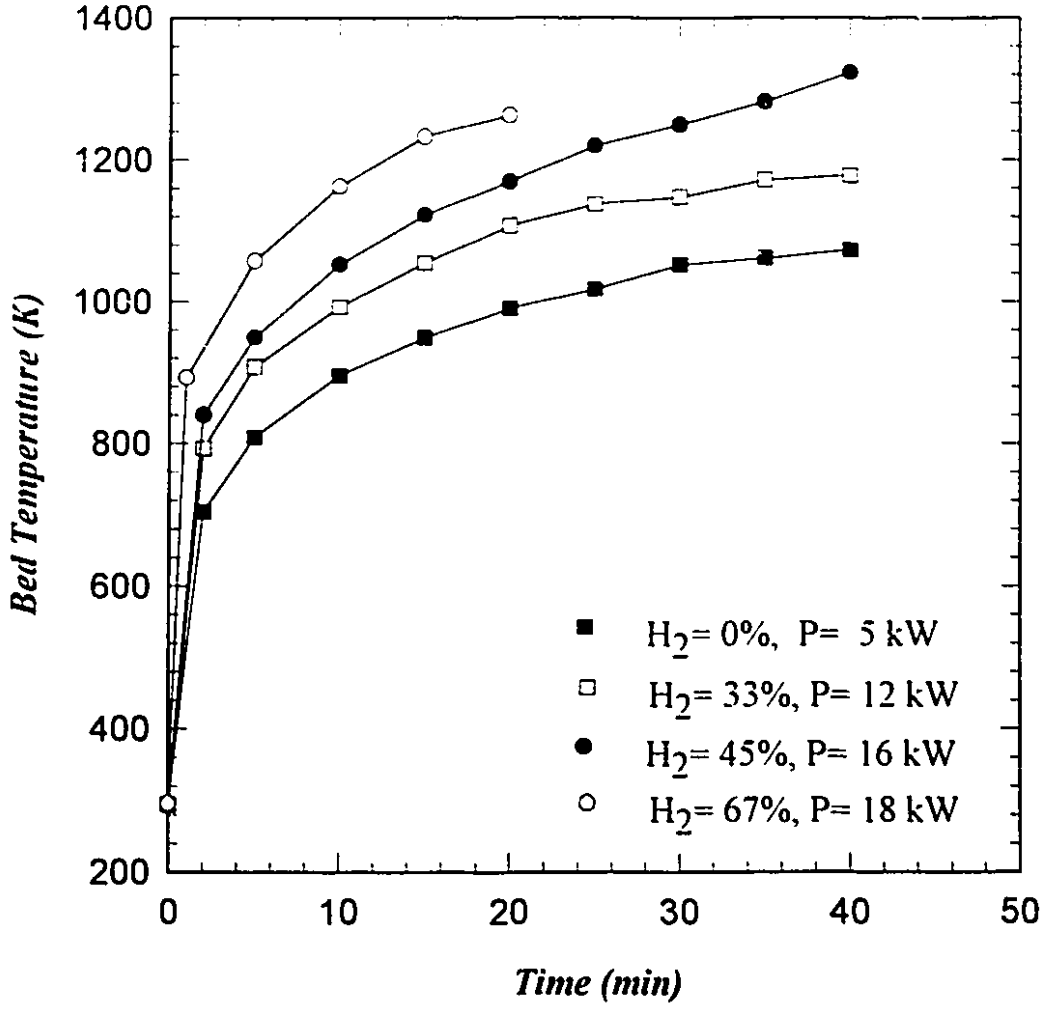

Figure 5.5: Bed temperature versus run time for different plasma powers. Plasma gas flow rate was 40 L/min and current was 240 A.

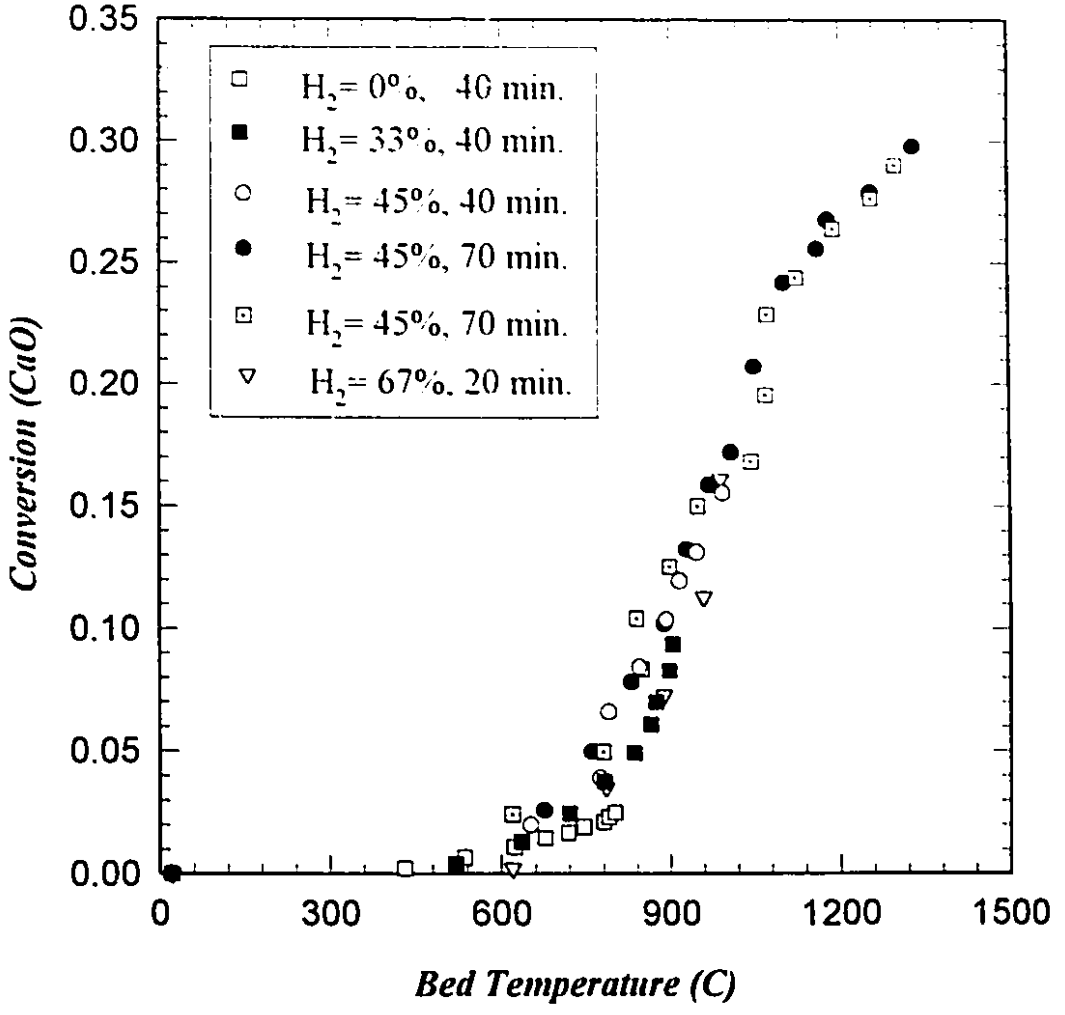

Figure 5.6: Conversion of calcium oxide to carbon monoxide versus bed temperature at different plasma powers. Carbon to calcium oxide molar ratio was 3:1 and plasma gas flow rate was 40 L/min.

Table 5.1: Reaction rates at different conditions

H_2 (Vol.%)	*Power (kW)*	*Calculated T_{jet} (K)*	*Reaction rate (mol/min)*
0	5	8400	0.006
33	12	9400	0.026
45	14	9800	0.042
67	18	10200	0.091

The bed zone, which represents most of the reactor volume, acts as a mixing zone that feeds particles into the jet where they react. As particles enter the jet, their temperature rises from bed temperature (T_B) to a maximum particle temperature (T_P). Except for the first 4 to 5 minutes of each run, the rate of increase in the bed temperature is relatively small. On the other hand, the increase of the particle temperature as particles pass through the jet is very high. Thus, the difference in bed temperature for the whole run is much smaller than the particle temperature gain in the jet (T_P-T_B). This means that the temperature (T_P), which determines the surface reaction temperature, is almost constant with time. This explains the constant rate of reaction despite the continuous heating of the bed. Calculations of the particle temperature, the mean reaction temperature and the particle circulation rate will be discussed later.

It should be noted here that plasma power could be varied by two mechanisms. The first is through changing the current while fixing plasma gas composition. The second is through

varying the hydrogen concentration while fixing the current The overall effect of increasing the power by either mechanism is to increase the plasma jet enthalpy and hence the plasma jet temperature. It is expected that hydrogen addition affects the rate by raising plasma power and enthalpy and not by involvement in the reaction. To verify this point, the hydrogen concentration was kept constant at 33%, while the power was increased by raising the current to equal the power of 45% hydrogen. A plot of conversion versus run time for the three cases is shown in Figure 5.7. Clearly, for the same power the rate of conversion is about the same for different hydrogen concentrations. This implies that hydrogen affects the rate only by raising the plasma power and plasma jet enthalpy.

The influence of an instantaneous jet temperature change on the rate of conversion was investigated by two methods: methane injection into the jet and lowering the current. This was carried out for a plasma gas composition of 67% hydrogen. In the first run, methane was injected (at 11 minutes) into the jet through the spouting port at a flow rate of 4 L/min. In the second run, the current was lowered from 240 to 200 A at 17 minutes, decreasing the plasma power from 18 to 15 kW. Both methods resulted in lowering the jet temperature and consequently the rate of conversion as shown in Figure 5.8.. It is clear that the effect was immediate, which confirms the fact that the reaction is taking place in the jet zone. Also, the sensitivity of the rate to the temperature change suggests that the global rate of reaction is controlled by chemical reaction. The jet temperature was lowered form 10200 K to 8600 K in the first case and to 9500 K in the second case. The rate of reaction was lowered from 0.091 mol/min to about the same level (0.032 mol/min) for

both cases despite the difference in the predicted plasma jet temperature. This is mainly due to the presence of methane as another source of carbon that is more reactive than graphite. The reactivity of graphite and other sources of carbon will be discussed in the next chapter.

5.5 BED STABILITY

The fluid bed reactor, as described earlier, is divided into two zones: the jet zone at the bottom and the bed zone, where most particles are present in the fluidized state. The jet zone is created by positioning the plasma torch at of the bottom of the reactor. Although this arrangement is effective in transferring plasma enthalpy to the bed materials, it creates a high temperature zone where particles may melt and agglomerate. Partially reacted particles soften and agglomerate when reaching a temperature near the melting point of calcium carbide (2573 K, Kubaschewski et al., 1993). The large agglomerates tend to fall into the bottom of the jet, where they combine and form a cylindrical mass around the jet. This occurred while the bed had not reached the required temperature for reaction (1600 K) according to thermodynamic calculations, at 30 minutes for 67% hydrogen and at 70 minutes for 45%, leading to the destabilization of the bed. When this destabilization occurred, the bed temperature and carbon monoxide concentration rose sharply. The solidified mass constricted the jet, making it go higher. As a result, the lightpipe sensor, which was positioned at 11 cm about the distributor, started measuring the jet rather than the bed temperature. Also, the melting produced calcium carbide by liquid phase reaction, which was much faster and resulted in the sharp increase in the carbon monoxide concentration in the exhaust gas.

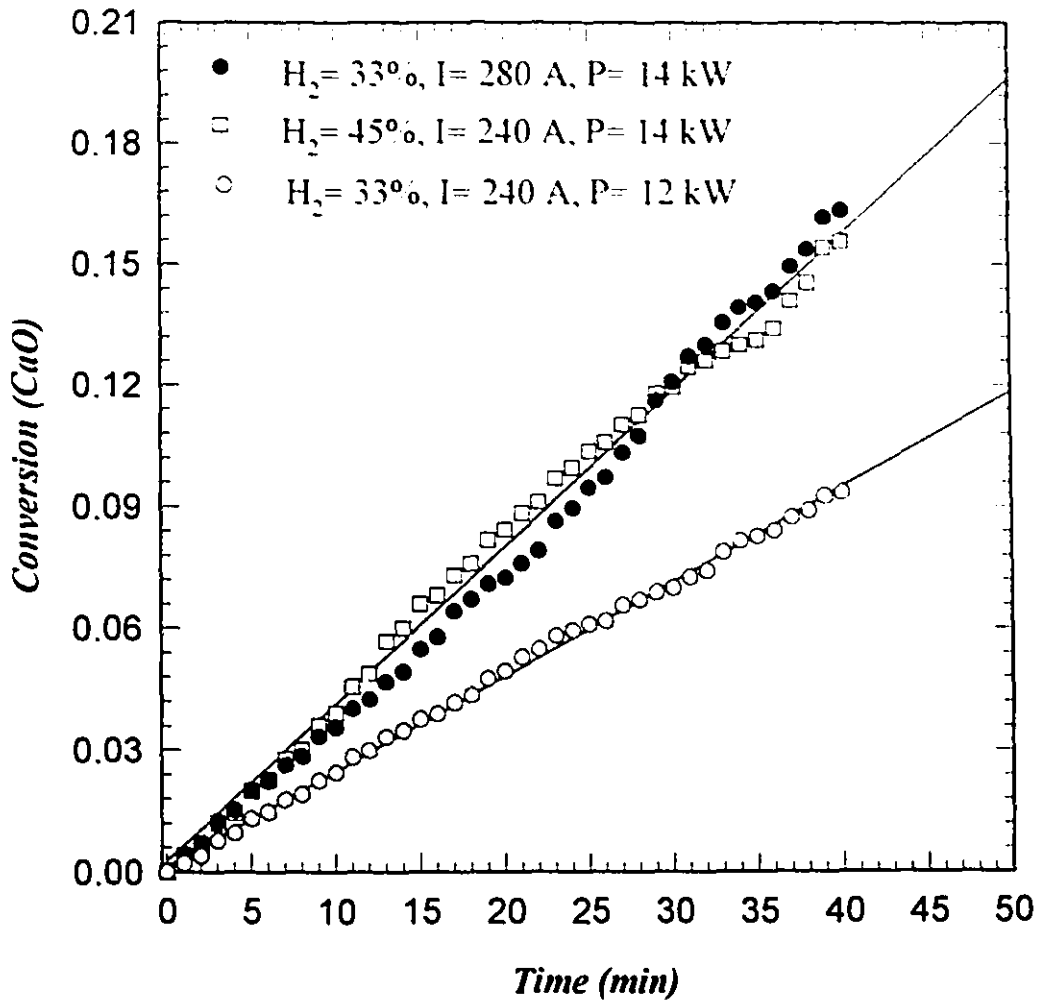

Figure 5.7: The effect of hydrogen addition on the rate of reaction. Carbon to calcium oxide molar ratio was 3:1 and plasma gas flow rate was 40 L/min.

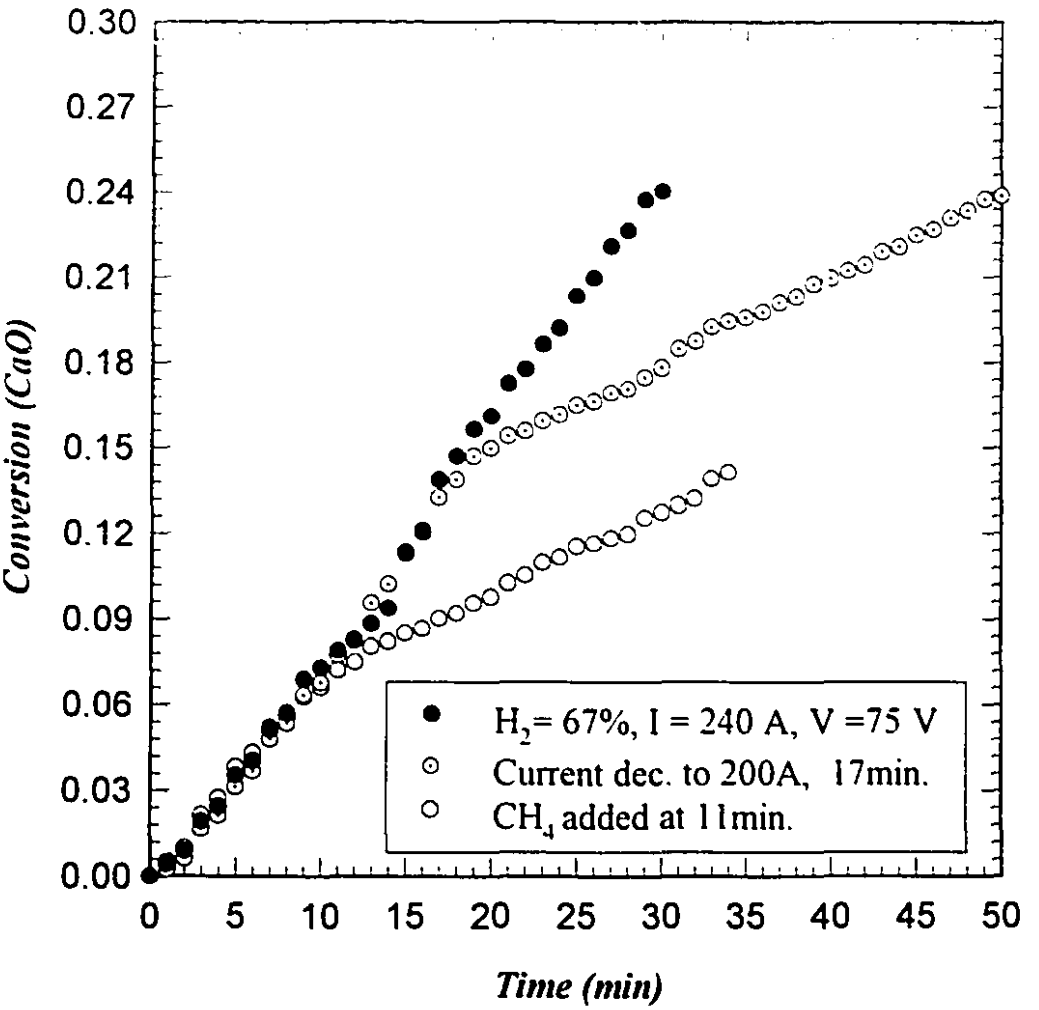

Figure 5.8: The influence of sudden change of plasma jet temperature on the rate of reaction. Carbon to calcium oxide molar ratio was 3:1 and plasma gas flow rate was 40 L/min.

Stable fluidization and reaction were achieved, however, for most conditions (except for 67% hydrogen) up to 40 minutes. The run time was set for most experiments at 40 minutes and only few experiments were run for longer periods. The limiting factor was the stainless steel wall temperature, which was limited at 873 K to avoid damage to the wall. The stability of a run was monitored by stable bed temperature and carbon monoxide concentration. The bed materials collected at the end of each stable experiment showed little agglomeration and no melting. The solids seemed to be well mixed and no segregation was observed.

5.6 EFFECT OF STOICHIOMETRY

Experiments were conducted with excess graphite (1CaO : 6C) and excess calcium oxide (1CaO :1.5 C) to determine the effect of stoichiometry on the reaction rate. A plot of conversion versus run time for the three stoichiometries is shown in Figure 5.9. The reaction with excess calcium oxide, has less carbon and less carbon surface area available for reaction, and hence its rate of conversion is lower than that of the stiochiometric reaction. On the other hand, having excess carbon is expected to lead to a higher rate. The observed rate was higher for the first five minutes and then declined as shown in the figure. This can be attributed to the fact that at the beginning there is a huge carbon surface area available for reaction. Then, calcium vapour, which reacts with carbon to form the carbide, becomes the limiting reactant, therefore, lowering the reaction rate.

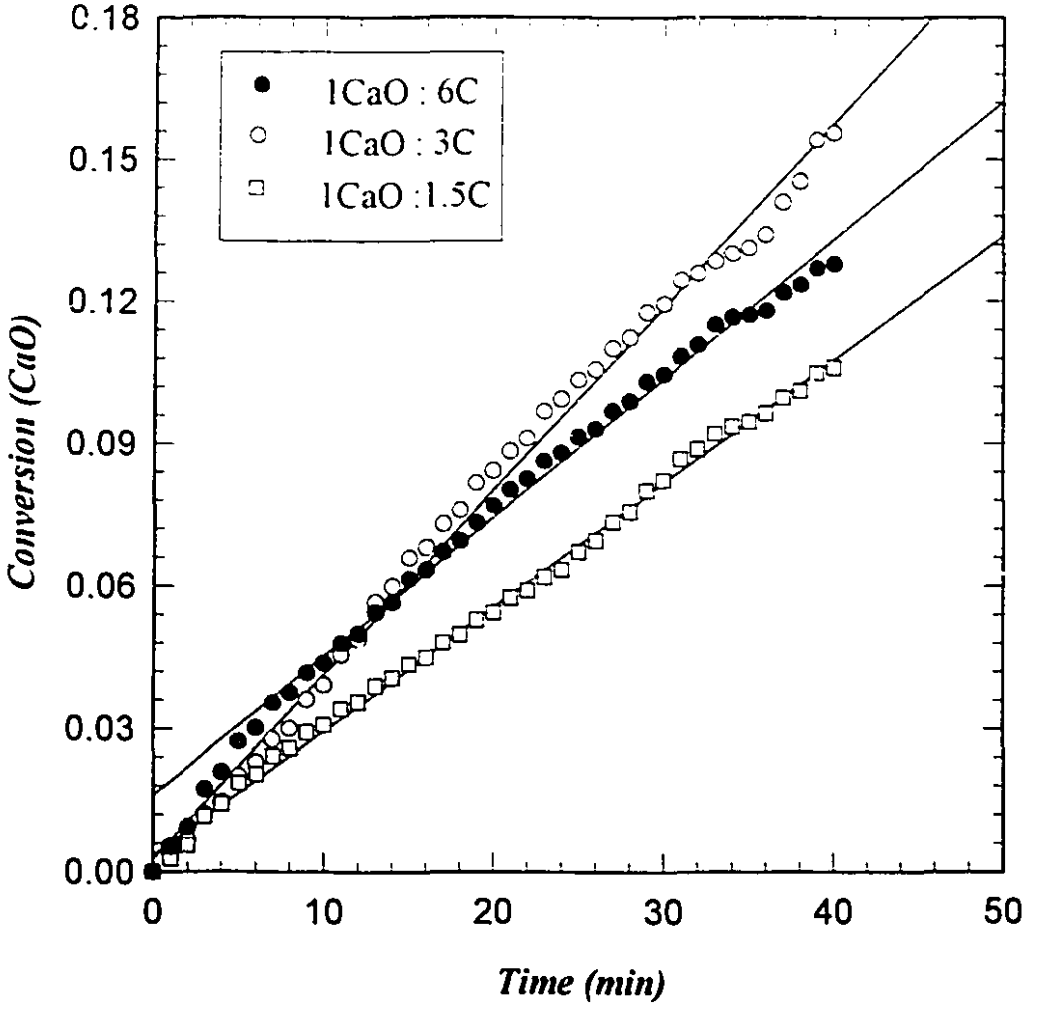

Figure 5.9: The effect of reaction stoichiometry on the reaction rate. Hydrogen concentration was 45% and plasma power was14 kW. Plasma gas flow rate was 40 L/min

5.7 EFFECT OF CaO PARTICLE SIZE

Calcium oxide powder had particle sizes ranging from 53 μm to 1100 μm. This range was divided into two portions in order to investigate the effect of particle size on the rate of formation of calcium carbide. The first portion contained particles greater than 53 and less than 425 μm and had a mean particle diameter of 150 μm . Particles greater than 425 and less than 1100 μm were included in the second portion and had a mean particle size of 600 μm. Each portion was reacted with graphite at a plasma power of 16 kW. A plot for conversion versus time for the two cases is shown in Figure 5.10. Smaller particles exhibited a higher rate of reaction, due to the greater oxide surface area. However, the difference in reaction rate is not significant compared to the difference in particle size (0.048 mol/min for 150 μm and 0.039 mol/min for 600 μm). This low sensitivity to particle size indicates again that the rate is controlled by chemical reaction, since both external and internal mass transfer are known to be much more sensitive to particle size than chemical reaction. For gas solid reactions, the ratio of reaction times needed to achieve a given conversion can be related to the ratio of particle sizes as follows:

$$\frac{t_1}{t_2} = \left(\frac{R_1}{R_2}\right)^n \qquad \textbf{(5.13)}$$

R_1 and R_2 are the radii of particles having the same conversion at different times t_1 and t_2 respectively. The value of the exponent n may be used to infer the controlling mechanism; it is equal to 2 for diffusion control, (1.5-2) for film diffusion control and (1) for chemical reaction control (Wen, 1968). For calcium oxide particles, as shown in Figure 5.10, the value of n is less than unity. In a chemical reaction control mechanism, particle size affects the rate through

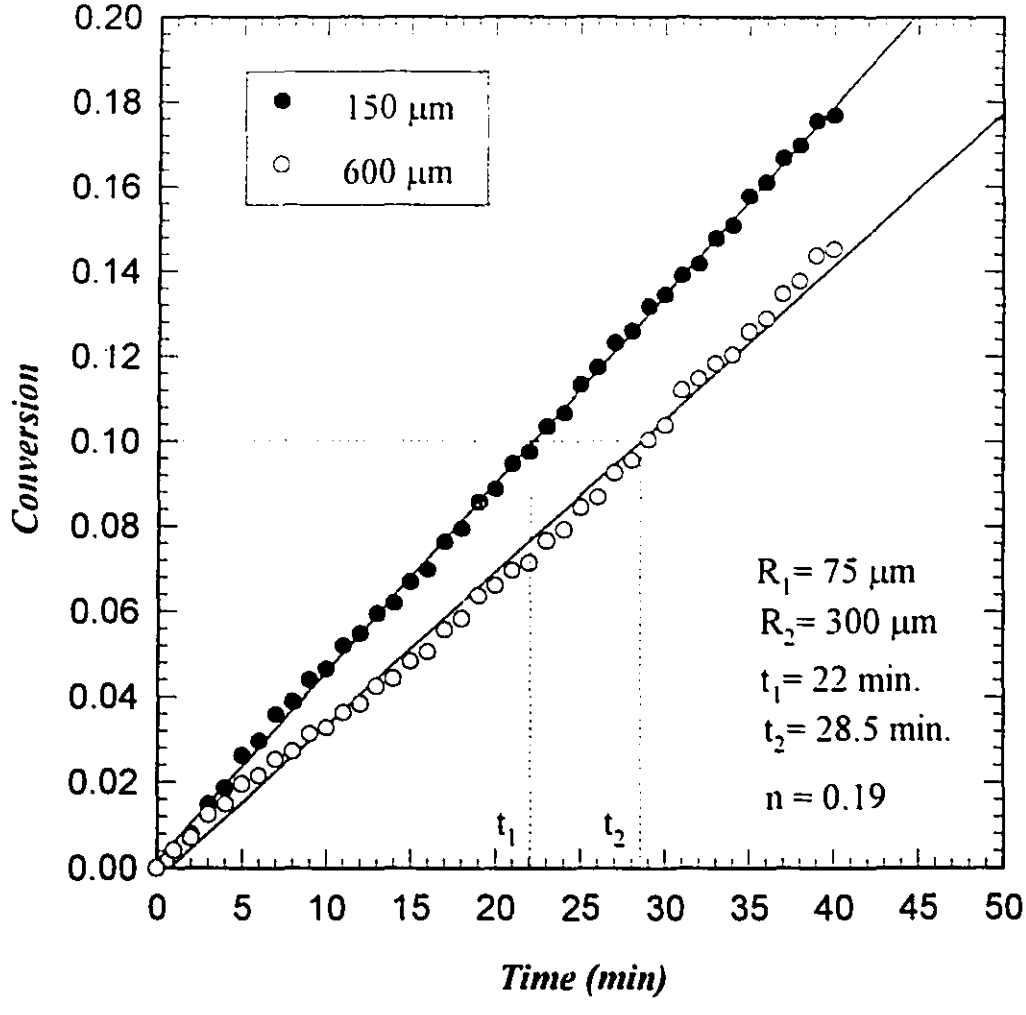

Figure 5.10: The effect of calcium oxide particle size on the reaction rate. Hydrogen concentration was 45% and plasma power was 16 kW. Carbon to calcium oxide molar ratio was 3:1 and plasma gas flow rate was 40 L/min.

surface area. Clearly, smaller oxide particles have larger surface area for reaction. However, because of the high porosity of calcium oxide, the effect of lowering particle size on surface area is minor and consequently, the effect on the rate is small.

5.8 PRODUCT ANALYSIS

5.8.1 Visual Observation

The bed materials were examined visually after every experimental run and samples were taken for analysis. In all experiments, except for pure argon, the solid materials looked black in colour and no white solids were observed. For the lowest power (0%H_2), however, the bed contained some grayish, white solids. For stable experiments, where no melting and agglomeration occurred, the bed materials looked very well mixed and showed no segregation. A considerable amount of elutriated fines were observed for all experiments on the walls of the disengaging section and in the filter and ranged from 8 to 15 (wt.%) of the feed materials, depending on the length of the experimental run. When melting and agglomeration took place, the bed contained 10 to 20 (wt. %) agglomerated particles (1-3 mm), and a fused mass of solids at the bottom, creating a conical shape around the exit of the torch nozzle.

5.8.2 Product Identification

Samples of the solid product were reacted with water to identify calcium carbide and to compute the carbide content of the solid product (conversion). The procedure was carried out as described in Chapter 3. Acetylene produced by the reaction was analyzed

by Gas Chromatography for identification. Two other techniques were also used to analyze the solid product, including X-ray diffraction and Fourier Transform Infra Red (FTIR). X-ray diffraction analyses of the product were compared with those of a calcium carbide sample ordered from Anachemia. Before the analysis, the samples were pulverized to very fine powder to facilitate the analysis. The grinding and the exposure of the powder to the atmosphere during the analysis resulted in converting the carbide into calcium hydroxide. Thus, X-ray diffraction for both the solid product and the sample from Anachemia showed only calcium oxide and calcium hydroxide as shown in Figure 5.11. The relative intensity of the oxide and the hydroxide peaks depended on the calcium carbide content of each sample. The sample from Anachemia contained about 80% calcium carbide, and hence it had higher intensity for the hydroxide peaks. The product sample, on the other hand, had about 16% conversion and therefore had more oxide as shown in the figure. The hydroxide peaks are labeled with number (1), whereas the oxide peaks are labeled with number (2). It is emphasized that no calcium carbide peaks were found for either sample. The FTIR technique can be used to show peaks for certain bonds and identify compounds. No FTIR spectra were found for calcium carbide in the literature, and hence it was rather difficult to identify peaks for Ca-C bonds. FTIR spectra for the solid product and the Anachemia carbide were compared and found to have similar peaks as shown in Figure 5.12 .

Although most of the above mentioned techniques were used for qualitative analysis, the results obtained from the acetylene test and the comparison with the known carbide

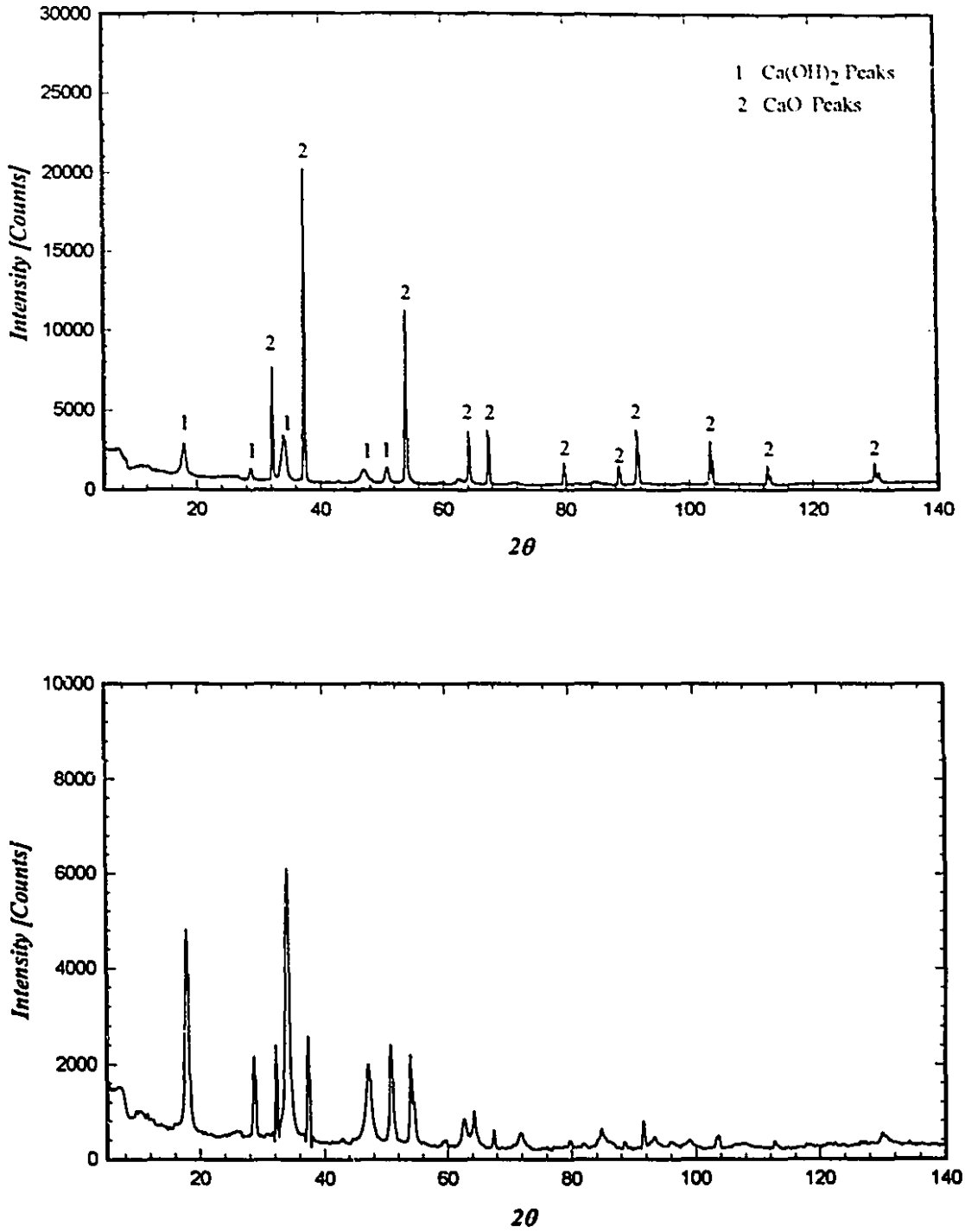

Figure 5.11: X-ray diffraction patterns for the solid product (Top) and the carbidesample from Anachemia (bottom).

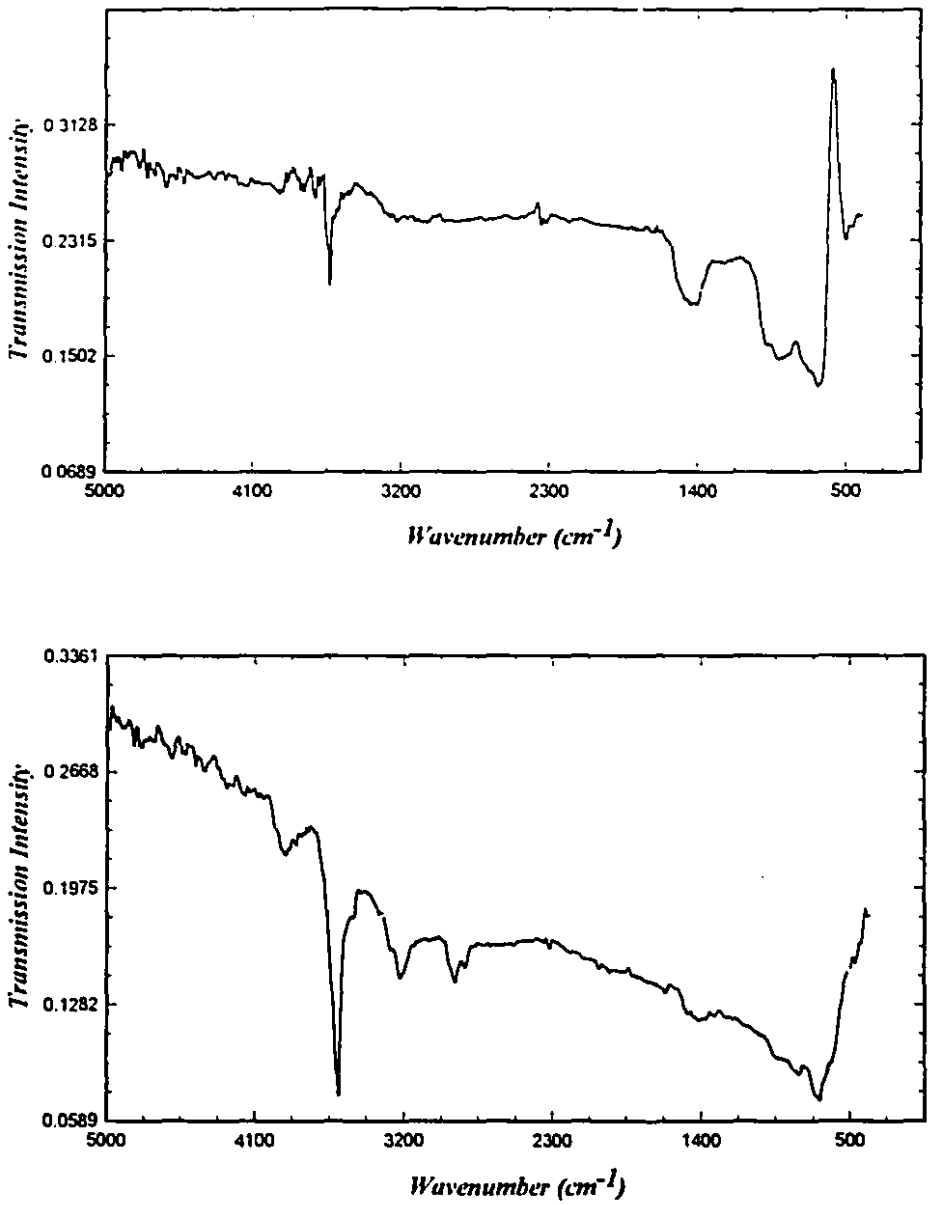

Figure 5.12: FTIR spectra for the solid product (top) and the carbide sample from Anachemia (bottom).

sample form Anachemia clearly indicated that the solid products contained calcium carbide and that the content depended on the operating plasma conditions.

5.8.3 Microscopic Analysis

One of the main objectives of this work was to investigate the morphology of the solid products and to determine whether calcium carbide was formed at the surface of the graphite particles, the oxide particles or both. To achieve this objective, microscopic analyses of the solid reactants and products were carried out according to the procedure described in Chapter 3. Cross sections of particles were examined and elemental spot analysis for calcium, carbon and oxygen was performed. Also, representative particles of unreacted and partially reacted graphite and calcium oxide particles were mapped to determine the relative distribution of calcium, carbon and oxygen. Spot analysis determines the elemental composition in a specific point on the cross section of a particle, whereas mapping gives an overview of the particle showing the region of elemental distribution. It should be noted here that for every product sample, about one hundred particles were examined. All particles examined had similar microscopic views and only a few were chosen for mapping. This observation indicated that all particles in a specific experiment reacted to about the same extent.

Mapping for the different elements proved to be an effective tool in determining profiles for calcium, carbon and oxygen across the unreacted and the partially reacted particles. The distribution of a specific element is determined by brightness in the map. Thus, for a carbon map, for example, the brighter the colour the more carbon and inversely, the

darker the colour the less carbon. Maps for unreacted graphite particles are characterized, as expected, by the presence of carbon and the lack of calcium and oxygen as shown in Figure 5.13 . On the other hand, maps for unreacted calcium oxide particles show calcium and oxygen but no carbon as shown in Figure 5.15. The resin used for mounting the particles was a polymer that contained carbon and possibly some oxygen, and hence it looked bright for carbon and oxygen maps but dark for calcium maps as seen in all figures.

Maps for a partially reacted graphite particle are shown in Figure 5.14. The apparent feature of both parts of the figure is the topochemical, shrinking core-type reaction. In the carbon map (Figure 5.14A.), the rim is darker than the rest of the particle, indicating less carbon is present at the rim of the particle. On the other hand, in the calcium map the rim is brighter, indicating that the outer edge of the particle has more calcium. The lack of carbon in the rim indicates that it is not calcium carbide. Spot analysis at different points in the rim showed that it contained oxygen and calcium in an atomic ratio of about 2 to 1. This implies that the outer edge of the particle is calcium hydroxide, which is formed as a result of a secondary H_2O-CaC_2 reaction. Calcium carbide is known to be very hygroscopic and upon contact with moisture in the atmosphere, during handling of particles, forms calcium hydroxide and acetylene according to the following reaction:

$$CaC_2 + H_2O \rightarrow Ca(OH)_2 + C_2H_2 \qquad (5.14)$$

Thus, carbon in the calcium carbide layer around the particle was removed as acetylene. This was also observed for partially reacted calcium oxide particles as shown in Figure 5.16. Calcium carbide, therefore, had formed at the surface of both reactants, before it

reacted with water forming calcium hydroxide and losing carbon as acetylene. The microscopic analysis indicated that the formation of calcium carbide proceeded according to the shrinking core model. Calcium vapour reacted with either carbon which diffused into the oxide particles or with free graphite particles to form the carbide according to Equation (5.12). It is important to note at this point that the uniformity of calcium profile in the partially reacted graphite particle (Figure 5.14B) is an indication of the lack of resistance to the diffusion of calcium into the graphite particles. This also supports the idea that the surface reaction (5.12) rather than diffusion is the rate controlling step. The resolution of oxygen maps was not as good as that of calcium or carbon, due to difficulties of oxygen mapping by the Microprobe. Oxygen maps in fact do not add much more information to the above analysis other than showing the presence of oxygen around the partially reacted particles. However, for the sake of completeness, maps for partially reacted graphite and calcium oxide particles are shown in Figure 5.17A and Figure 5.17B respectively.

Figure 5.13 A: Carbon map for unreacted graphite particle.

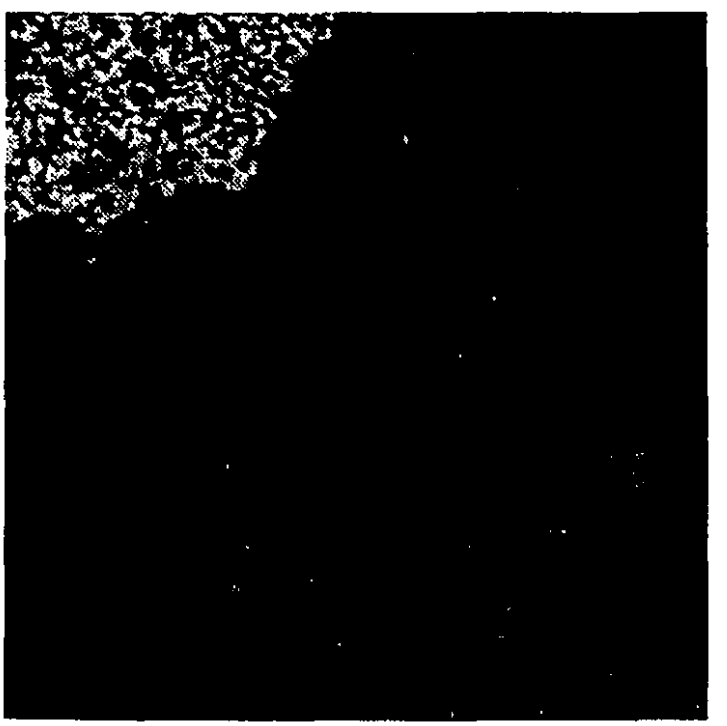

Figure 5.13 B: Calcium map for unreacted graphite particle.

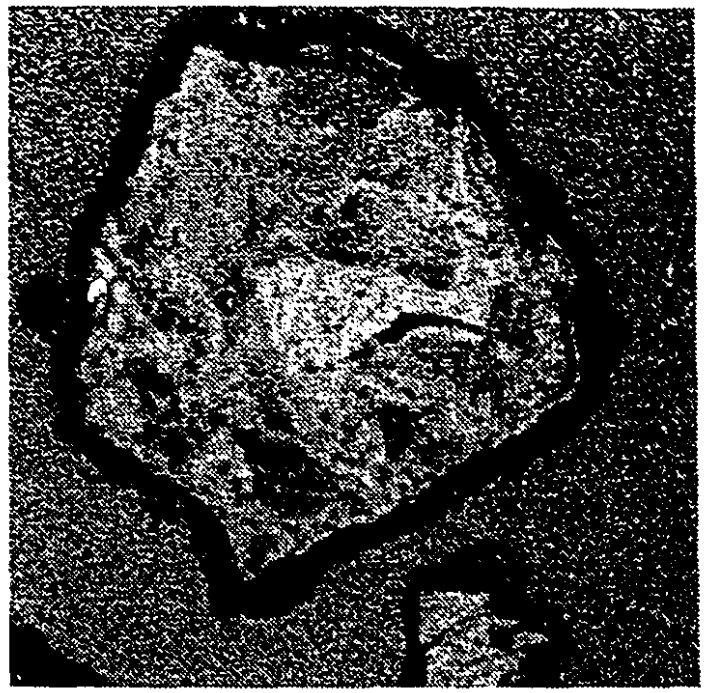

Figure 5.14 A: Carbon map for a partially reacted graphite particle.

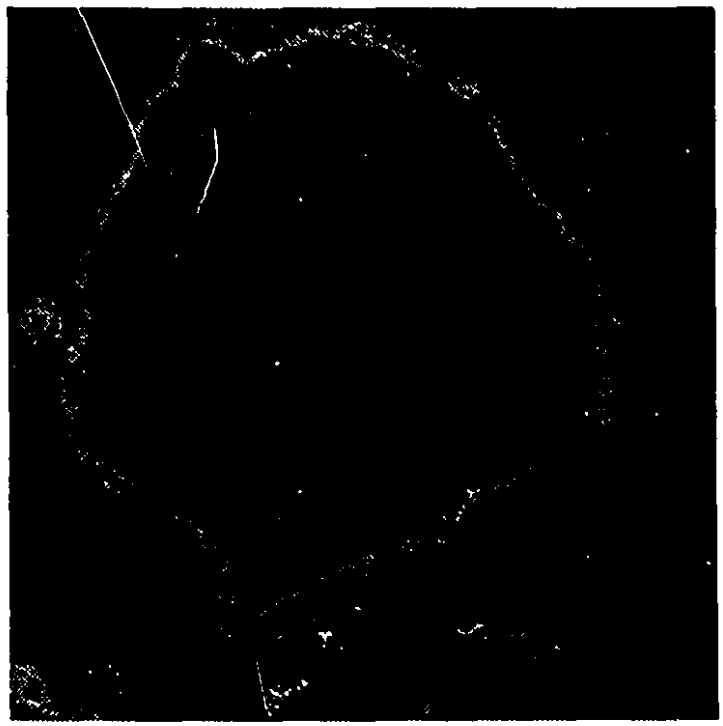

Figure 5.14 B: Calcium map for a partially reacted graphite particle

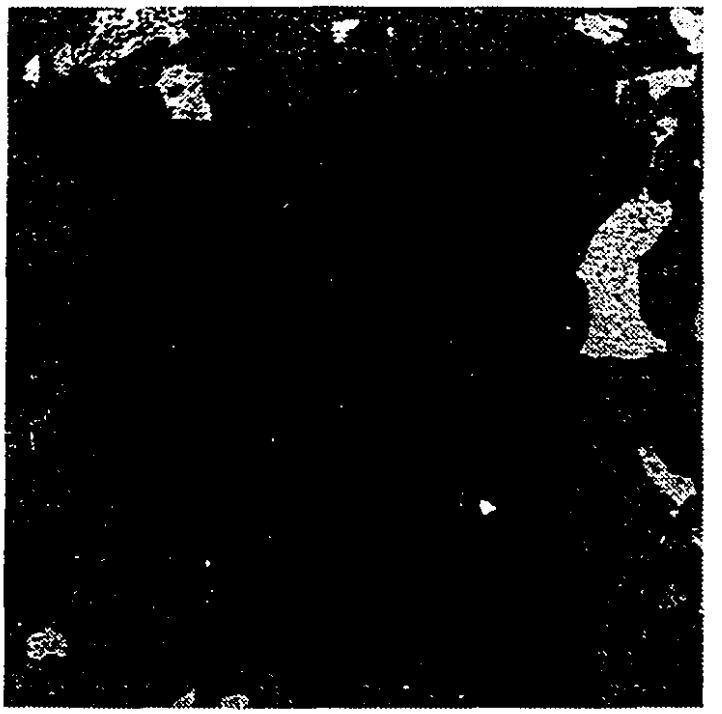

Figure 5.15 A: Carbon map for unreacted calcium oxide particle.

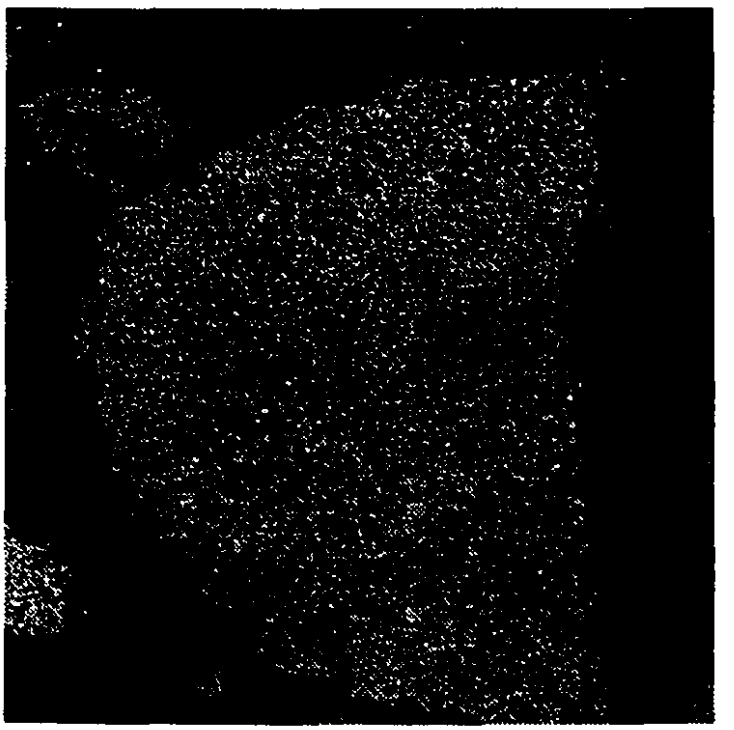

Figure 5.15 B: Calcium map for unreacted calcium oxide particle.

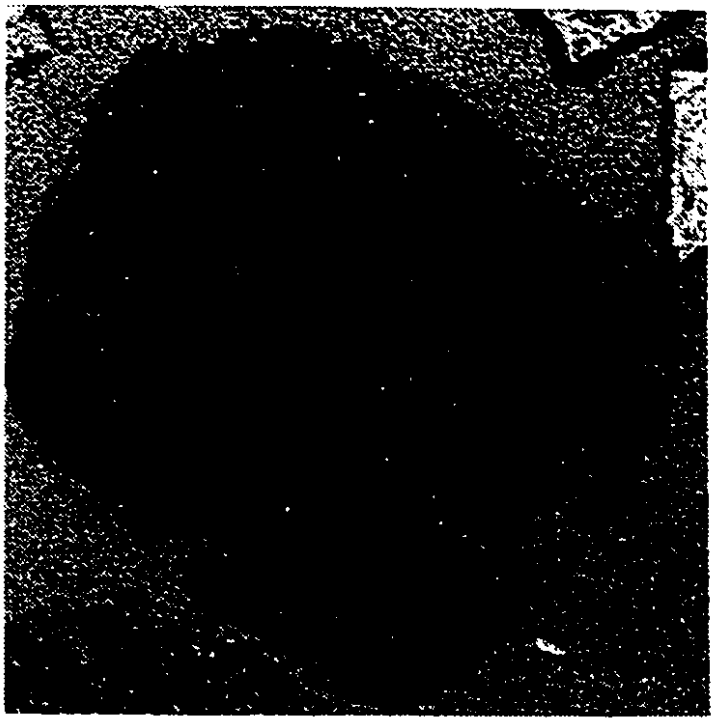

Figure 5.16 A: Carbon map for a partially reacted calcium oxide particle.

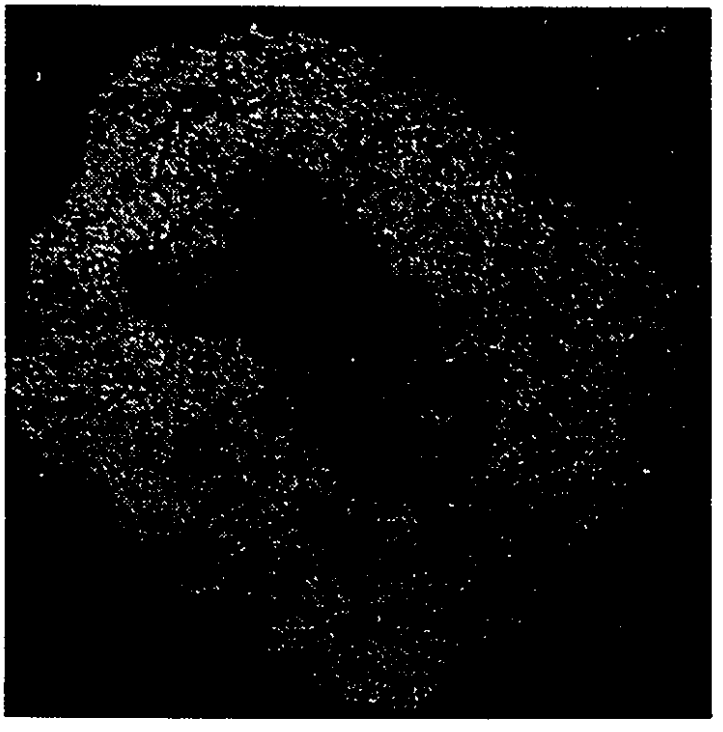

Figure 5.16 B: Calcium map for a partially reacted calcium oxide particle.

Figure 5.17 A: Oxygen map for a partially reacted graphite particle.

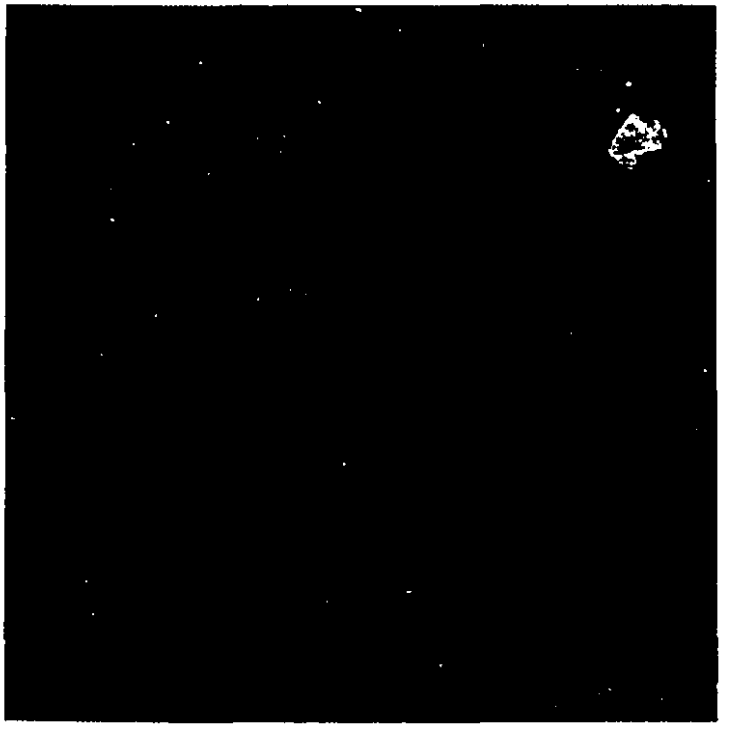

Figure 5.17 B: Oxygen map for a partially reacted calcium oxide particle.

5.8.4 Product Decomposition

Previous studies of the solid phase formation of calcium carbide showed that the calcium carbide decomposed according to the reverse of reaction (5.12), and that the rate was zero order and increased with time and temperature (Tagawa and Sugawara, 1962). The decomposition occurred even at atmospheric pressure as reported by Mu and Hard (1987) and was slowed down by lowering the partial pressure of carbon monoxide. Brookes et al. (1975) stated that the decomposition led to the formation of carbon and calcium vapour. The latter reacted with carbon monoxide according to the reverse of reaction (5.11) and deposited calcium oxide and carbon on cooler surfaces as a grey dust. The researchers also observed a carbide free, carbon ring on the outside of the product layer. In the present study, it was rather difficult to confirm the decomposition of calcium carbide. Although grey dust was observed on the walls of the upper part of the disengaging section and the filter, no carbon layers were observed on the partially reacted particles. Microscopic analysis, as discussed in the preceding section, would clearly detect the presence of any carbon around the particles, but no carbon was found around any partially reacted graphite or calcium oxide particles. It is possible, nevertheless, that decomposition had occurred and that the carbon ring around the particles was stripped off by attrition due to particle movement in the bed. The extent of the decomposition, however, is expected to be minor due to the low carbon monoxide partial pressure, which tends to hamper the decomposition of calcium carbide.

CHAPTER SIX

"All things I thought I knew; but now confess
The more I know I know, I know the less"

Robert Owen (1771-1858)

CHAPTER VI 6

EFFECT OF CALCIUM OXIDE STRUCTURE AND CARBON REACTIVITY

6.1 POROSITY ANALYSIS

The main objective of the porosity analysis was to determine the relative porosity of calcium oxide and graphite; to examine the effect of high temperature on the structure of calcium oxide; and to examine the effect of porosity on the reactivity of graphite. In this section, only results for the porosities of unreacted calcium oxide and graphite will be discussed. Other porosity analyses will be presented in later sections.

Porosity analysis results are presented as plots for cumulative intrusion, incremental intrusion, differential intrusion and incremental pore area as a function of pore diameter. The cumulative intrusion for a calcium oxide sample is plotted versus pressure and pore diameter in Figure 6.1. Porosity is calculated as the total volume of mercury intruded into the sample divided by the sample volume. This calculation includes the volume intruded in between particles; therefore, a correction was needed to obtain the actual internal porosity of particles. It is assumed that the mercury penetrates between particles as the pressure is raised to atmospheric in the low pressure run. Thus, the corrected porosity is calculated as follows:

$$\text{Corrected Porosity } (\varepsilon_C) = \frac{(V_t - V_{atm}).W_S}{V_S}, \quad \text{where}$$

V_t = Total volume intruded (ml/g)

V_{atm} = Volume intruded at atmospheric pressure (ml/g)

W_S = Sample weight (g)

V_S = Sample volume (ml)

A plot of incremental intrusion versus pore diameter for calcium oxide is shown in Figure 6.2. The two different peaks in the plot represent the intrusion between particles (from pore diameter 7 to 100 μm) and intrusion inside the particles (from 0.1 to 7 μm). Incremental intrusions for two other calcium oxide samples are compared with that of the first sample in Figure 6.3. The second sample was taken from the same calcium oxide powder and had about the same mean particle size as the first, while the third sample was screened to have a larger particle size. Clearly, the first peak in the plot seems to be different for the three samples. The reason for this discrepancy is due to the fact that the samples do not have the same size distribution. Although the first and second sample had about the same mean particle size, their individual size distribution could not possibly be the same, and hence the intrusion of mercury between particles was different. On the other hand, because it is the same material with the same internal porosity, the internal particle intrusion for the samples (the second peak) is the same. This fact is even clearer when comparing differential intrusion for the three samples as shown in Figure 6.4. The median pore diameter as shown by the plots is about 1 μm, and the corrected internal porosity for calcium oxide is 50%.

Mercury intrusion into graphite powder was found to be very different from that of calcium oxide. Incremental intrusions for two graphite samples are plotted versus pore diameter in Figure 6.5. Again the two samples were taken from the same graphite powder and had about the same mean particle size but a different size distribution. Intrusion into graphite samples occurred mainly between particles (pore diameter greater than 10 μm) which reflects the low porosity of graphite. Differential intrusions for the two samples are shown in Figure 6.6. A summary of the porosity analysis for graphite and calcium oxide is shown in Table 6.1.

Table 6.1: A Summary of Porosity Analysis

*Sample**	*Mean Pore Diameter (μm)*	*Corrected Porosity(ε_c)*
Calcium Oxide sample I	0.9948	0.500
Calcium Oxide Sample II	0.9657	0.480
Calcium Oxide Sample III	1.050	0.510
Graphite(G-I) Sample I	0.0077	0.028
Graphite(G-I) Sample II	0.0097	0.030

* I, II and III represent repeat analysis of samples from the same powder.

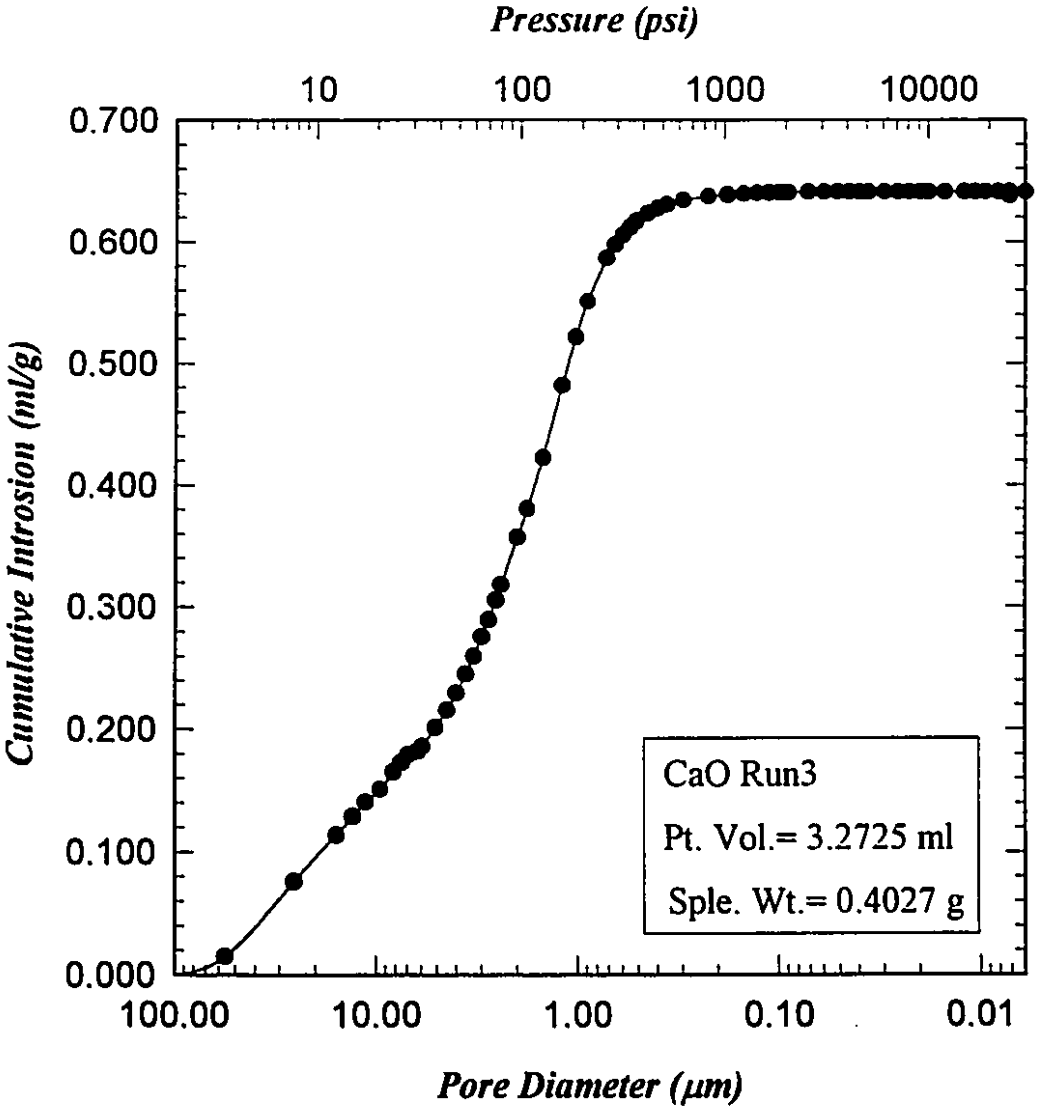

Figure 6.1: Cumulative intrusion versus pressure and pore diameter for calcium oxide.

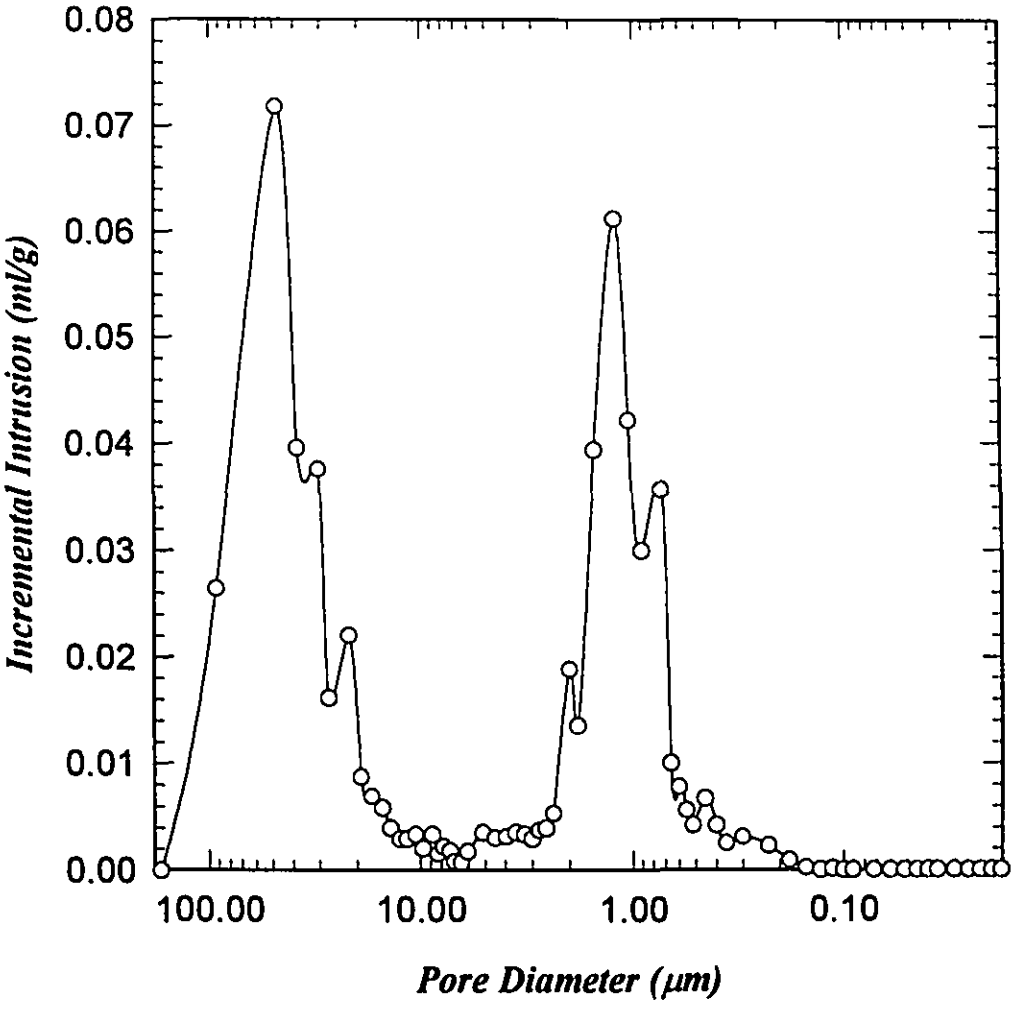

Figure 6.2: Incremental intrusion versus pore diameter for calcium oxide.

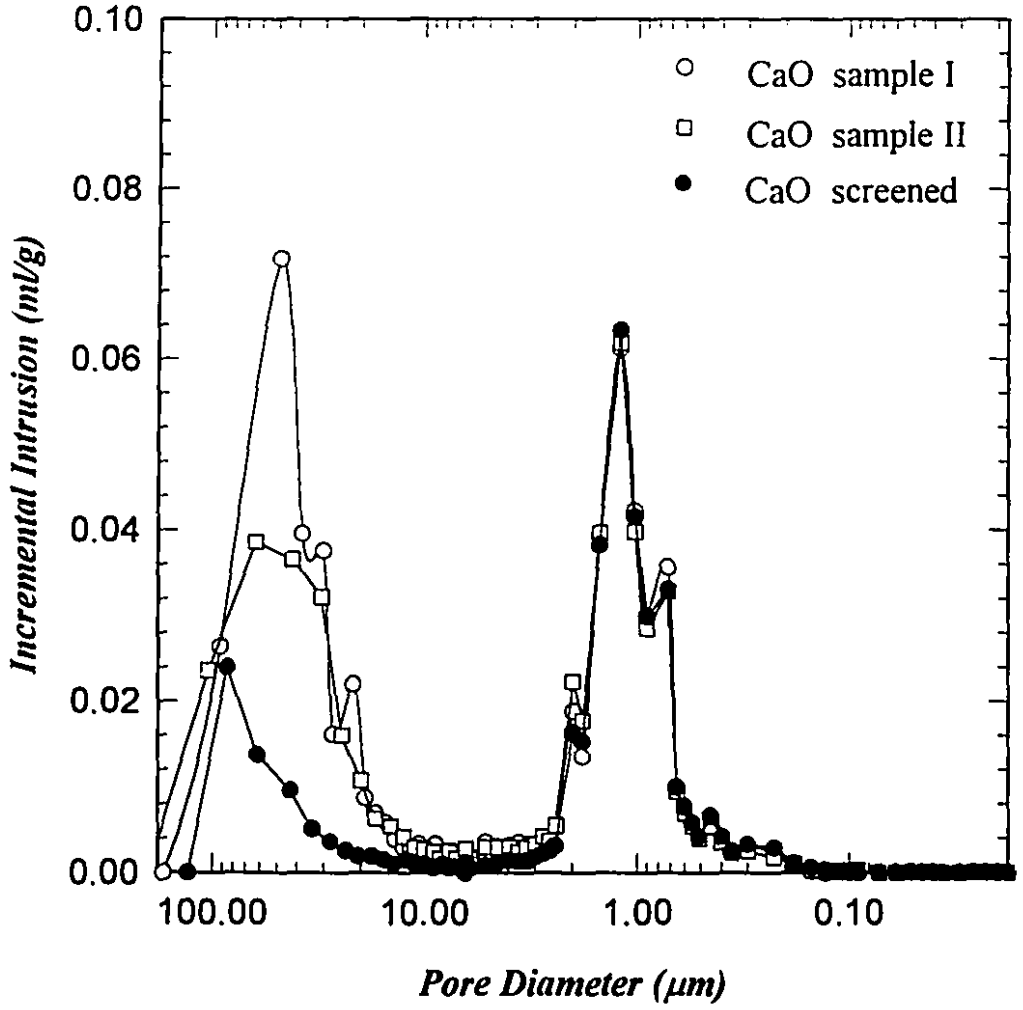

Figure 6.3: A comparison of incremental intrusion versus pore diameter for three calcium oxide samples. I and II represent repeat analysis of samples from the same powder.

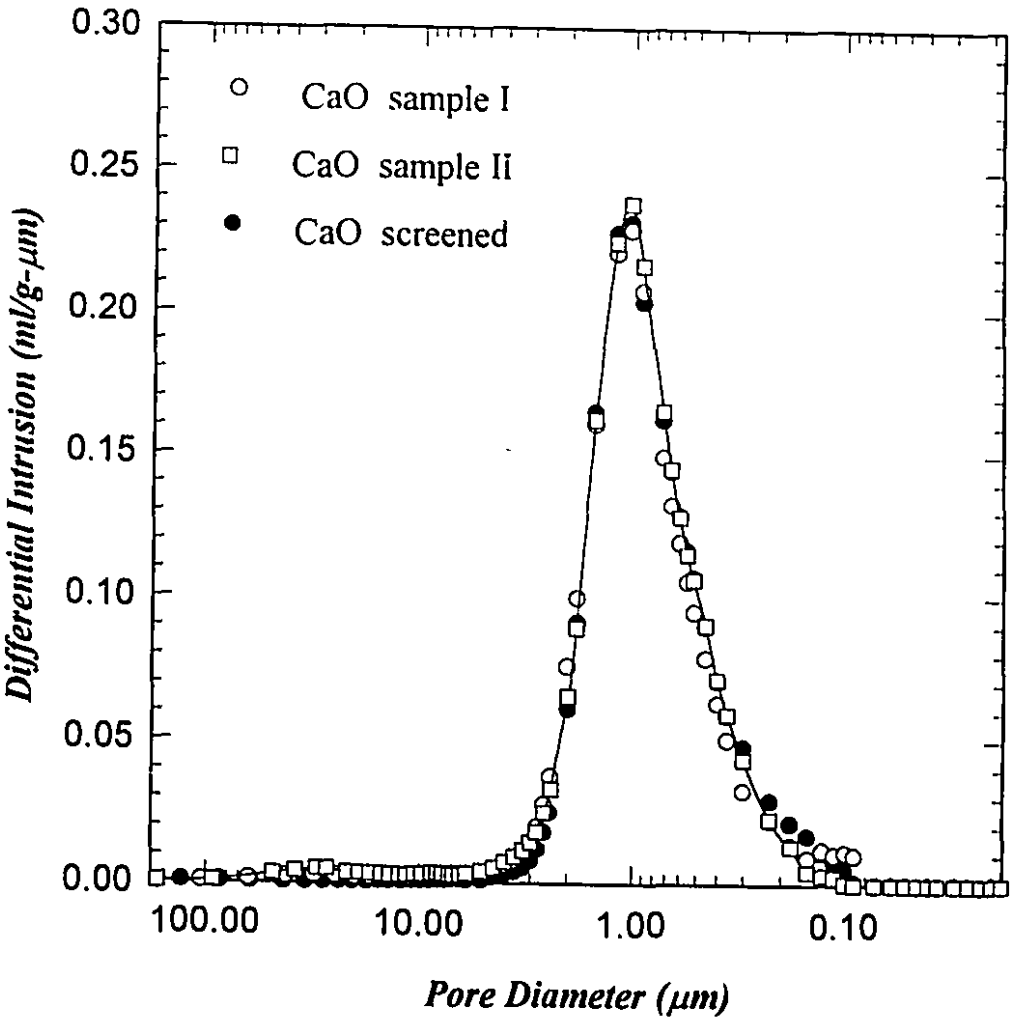

Figure 6.4: A comparison of differential intrusion versus pore diameter for three calcium oxide samples. I and II represent repeat analysis of samples from the same powder

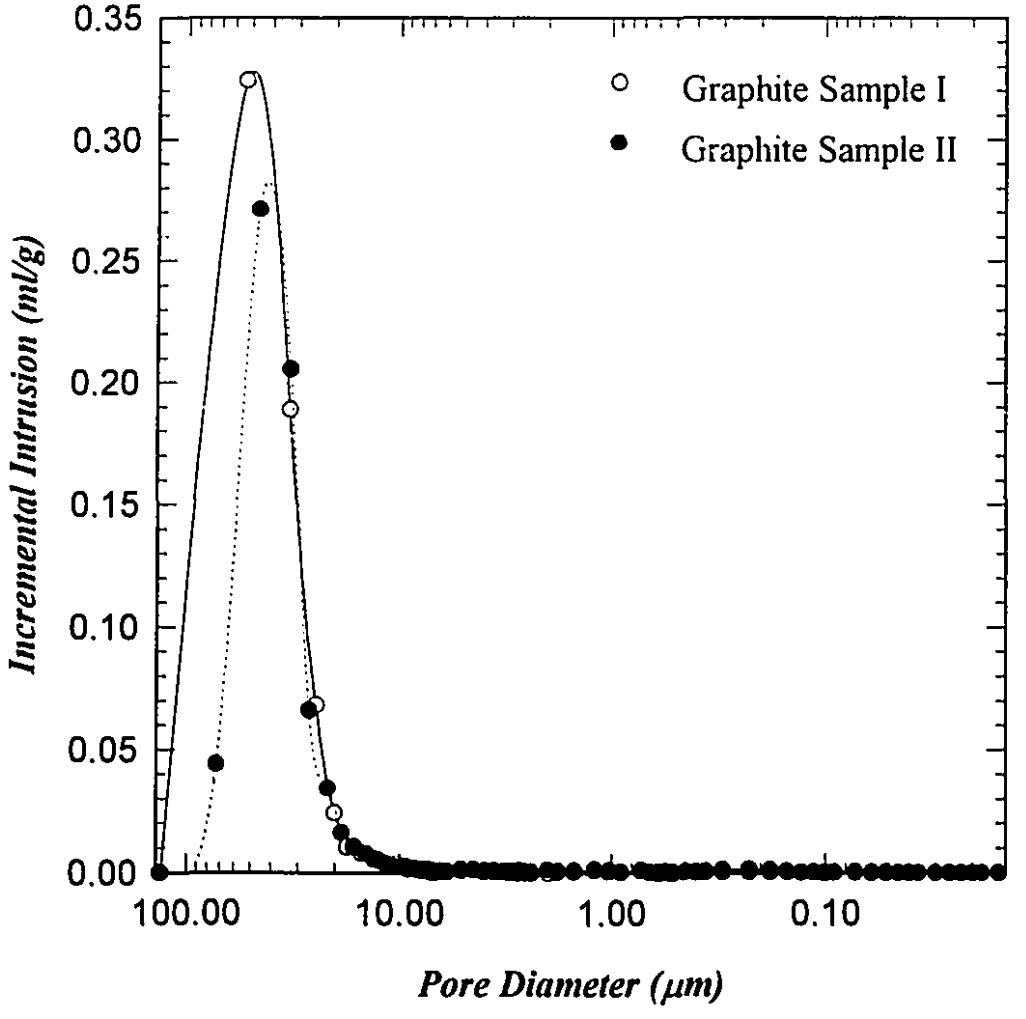

Figure 6.5: Incremental intrusion versus pore diameter for two graphite samples. I and II represent repeat analysis of samples from the same powder

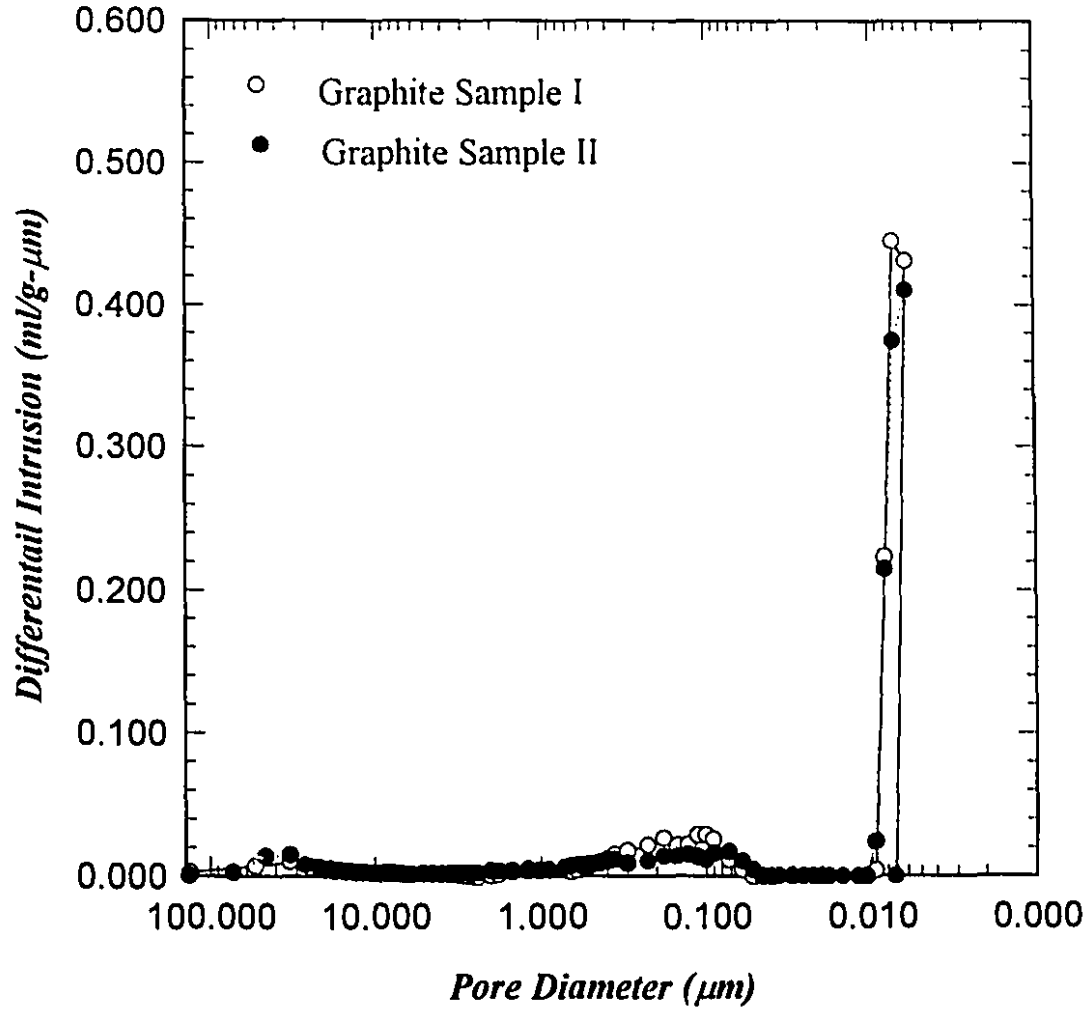

Figure 6.6: Differential intrusion versus pore diameter for two graphite samples. I and II represent repeat analysis of samples from the same powder

6.2 EFFECT OF CALCIUM OXIDE STRUCTURE

Calcium oxide (sometimes referred to as quicklime or calcia) is made by the calcination of calcium carbonate (limestone or calcite) at about 1200 K according to the following reaction:

$$CaCO_3 \leftrightarrow CaO + CO_2 \qquad (6.1)$$

A dissociation temperature of calcium carbonate of 1171 K (at 1 atm) was determined by Johnston (1910) and Mitchell(1923). The free energy of the reaction was measured by Huber and Holly (1967), and the equilibrium temperature was found to be 1170 K. The physical properties of calcium oxide are affected by both the reaction temperature and reaction time. A high burning temperature and long calcination time yield a hard-burned quicklime that has high density, low porosity, and low chemical reactivity. On the other hand, a low burning temperature and short burning duration yield soft-burned, highly reactive limes with low density and high porosity (Boynton, 1980). The calcium oxide used in the present work was described by the supplier to be soft-burned lime.

The atomic structure of $CaCO_3$ and CaO and the changes occurring during calcination were discussed by Azbe (1927). He reported that soft-burned, unshrunk lime contained about 57% voids. Such voids resulted from the loss of carbon dioxide molecules from individual calcium carbonate unit cells. He also suggested that the CaO cells aggregated as the lime was hard burned, filling in the voids and resulting in a less reactive lime. Hedin (1960) explained the shrinkage and increase in density by suggesting that CaO molecules, which are formed through dissociation, unite into progressively larger crystallites. He

calculated that the size of these crystallites increased from 0.1 μm at 1173 K to 1 μm at 1273 K. The development and distribution of pore space in calcium oxide was investigated by Eades and Sandberg (1969) using Scanning Electron Microscopy. They found that calcium oxide was made of small elongated crystallites (0.5-0.6 μm in diameter and about 1.5-2 μm in length). Eades and Sandberg stated that these crystallites were connected with narrow necks or spines to one or more laterally or terminally adjacent crystals of similar size and shape. This description pictures a calcium oxide particle as a porous compact of small non-porous crystallites.

Müller (1990a,b,c) studied the structure, properties and reactions of calcium oxide in burnt lime. He developed a crystallographic model of recrystallised burnt lime, describing CaO as consisting of two equal parts of crystalline oxide: cubic [CaO(c)] and expanded [CaO(n)] characterized by length of valency bonds of 2.41 and 3.91 Å respectively. Müller indicated that in a CaO-C reaction, the two crystal structures react with carbon at different rates. The expanded CaO is reduced at a faster rate and before the cubic CaO is attacked by carbon.

The CaO source used in the present work was high calcium quicklime as described previously (Chapter 3). Its rate of reaction with graphite and methane was found to be constant with time for most experimental conditions. There was, however, a decline in the rate for one case when the reaction time exceeded 40 minutes. At about 44 minutes, the rate of reaction decreased and remained constant at that new value. This trend was

repeatable as shown in Figure 6.7. The change in the rate, which occurred at a bed temperature of (1373 K), can be attributed to one of two factors. The first is as mentioned earlier by Müller that the two crystalline structures of calcium oxide react at different rates. This, however, may not be the case here; because if the expanded CaO[n] represented 50% of the total calcium oxide, the change in rate should only be noticed beyond 50% conversion and not at 25%. It is possible, nonetheless, that the fraction of the expanded CaO[n] is different for different forms of calcium oxide and is not always 50% as reported by Müller. The second factor that can be responsible for the decline in the reaction rate is sintering. The term *sintering* here refers to the phenomenon by which a porous solid, like CaO, increases its bulk density as a result of being held at high temperature. For a particular solid, there is a temperature (Tammann Temperature) below which sintering is slow, but above which it takes place very rapidly. This temperature is usually about 0.4-0.5 times the melting point in the absolute scale (Szekely et al., 1976).

The melting point of calcium oxide is 2843 K (Boynton, 1980). Thus, the temperature at which the rate changes (1373 K) represents 0.48 of the melting point. As this temperature is reached, the sintering of the calcium oxide particles results in a lowering of the porosity, the surface area available for reaction and as a consequence, the rate of reaction. The change of porosity and surface area was investigated by heating a bed of calcium oxide (without graphite) at the same conditions as those in Figure 6.7 for 50 minutes. Porosity analyses were conducted for screened portions (425 to 455 μm) from the heated and fresh

oxide. Differential intrusion and cumulative pore area are plotted versus pore diameter in Figure 6.8 and Figure 6.9 respectively. It is obvious that the amount of mercury intruded into the particles and the pore area are much lower for the heated sample. This clearly indicates that heating the oxide results in shrinkage of the individual particles and a decrease in the internal porosity. The measured porosity of the heated sample was 39% , while that of the fresh oxide was 50%. This decrease in porosity is proportional to the observed decline in the reaction rate. X-ray analysis of both oxides indicated that they had the same crystal structure. This was expected since sintering or hard burning does not shrink the molecular structure, only the spaces between the crystallites as was reported by Mayer and Stowe (1964).

The fact that heating calcium oxide for a long period causes a decrease in surface area and reactivity is an important finding in studying the solid phase formation of calcium carbide. It suggests that the oxide-carbon reaction must take place at high temperature and the residence time must be short to avoid sintering of the oxide particles. This, however, should not be a problem for a continuous plasma fluid bed process. In such a system, reactants are continuously fed and products are continuously removed with the reaction taking place in a high temperature bed.

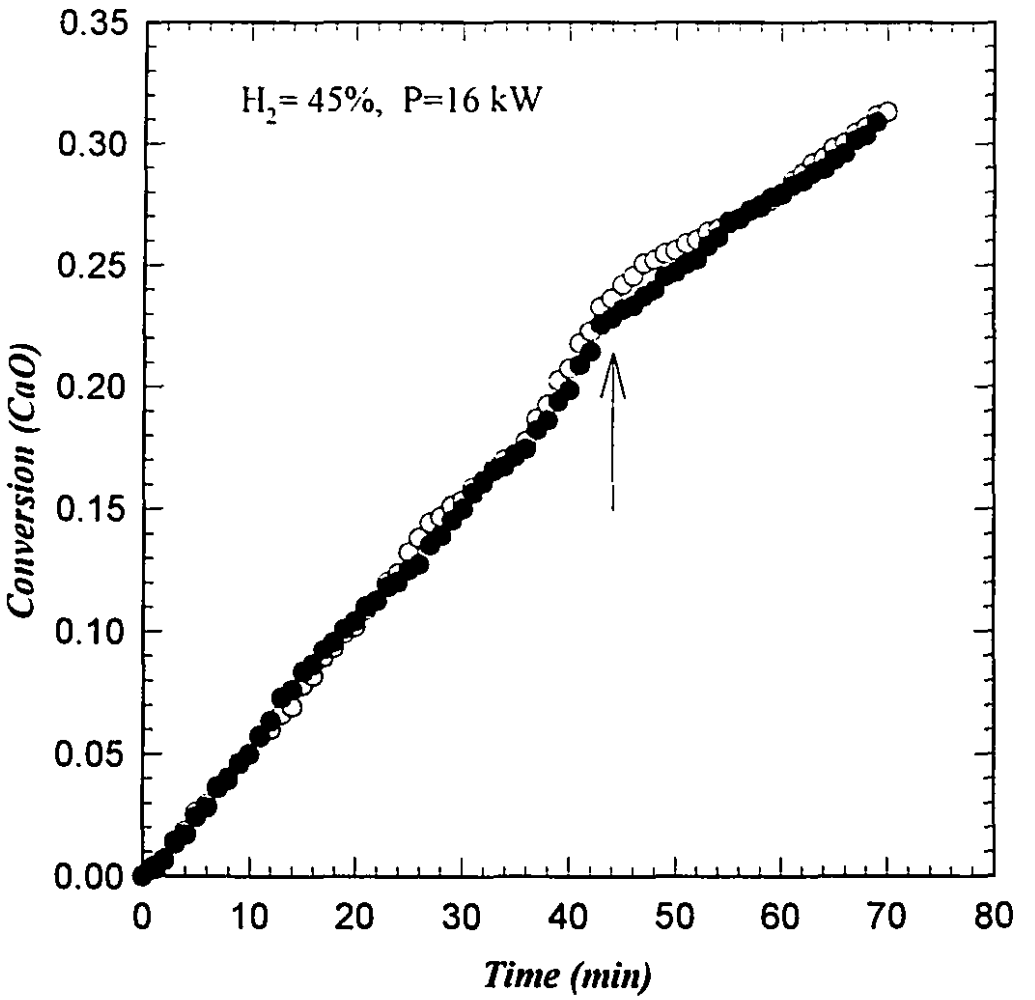

Figure 6.7: Effect of calcium oxide structure on the rate of conversion to carbon monoxide. Carbon to calcium oxide molar ratio was 3:1 and plasma gas flow rate was 40 L/min.

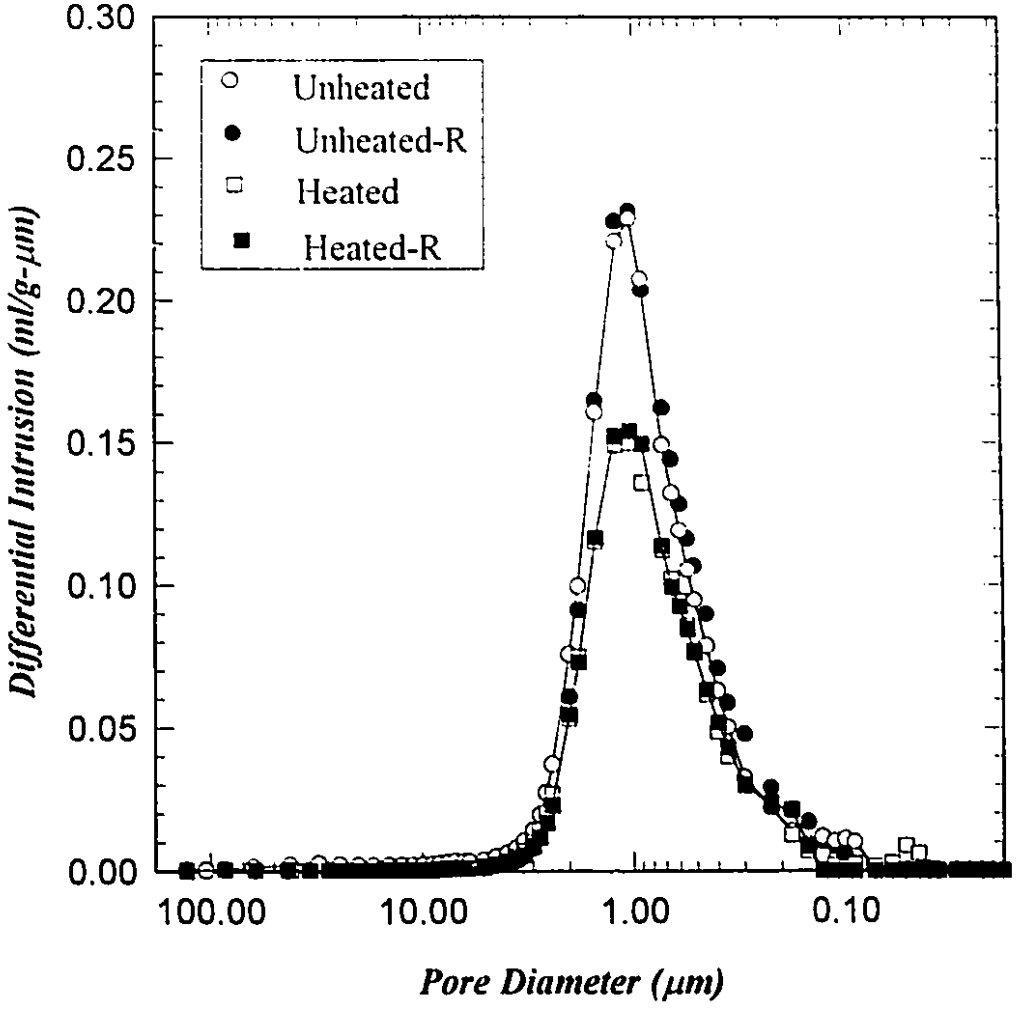

Figure 6.8: A comparison of differential intrusion versus pore diameter for heated and unheated calcium oxide samples. R indicates a repeat analysis.

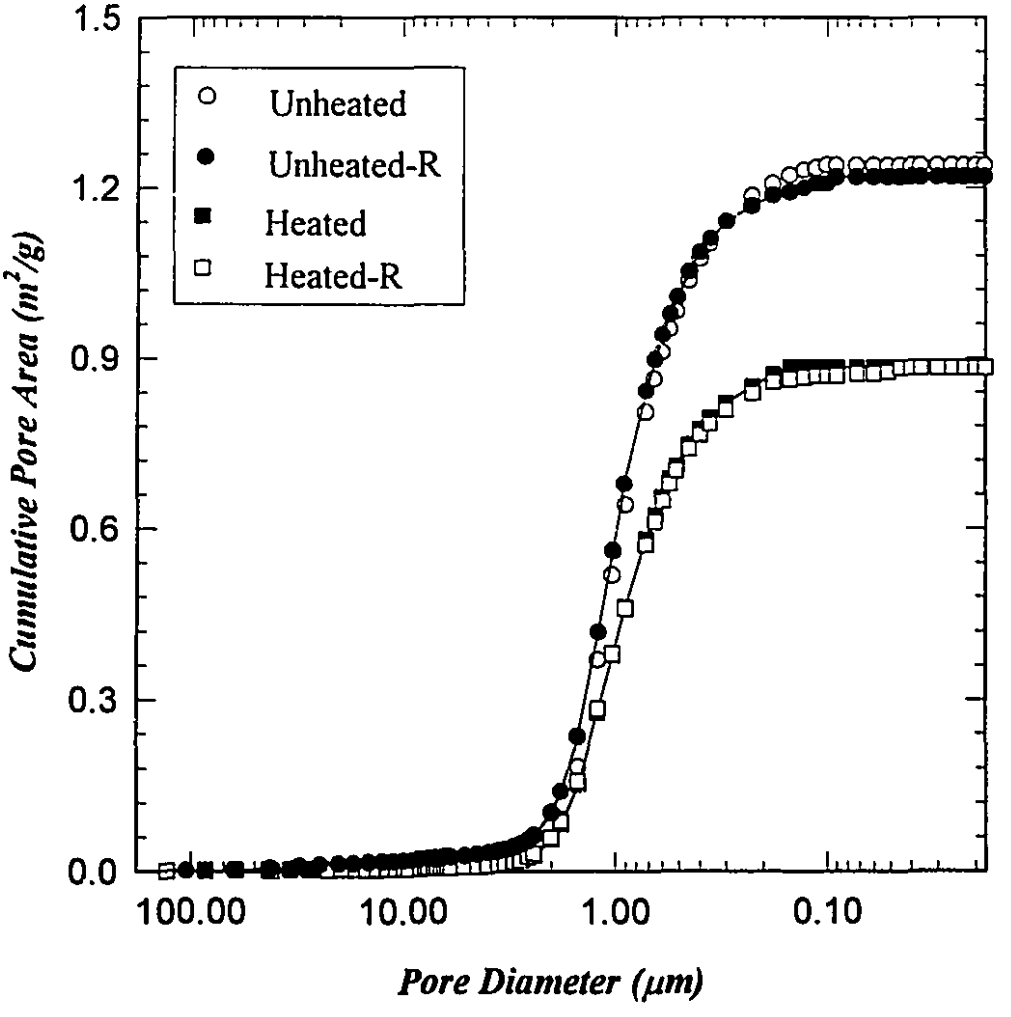

Figure 6.9: A comparison of cumulative pore area versus pore diameter for heated and unheated calcium oxide samples. R indicates a repeat analysis.

6.3 EFFECT OF CARBON REACTIVITY

Carbon reactivity is also an important factor in the solid phase formation of calcium carbide. Carbon can exhibit different reactivities, which depend on factors such as its particulate form, source, accessible surface area, and catalytic effects caused by inorganic impurities (Marsh and Kuo, 1989). The microstructure defines the active carbon surface and thereby the reactivity. The influence of various types of carbon on the reduction of lime was investigated by Hellmold and Gordziel (1983) at 1973 K and 2073 K. They found that at 1973 K, anthracite had by far the highest reactivity with spectral carbon a close second. Graphite and metallurgical coke had the lowest reactivity. At 2073 K, however, the reverse was observed with anthracite being at the bottom of the reactivity scale. Müller (1990c) believes that anthracite is the superior carbon for ionization and diffusion into lime, but inferior for the adsorption of calcium gas and formation of calcium carbide. The role of carbon, according to Müller's ionic diffusion, is to dispatch C_3 molecules for the ionization and formation of CaC_3O and to adsorb calcium gas for the formation of CaC_2. It is the ionization and formation of CaC_3O that initiates the reaction process, resulting in the production of calcium vapour (Equations 5.11), which then reacts at the carbon surface to form calcium carbide according to Equation (5.12). The presence of volatiles in carbon is believed to enhance its ability for ionization, diffusion into the oxide and formation of calcium vapour, whereas a large accessible surface area and a considerable number of active sites can improve the capability of carbon to adsorb and react with calcium vapour. Thus, different forms of carbon can have different abilities for ionization and surface reaction and consequently, different reaction rates.

The influence of carbon source and carbon reactivity on the rate of formation of calcium carbide was investigated in the present work using methane, coke and a second type of graphite powder. Results for the conversion of calcium oxide into carbon monoxide are presented for the three carbon materials and compared with those of the first graphite powder.

6.3.1 Reaction with Methane

Methane was used as a carbon source to react with calcium oxide powder at different plasma gas compositions. It was injected into the reactor in two ways: into the distributor as a fluidizing gas and into the plasma jet as a spouting gas. Methane reacts with calcium oxide as a decomposed fine carbon (soot). Thermodynamic analysis shows that the decomposition of methane is complete at about 823 K. Since this temperature is reached by the bed within the first five minutes for most experimental conditions, the calculation of conversion (from CO analysis) was based on the assumption of complete decomposition.

The conversion of calcium oxide, with methane as the fluidizing gas, is plotted versus reaction time in Figure 6.10. The conversion is linear with time for the three conditions plotted in the figure. Also, the rate of conversion increased with increasing power as was the case for the graphite experiments. There were, however, two major differences between the two cases. For methane, the rate of conversion was much lower, and there was no reaction at the lowest power (5 kW). In this case, the bed temperature for the first

25 minutes was too low (less than 823 K) for methane to decompose completely. A threshold power may be needed for the decomposition of methane and the formation of calcium carbide. Indeed this was reported by Kim et al (1979) who studied the reaction of lime with methane in a rotating-arc reactor. They found that for a constant methane flow rate, there existed a threshold power below which no carbide formed, and for a flow rate of 16-17 L/min, this power ranged from 14 to 16 kW. In the present study, a considerable amount of energy is needed for heating up the bed, for the decomposition of methane and for the formation of calcium carbide, and hence a minimum power (greater than 5 kW) is needed. Methane reacts with calcium oxide as a fine carbon powder and not as a gas. The powder is entrained into the high temperature jet zone, where it reacts with the oxide in the same manner as graphite. It is unlikely, however, that the unreacted fine soot can recirculate into the jet zone due its fine particle size ($\cong$ 0.03 μm, Kim et al, 1979).

It is emphasized at this point that methane was injected continuously, whereas graphite was fed to the reactor at the beginning of each run. Thus, it is difficult to compare the reaction rates for the two forms of carbon. It is possible, however, to make a comparison based on the assumptions that methane decomposes completely and that soot elutriation is minimal. The integral mass of carbon (for the run), from methane decomposition, can then be estimated, and the rate of conversion based on the total carbon can be calculated and compared with that of graphite. On this basis, the rate of carbon conversion (moles of carbon monoxide divided by one third of the total moles of carbon) is higher for methane than for graphite as shown in Figure 6.11. The higher rate is mainly due to the high

carbon surface area available for reaction. As methane decomposes, the fine-powdered carbon (≅ 0.03 μm) has much more surface area and is more reactive than graphite.

Although it was assumed that elutriation was negligible, some soot (decomposed methane) did elutriate during the experimental runs indicating that an even smaller mass of carbon was available to react with calcium oxide. Consequently, the calculated rate of conversion for methane, which is based on the assumption that all the decomposed methane converted to carbon monoxide, is lower than the actual rate. A considerable amount of soot was observed in the filter indicating that not all decomposed methane was available for reaction. Direct injection of methane into the plasma jet is expected to result in a higher rate of reaction. The main advantage of methane injection into the jet is the availability of carbon in the high temperature jet zone. Most of the carbon from the decomposition is available for reaction with the oxide. There were, however, some disadvantages. When methane is injected into the plasma jet as a spouting gas, it lowers the jet temperature by physically quenching the jet and by consuming energy through the endothermic decomposition. The plasma power had to be raised to offset this decline in temperature. This, however, proved to be difficult, because the power required was higher than that could be handled by the torch with the present apparatus. It was always preferred to keep the current less than 300 A to minimize erosion of the copper anode.

Methane at a flow rate of 10 L/min was injected into the plasma jet through the spouting port. The plasma gas composition was 33% hydrogen in argon and the plasma power was

12 kW. The calculated jet temperature for this condition was 9400 K. To compensate for lowering the jet temperature by methane injection, the current had to be raised to 320 A. The current, however, was unstable and fluctuated from 300 to 320 A. Nonetheless, the experiment was run for twenty minutes. The rate of conversion was found to be higher than that observed with methane as the fluidization gas, despite the fact that the jet temperature might have been slightly lower than 9400 K, because of the current fluctuation. The rate of conversion is plotted versus time in Figure 6.12.

6.3..2 Reaction with Coke

Coke powder with a mean particle size of 200 μm was reacted with calcium oxide at a plasma gas composition of 45% hydrogen and a plasma power of 16 kW. The conversion of calcium oxide to carbon monoxide is plotted versus run time in Figure 6.13. For the first five minutes, the rate of conversion was found to be higher than that of graphite under the same conditions as shown in the figure. The rate then dropped to a new and constant value. This behaviour is believed to be due the presence of volatiles in the coke, which react at a faster rate than the rest of the carbonaceous material. It is believed that the presence of these volatiles improves the ability of coke to generate C_3 molecules and to ionize as described previously in the preceding chapter. Tsikarev (1991) studied the reactivity of coke in the electrothermal process for the production of calcium carbide and noted that in the initial period of the process only the external surface of the coke reacted. The fact that the initial reaction rate for coke is fast may indicate that coke is effective for the ionization and the formation of calcium vapour, but not as effective as graphite for the surface reaction.

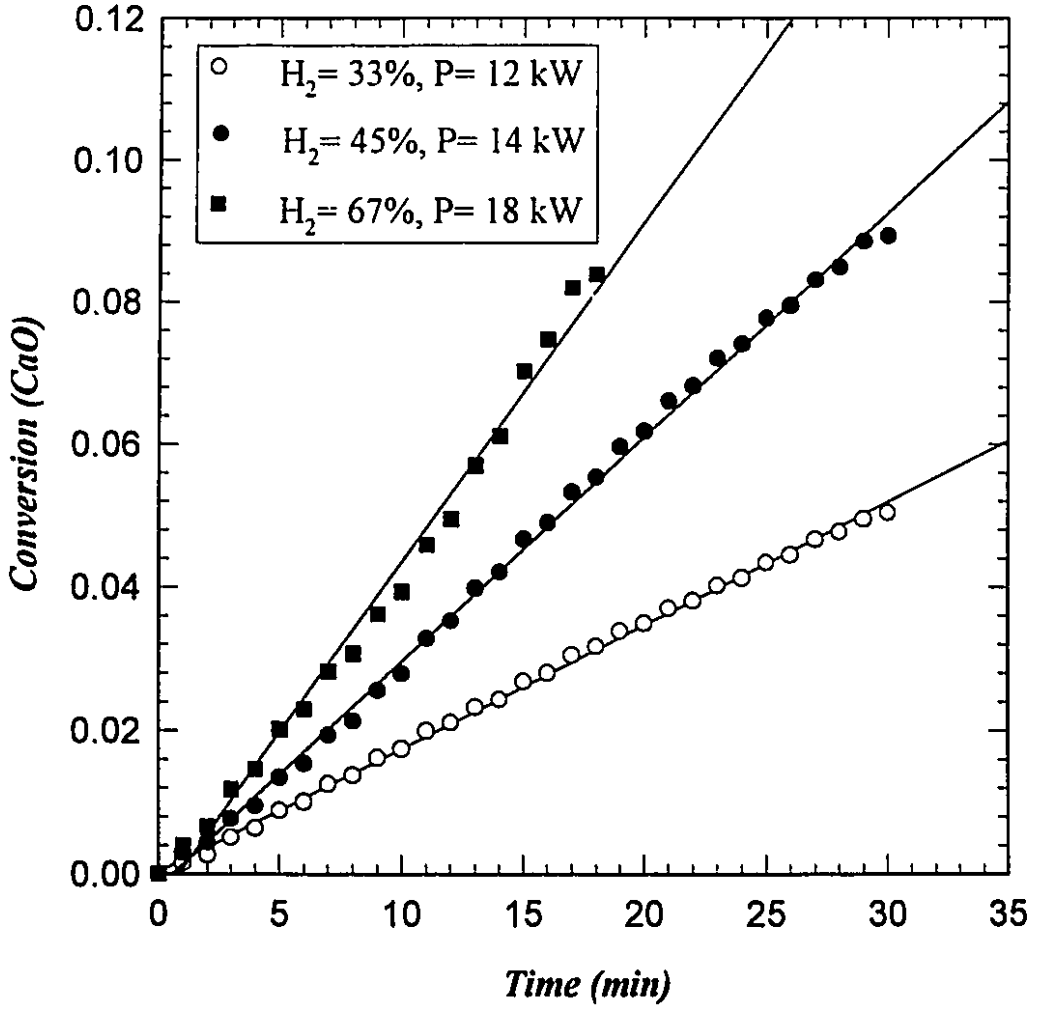

Figure 6.10: Conversion of calcium oxide to carbon monoxide for methane at different plasma powers. Methane was injected as a fluidizing gas a 10 L/min. Plasma gas flow rate is 40 L/min.

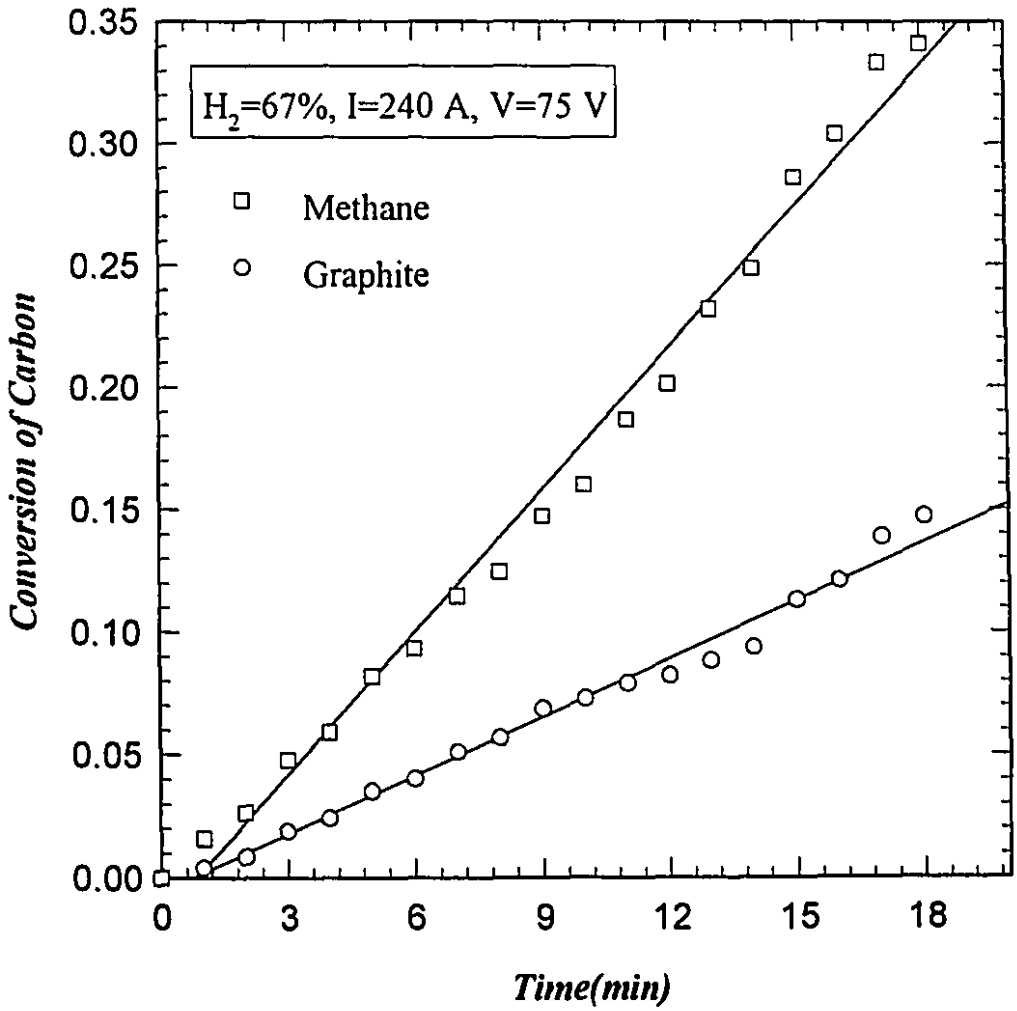

Figure 6.11: A comparison between the rates of carbon conversion to carbon monoxide for methane and graphite at a plasma power of 18 kW. Methane was injected as a fluidizing gas at 10 L/min and plasma gas flow rate was 40 L/min.

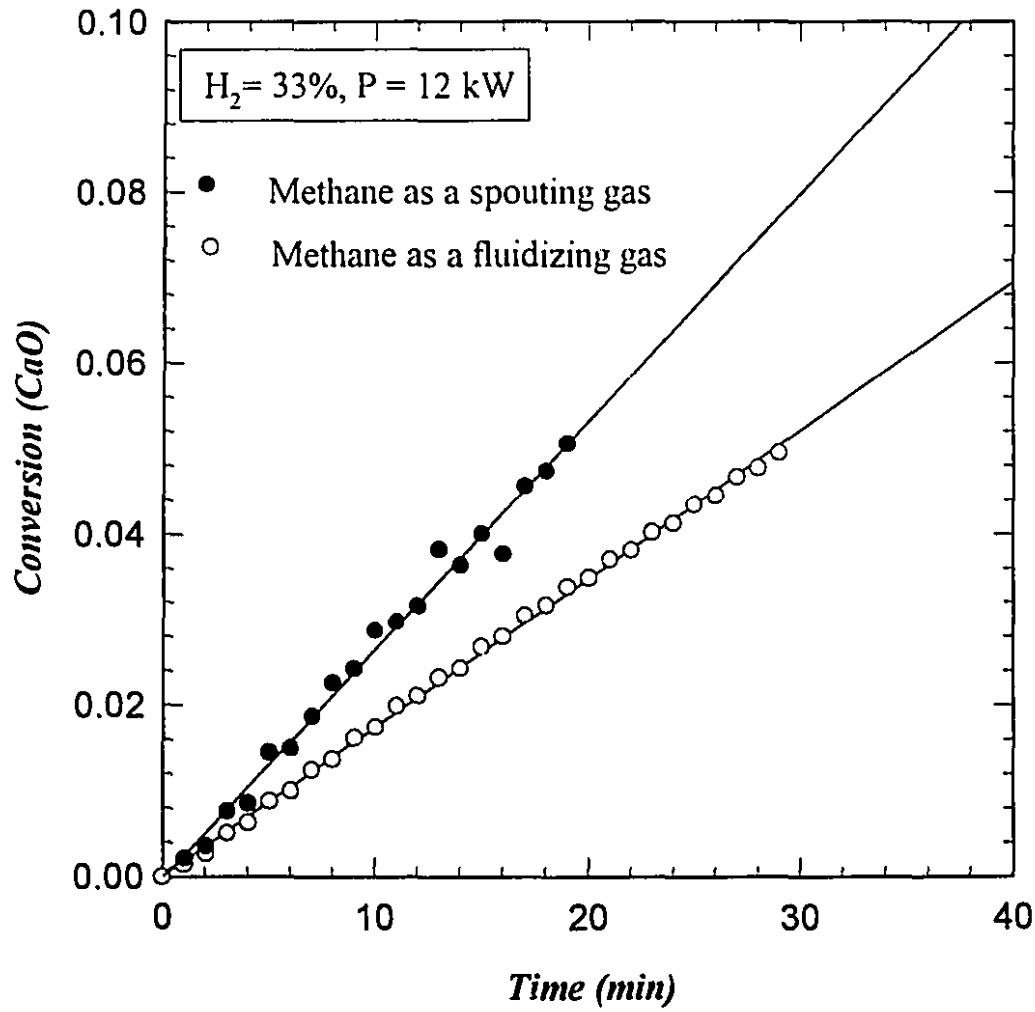

Figure 6.12: A comparison between the rates of calcium oxide conversion to carbon monoxide for fluidizing and spouting methane at a plasma power of 12 kW. Methane was injected at 10 L/min and plasma gas flow rate was 40 L/min.

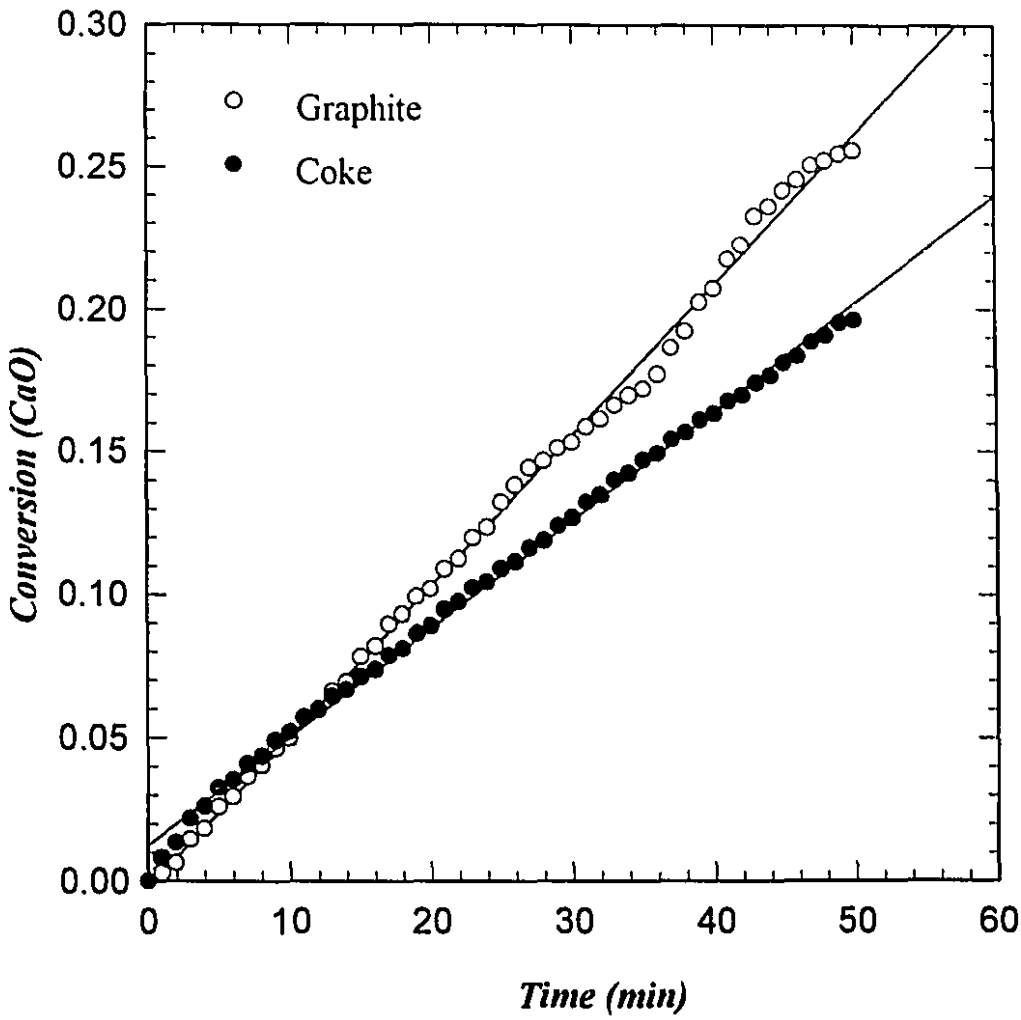

Figure 6.13: A comparison between conversions of calcium oxide to carbon monoxide for coke and graphite at a plasma power of 16 kW. Carbon to calcium oxide molar ratio was 3:1 and plasma gas flow rate was 40 L/min.

6.3.3 Graphite Reactivity

A second type of graphite with a mean particle size of 350 μm was also reacted with calcium oxide powder. This graphite will be referred to as graphite II (G-II), while graphite I (G-I) is the first graphite. Both types were reacted with calcium oxide in a molar ratio of 3 to 1 at two plasma powers of 12 and 16 kW, with argon at 10 L/min as the fluidizing gas. The conversions of calcium oxide for both types of graphite at both conditions are plotted against run time in Figure 6.14 and Figure 6.15. The rate of conversion for G-II was much higher than that of G-I for both conditions. This major difference in the rate of reaction between the two types of graphite can only be attributed to differences in structure or accessible surface area. X-ray diffraction and porosity analyses were carried out for both graphites. The aim of these analyses was to determine the relative porosity and any difference in crystal structure between the two types of graphite.

Samples of the two types of graphite were analyzed by X-ray diffraction to determine whether they have the same crystal structure. A comparison between the two diffraction diagrams is shown in Figure 6.16. The noticeable difference between the two diagrams is the pronounced presence of a peak at ($2\theta = 52$) for G-II, which is barely visible for G-I. The presence of this peak and the difference in intensity ratio between the other peaks may indicate that the two graphites have different crystal structures, with G-II being more crystalline than G-I. It is unlikely, however, that this difference could account for the different reaction rates.

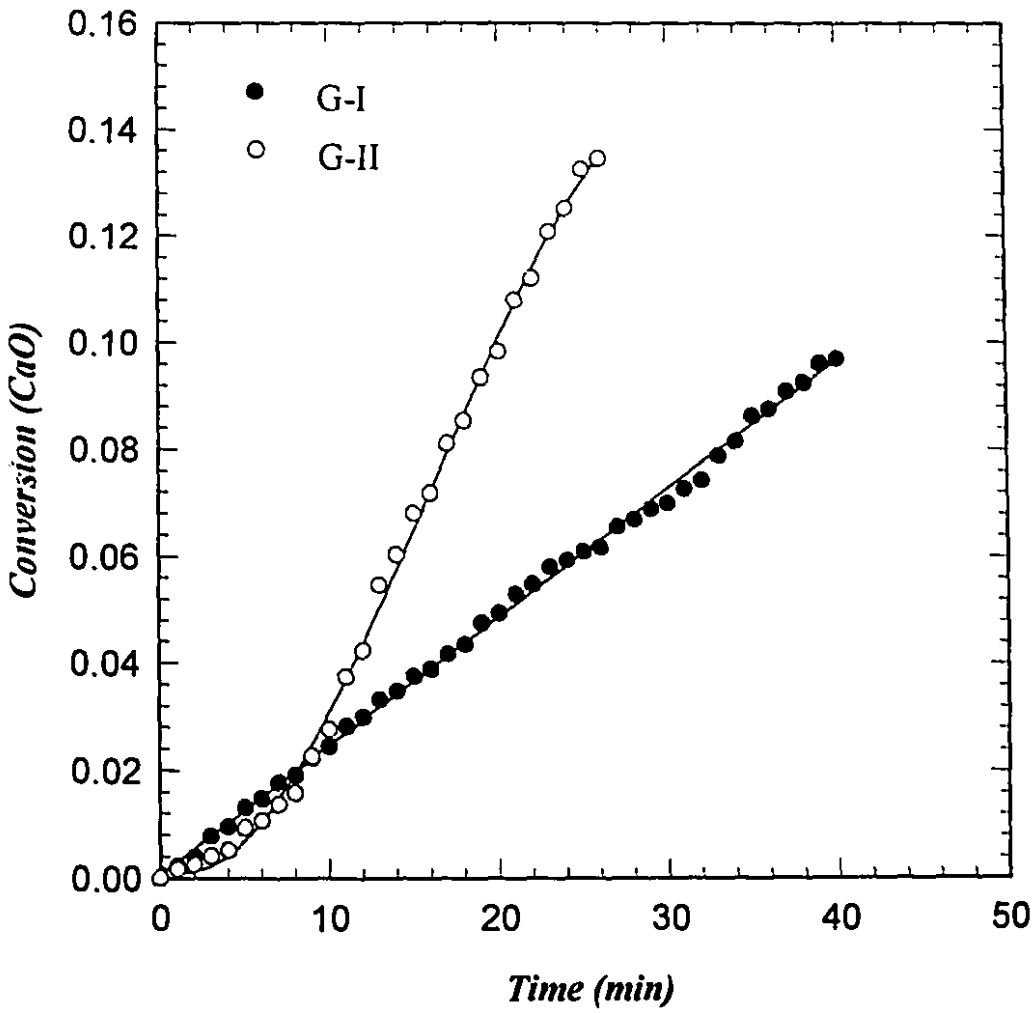

Figure 6.14: A comparison between conversions of calcium oxide to carbon monoxide for G-I and G-II at a plasma power of 12 kW. Carbon to calcium oxide molar ratio was 3:1 and plasma gas flow rate was 40 L/min.

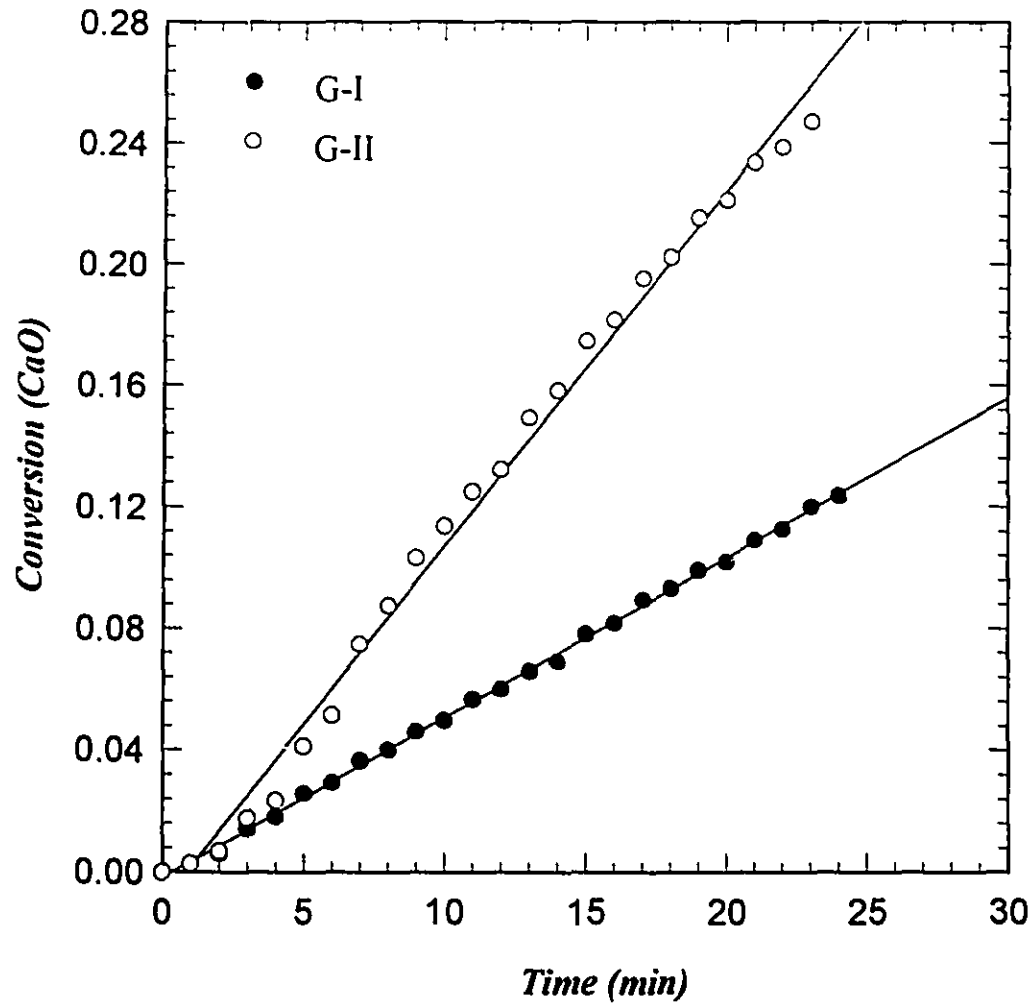

Figure 6.15: A comparison between conversions of calcium oxide to carbon monoxide for G-I and G-II at a plasma power of 16 kW. Plasma gas flow rate was 40 L/min.

Porosity analysis for the two types of graphite was carried out using mercury intrusion porosimetry. Values for the corrected mean porosity for both types are given in Table 6.2. Clearly, G-II is about four times as porous as G-I and, consequently has a larger surface area as shown in Figure 6.17. It is worth noting here that a higher porosity does not always mean a larger surface area; nevertheless, it is true when comparing particles with similar pore diameter as in this case. A larger surface area enhances the rate of carbon-calcium vapour surface reaction (Equation 5.12). Since this reaction is the rate controlling step, the overall rate of formation of calcium carbide is improved considerably. It is noticeable, however, that the rate of conversion of G-II is quite slow for the first few minutes, especially for the lower power of 12 kW. This may be caused by the slow ionization of this type of graphite. Although G-II may be superior with regards to adsorption of and reaction with calcium vapour, due to the larger surface area, it may not be superior with regards to ionization and diffusion into the oxide lattice.

Carbon reactivity, therefore, is an essential factor in determining the rate of formation of calcium carbide. Reaction between calcium oxide and carbon can be considered to proceed through two main stages: *initiation* and *gas-solid reaction*. The initiation step depends mainly on the ability of carbon to ionize and diffuse into the calcium oxide particles. It is this stage that starts the reaction by forming calcium vapour. Coke had the highest initial rate of reaction due to the presence of volatiles which facilitated the ionization of coke and diffusion into the oxide. The gas-solid reaction between carbon and calcium vapour depends on the ability of carbon to adsorb and react with calcium gas. Accessible surface area , therefore, was found to

be the main parameter in this stage. The second type of graphite (G-II) had the largest carbon surface area and therefore had the highest reaction rate. A summary of the reaction rates for the different forms of carbon is shown in Table 6.3.

Table 6.2- A Summary of Graphite Porosity Analysis.

Sample	*Mean Pore Diameter (μm)*	*Corrected Porosity(ε_c)*
Graphite I (G-I)	0.009	0.029
Graphite II (G-II)	0.010	0.118

Table 6.3 - Reaction Rates for the Different Sources of Carbon.

Carbon Source	*Reaction Rate (mol/min.)*	
	P= 12 kW	P = 16 kW
Graphite I	0.026	0.054
Graphite II	0.074	0.130
Coke	-	0.041
*Methane**	0.019	-
*Methane***	0.029	-

* Fluidizing methane, ** Spouting methane.

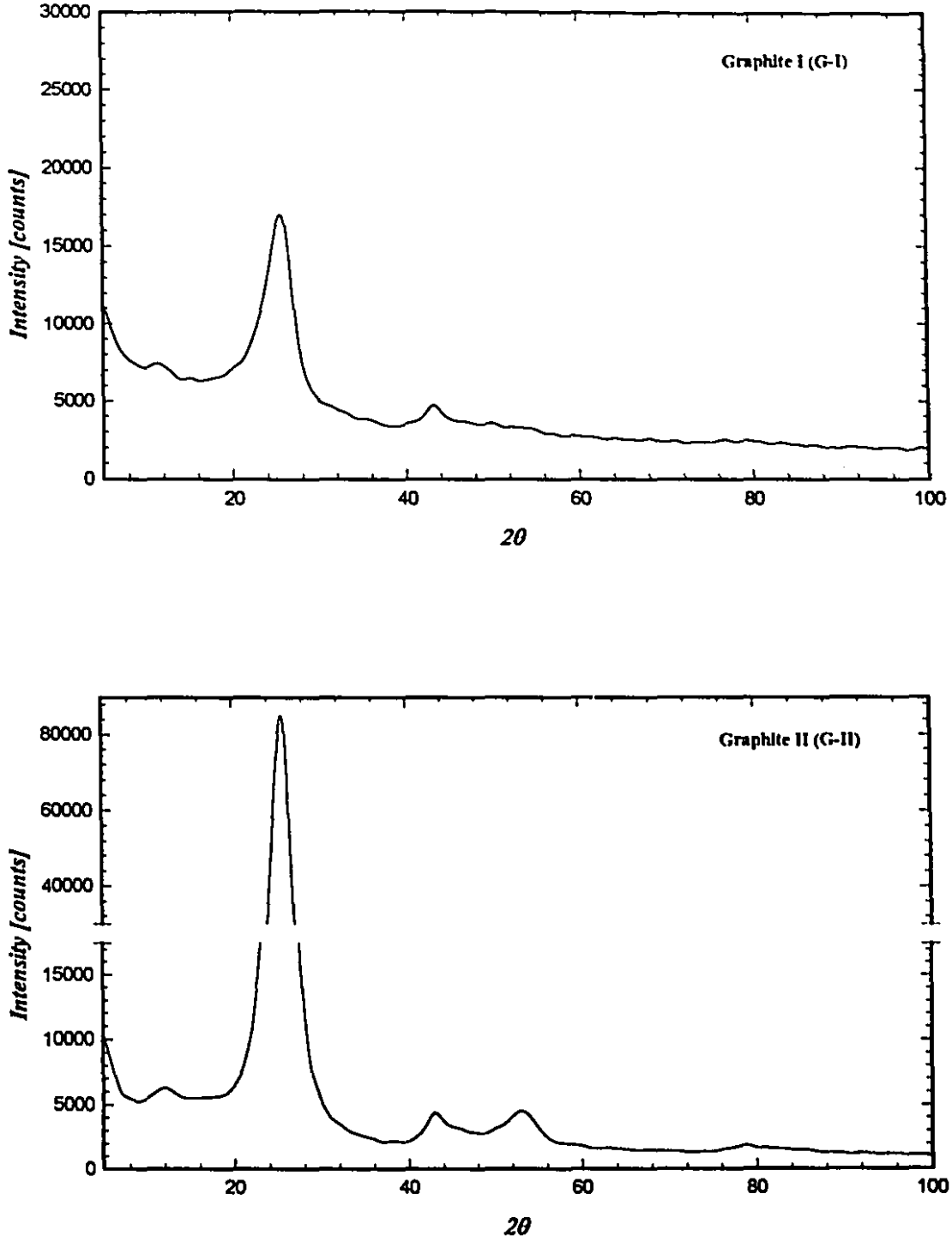

Figure 6.16: X-ray diffraction patterns for the two types of graphite (G-I and G-II).

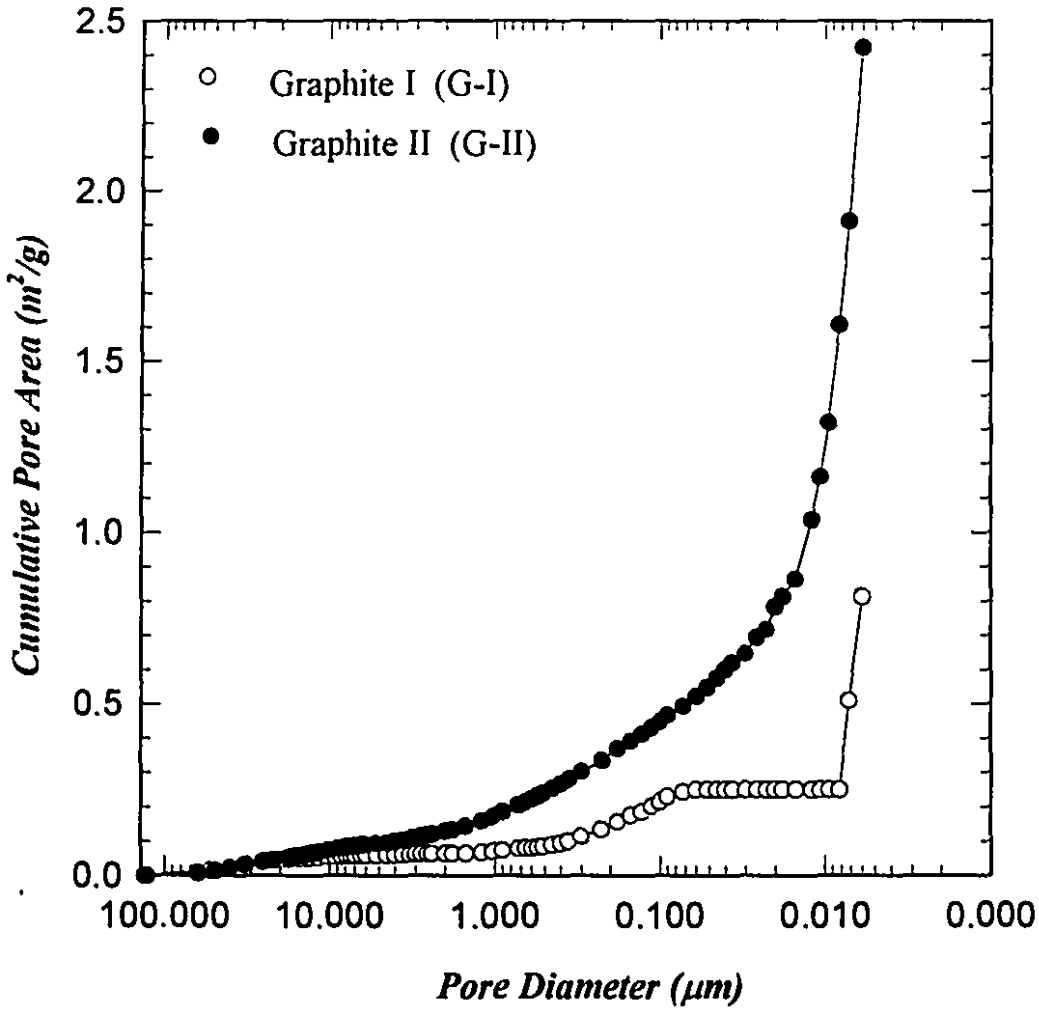

Figure 6.17: A comparison between cumulative pore areas for the two types of graphite (G-I and G-II).

CHAPTER SEVEN

"You can observe a lot just by watching"

Yogi Berra, New York Yankees

CHAPTER VII 7

THEORETICAL INTERPRETATION AND MODELLING

7.1 DESCRIPTION OF THE REACTION PROCESS

It was previously described (Chapter 3) that the plasma torch was positioned at the bottom of the fluid bed reactor. This arrangement created two different zones inside the reactor: a high temperature plasma jet zone and a well mixed, isothermal bed zone. During experiments, particles enter the jet at the mean bed temperature T_B. As they pass through the jet, their temperature increases to a maximum temperature T_I at the upper interface between the jet and the bed zone. At the same time, the gas temperature in the jet zone decreases sharply from T_J at the exit of the torch nozzle to T_I at the interface as shown in the diagrams below.

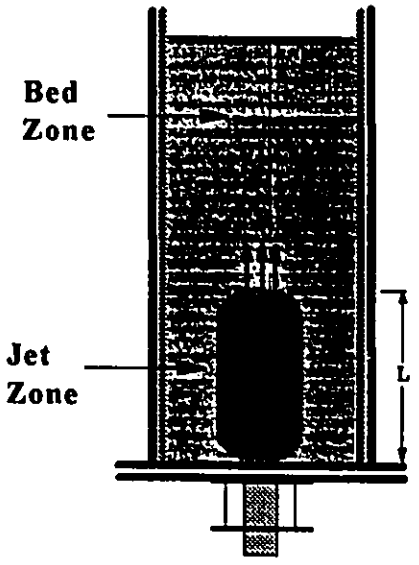

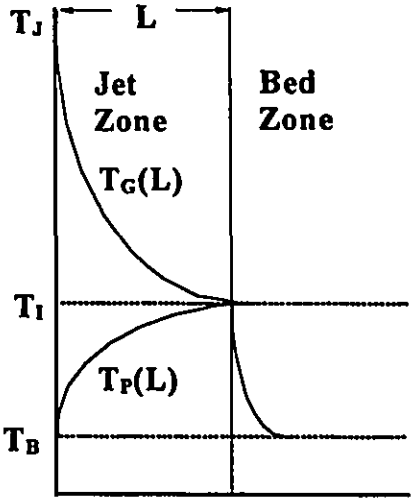

As the plasma gas and the particles in the jet impinge upon the dense bed zone, their temperature drops to the bed temperature T_B. The interface temperature T_I was measured experimentally at the highest hydrogen concentration (67%). Based on this measurement, the rate of particle circulation into the jet (M_P) was calculated by performing an energy balance over the volume of the jet, assuming that the gas and particle temperatures were equal at the interface. This assumption meant that the particle heating rate was so fast that the particle reached the gas temperature before leaving the jet zone.

7.2 VALIDITY OF THE ASSUMPTION

Measurement of the interface temperature at the highest hydrogen concentration (67%) was carried out using the Accufiber lightpipe sensor. It is expected that the measured temperature is closer to the gas temperature. However, the combination of high jet temperature, good heat transfer and small particle size may indicate that the particle temperature approaches that of the gas at the interface. This argument was the basis for assuming gas-particle temperature equality at the upper boundary of the jet zone. The validity of this assumption can be verified by comparing particle residence time within the jet with the time needed for the particles to reach T_I by transient heat transfer. Calculation of particle terminal velocity (v_t) indicated that it was small compared to the gas velocity (v_J) as shown in Table 7.1. This implied that particles inside the jet had the same velocity as the gas, and that their residence time was of the order of milliseconds as shown in Table 7.2.

Table 7.1 Particle terminal velocity, plasma jet velocity and properties at T_G.

H_2(vol%)	v_t (m/s)	v_j (m/s)	ρ_f(kg/m^3)	μ (kg/m.s)
0	0.11	38	5.78×10^{-2}	2.43×10^{-4}
33	0.10	42	2.62×10^{-2}	2.57×10^{-4}
45	0.11	44	1.93×10^{-2}	2.54×10^{-4}
67	0.12	46	1.0×10^{-2}	2.23×10^{-4}

Gas-particle heat transfer in the jet depended mostly on the plasma gas composition and plasma jet temperature. Transient heat transfer to the particle was calculated assuming a Nusselt number of 2. The lumped capacitance method was used to estimate the transient heat transfer to the particles. This method assumes that the temperature of the particle is spatially uniform at any instant during the transient heating, and hence temperature gradients within the particle are negligible. An important parameter in the lumped capacitance method is the Biot number (hL_C/k), where h is heat transfer coefficient, L_C is the characteristic length and k is the particle thermal conductivity. Values for k for graphite and calcium oxide were taken from Touloukian et al (1970). Since the thermal conductivity of graphite was much higher than that of calcium oxide, the calculations were based only on the oxide thermal conductivity. The Biot number represents a ratio between resistance to conduction within the particle to resistance to convection across the fluid boundary layer. Thus, for the lumped capacitance method to be valid , the Biot number must be much less than unity ($Bi \ll 1$). The error associated with the method is expected to be negligible for $Bi \leq 0.1$ (Incropera and Dewitt, 1985). Values for the Biot number for

the different conditions are given in Table 7.2. Particle heating time can be calculated by energy balance on the particle as follows:

$$hA_S(T_G - T) = \rho V C_{PP} \frac{dT}{dt} \qquad (7.1)$$

Let $\theta = T_G - T$, where $T_G = \frac{(T_J - T_I)}{\ln(\frac{T_J}{T_I})}$

Thus, $$\rho C_{PP} \frac{V}{hA_S} \frac{d\theta}{dt} = -\theta \qquad (7.2)$$

Integrating using the initial condition $\theta(0) = \theta_B$, with $\theta_B = T_G - T_B$ and taking into account that for a spherical particle $V/A_S = dp/6$ gives

$$t_h = \frac{\rho C_{PP} dp}{6h} . \ln \frac{\theta_B}{\theta} \quad \text{or} \quad t_h = \frac{\rho C_{PP} dp}{6h} . \ln \left[\frac{T_G - T_B}{T_G - T_I} \right] \qquad (7.3)$$

where, d_P is the particle diameter and ρ is the particle density.

Values for t_h are compared with residence time in Table 7.2. Clearly the heating time is much less than the particle residence time for conditions where hydrogen was added to the plasma gas. This confirms, for those conditions, the validity of the assumption that the particle temperature reaches that of the gas at the upper interface. For pure argon, however, the case is different. Heat transfer limitations seem to be important, and as a result the particle may not reach the gas temperature before leaving the jet zone.

Table7.2: A comparison between particle residence and heating time inside the jet.

H_2(vol%)	Re	h ($W/m^2.K$)	Bi	τ (s)	t_h (s)
0	3.96×10^{-3}	2.0×10^{3}	0.01	0.001	0.0040
33	1.60×10^{-3}	1.5×10^{4}	0.08	0.002	0.0010
45	1.21×10^{-3}	2.0×10^{4}	0.10	0.002	0.0008
67	8.13×10^{-4}	2.5×10^{4}	0.13	0.002	0.0007

Re= Reynolds number
h = Plasma gas heat transfer coefficient ($W/m^2.K$)
Bi= Biot number
τ = Particle residence time in the jet (s)
t_h = Time needed for particles to reach T_I in the jet (s).

7.3 CALCULATION OF THE REACTION TEMPERATURE

For other conditions, the particle temperature and the circulation rate are calculated based on the following assumptions:

- The particle and the gas temperature are equal at the plasma jet upper boundary (jet-bed interface, $T_P=T_G=T_I$)
- The size (volume) of the jet zone and the particle circulation rate are directly proportional to the plasma net power . The shape of the jet zone is assumed to be a paraboloid, with equal base and height. The volume is then equal to $(1/8)\pi L^3$.

The particle temperature at the interface, T_I, and the rate of particle circulation into the jet zone can be calculated by energy balance over the jet zone as follows:

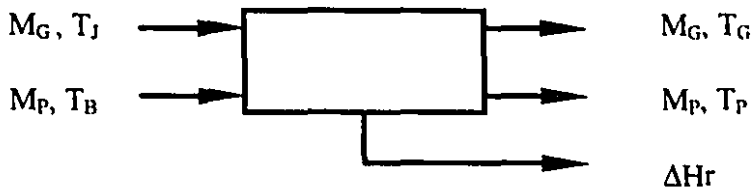

$$\int_{T_G}^{T_J} M_G C_P dT = M_P C_{PP}(T_P - T_B) + r\,\Delta H_r$$

With $T_P = T_G = T_I$,

$$M_P = \frac{\int_{T_I}^{T_J} M_G C_P dT - r\Delta H_r}{C_{PP}(T_I - T_B)} \qquad (7.4)$$

Also,

$$M_P = \beta H_J \qquad (7.5)$$

where,

L = Plasma jet height (m).
T_J = Plasma gas temperature as it leaves the torch (K).
T_G = Gas temperature in the jet zone (K).
T_B = Mean bed temperature (K).
T_P = Mean particle temperature (K).
T_I = Temperature at the jet-bed interface (K).
M_G = Plasma gas flow rate (kg/min).
M_P = Particle circulation rate (kg/min).
H_J = Plasma net power (kJ/min).
β = Proportionality constant (kg/kJ).
C_P = Heat capacity of plasma gas (kJ/kg.K)
C_{pp} = Heat capacity of particles (mean heat capacity of bed materials)
r = rate of reaction (mol/min).
ΔHr = heat of reaction (kJ/mol).

Heat capacities for the different plasma gas compositions were taken from Boulos et al. (1994) and fitted to the following equation:

$$C_P(T) = A + B*10^{-3}\,T + C*10^{5}\,T^{-2} + D*10^{-6}\,T^{2} \qquad (7.6)$$

Values for A, B, C, and D for the plasma gas compositions used in the study are given in Table 7.3. Two temperature ranges were used for an accurate fit: (1000 to 3700 K) and (3700 to 12000 K). A plot of the heat capacities versus temperature is shown in Figure 7.1. For pure argon, the heat capacity is constant (at 0.520 kJ/kg.K) up to 6000 K. Values for the constants in Equation (7.6) for temperatures higher than 6000 K, are given in Table 7.3 .

Table 7.3 Values for A, B, C and D for Equation (7.6). Heat capacity at constant pressure (kJ/kg.K).

	Range I (1000 to 3700 K)			**Range II (3700 to 12000 K)**			
H_2 (Vol%)	***33%***	***45%***	***67%***	***0%****	***33%***	***45%***	***67%***
A	3.20	13.2	31.3	41.1	6.34	0.490	-18.1
B	-2.99	-10.7	-25.3	-7.35	-2.37	-1.76	0.011
C	-1.88	-40.0	-102.3	-3639	605	1549	4730
D	0.955	2.59	5.96	0.375	0.198	0.195	0.202

* For pure argon (0%H_2), this temperature range is from 6000 to 12000 K.

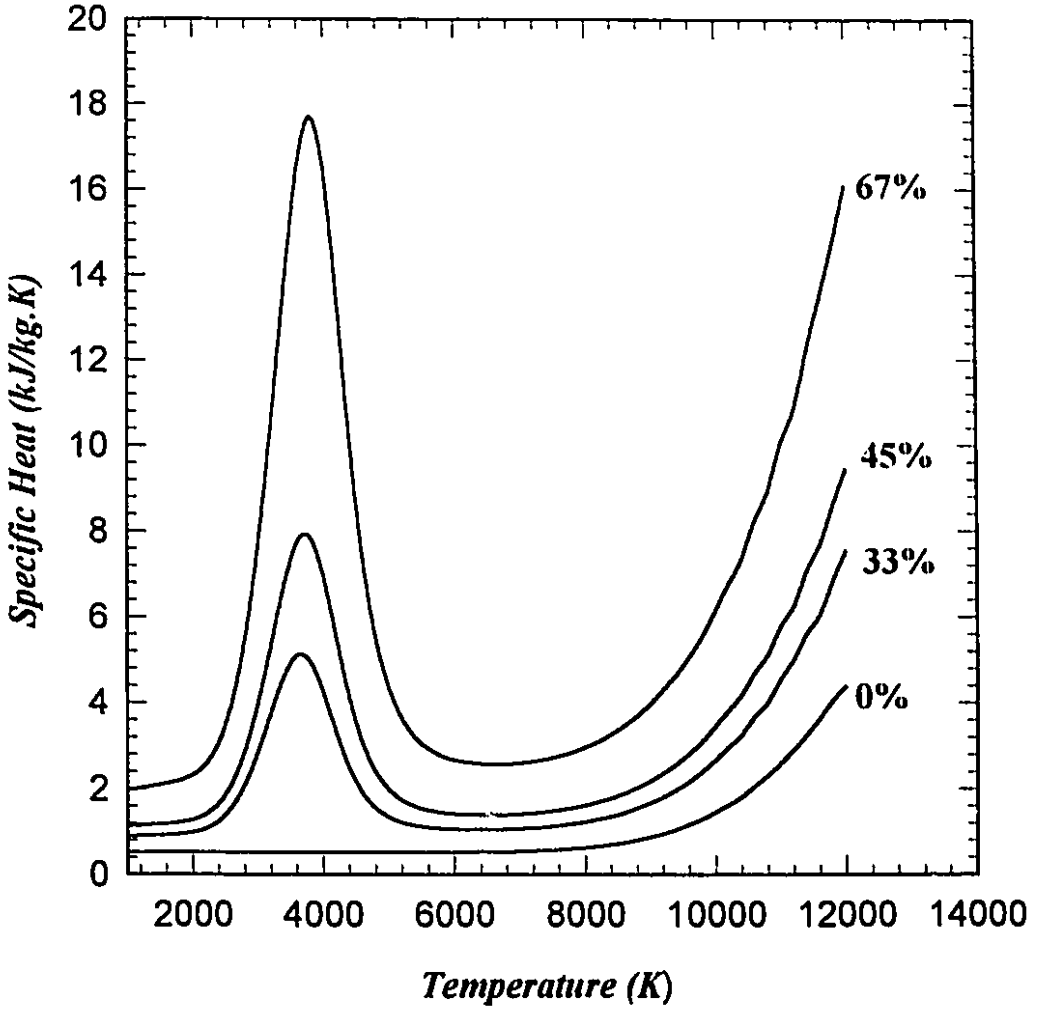

Figure 7.1: Heat capacity for the plasma gas versus plasma jet temperature at different compositions (H_2 vol.% in Ar). Based on data from Boulos et al. (1994).

Thermodynamic predictions (Chapter 4) indicate that the reaction to form calcium carbide does not proceed below 1600 K. Thus, particles passing through the jet do not react before reaching this temperature. The reaction temperature can then be estimated as the logarithmic mean between 1600 K and T_I. A logarithmic mean is more appropriate in this case than an arithmetic mean because of the nature of the increase in particle temperature inside the jet. The calculated particle temperature, particle circulation rate and the mean reaction temperature for the different conditions are listed in Table 7.4.

Table 7.4: Calculated mean reaction temperature for different conditions.

Power (kW) [%H_2]	*Calculated Mp (kg/min)*	*Calculated Particle Temperature (K)*	*Mean Reaction Temperature (K)*
5 [0]	0.168	1800	1700
12 [33]	0.402	1910	1750
14 [45]	0.470	1960	1774
18 [67]	0.604	2040	1811

7.4 HEAT TRANSFER LIMITATIONS

Heat transfer from the high temperature plasma gas to the solid particles is an essential factor in determining the reaction rate for endothermic gas-solid reactions. Although the transient heat transfer calculations discussed earlier indicated that the solid particles reached the gas temperature before leaving the jet, a comparison between convection heat transfer to the solid particles and the heat of reaction was needed to estimate any heat

transfer limitations to the rate of solid phase formation of calcium carbide. The calculation was carried out assuming a Nusselt number of 2 and neglecting radiation heat transfer. The rate of heat transfer to the solid particles, per pass through the jet, for the different plasma powers was calculated as follows:

$$Q = A_S h (T_G - T_R) \qquad (7.7)$$

where, A_S is particle surface area (m^2), h is the heat transfer coefficient ($W/m^2.K$), T_G and T_R are the mean plasma gas temperature and the mean reaction temperature (K) respectively. The use of the mean reaction temperature results in a rather conservative estimate of the heat transfer. The total energy transferred to the particles throughout the complete run is equal to the rate of heat transfer (Equation 7.7) times the estimated cumulative residence time in the jet zone. This total energy is compared with the energy used by the reaction as heat of reaction in Figure 7.2. For conditions, where hydrogen was present in the plasma gas, the total energy transferred to the particles was much higher than that used by the reaction. This clearly indicated that for those conditions there were no heat transfer limitations and that the reaction rate was the main controlling mechanism. For pure argon, there may be heat transfer limitations. However, these heat transfer calculations were based on a Nusselt number of 2, which gave very conservative values for the heat transfer coefficient. Given the good mixing and the high particle velocity, the actual value for the heat transfer coefficient is expected to be much higher and consequently, a much higher rate of heat transfer is expected even for the pure argon plasma.

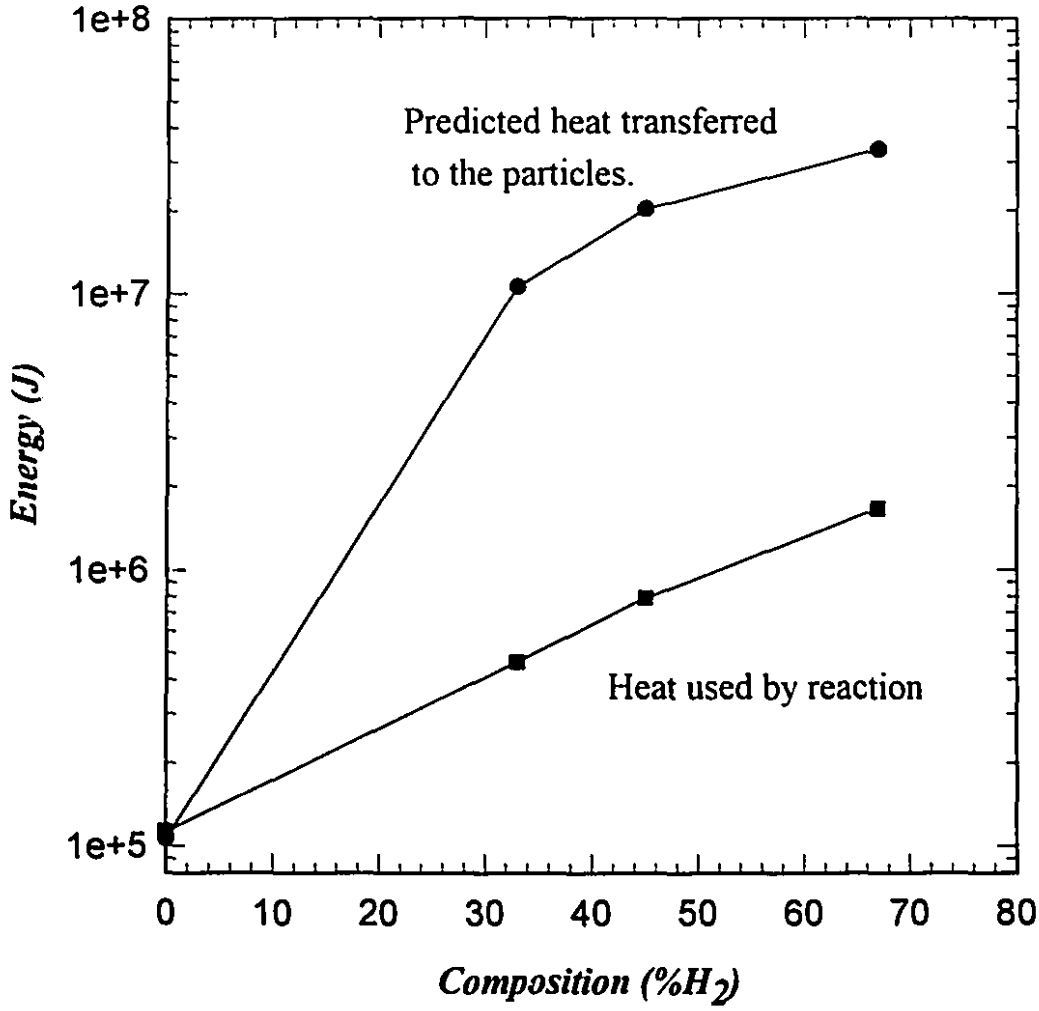

Figure 7.2 : A comparison between the total energy transferred to the particles and the energy used by the reaction.

7.5 REACTION MODELLING

Modelling of gas-solid reactions encompasses a vast area of study which has been discussed in detail by many authors (Wen, 1968; Sohn and Szekely, 1973; Tamhankar and Doraiswamy, 1979; and Doraiswamy and Sharma, 1984). Choosing an appropriate model should be based on quantitative results as well as qualitative observations of the reaction and the product morphology. Experimental results and microscopic analysis of the solid products indicate that the reaction under study in the present work may follow a chemical reaction control, shrinking core model.

One of the main assumptions of the shrinking core model is constant reaction temperature (isothermicity). Although the temperature profile in the reaction zone (plasma jet zone) was not expected to be constant, experimental results and analysis of the reaction process indicated that the reaction temperature was almost constant throughout the experimental run. The increase in the temperature of the particles as they pass through the jet was much more than the increase in the bed temperature throughout the run. Thus, the interface temperature (T_i) and hence the reaction temperature were almost constant.

For a shrinking core model with chemical reaction control, the fractional conversion is related to time as follows:

$$1-(1-X)^{1/3} = Kt \qquad (7.8)$$

where K is the apparent rate constant. For diffusion control, the relation between conversion and time can be written as (Wen, 1968):

$$[1-(1-X)^{1/3}]^2 = K't \qquad (7.9)$$

where K' is a different rate constant. Thus, the fractional conversion for both controlling mechanisms can be related to time as:

$$[1-(1-X)^{1/3}]^n = K''t \qquad (7.10)$$

This relation may be used to determine the controlling mechanism. A plot of ln[t] versus $\ln[1-(1-x)^{1/3}]$ yields a straight line with a slope which equals n. The slope (n) would be equal to one for reaction control and two for diffusion control. Experimental conversions plotted in this manner resulted in a slope of (1± 0.10) for all conditions, with the exception of pure argon, where n was about 1.25. A plot for ln[t] versus $\ln[1-(1-X)^{1/3}]$ for two plasma conditions is shown in Figure 7.3. This indicates that the global rate of conversion is controlled by chemical reaction rate and that Equation (7.8) can be used to estimate the global rate constant. A plot of $1-(1-X)^{1/3}$ versus run time is shown in Figure 7.4 for the reaction between calcium oxide and graphite I (G-I) for different plasma powers. The fit was excellent for all conditions where hydrogen was present in the plasma gas with R^2 greater than 0.99, indicating again that the rate of reaction for those conditions was controlled by chemical reaction rate. For pure argon, however, the fit was not as good, an indication, perhaps, of some heat transfer limitations. The slopes in Figure 7.4 represent the apparent global rate constants.

The conversion of calcium oxide to carbon monoxide was always calculated based on the total number of moles of CaO initially fed to the reactor. Calculations of particle circulation rate indicated that the amount of reactants entering the jet at any time and

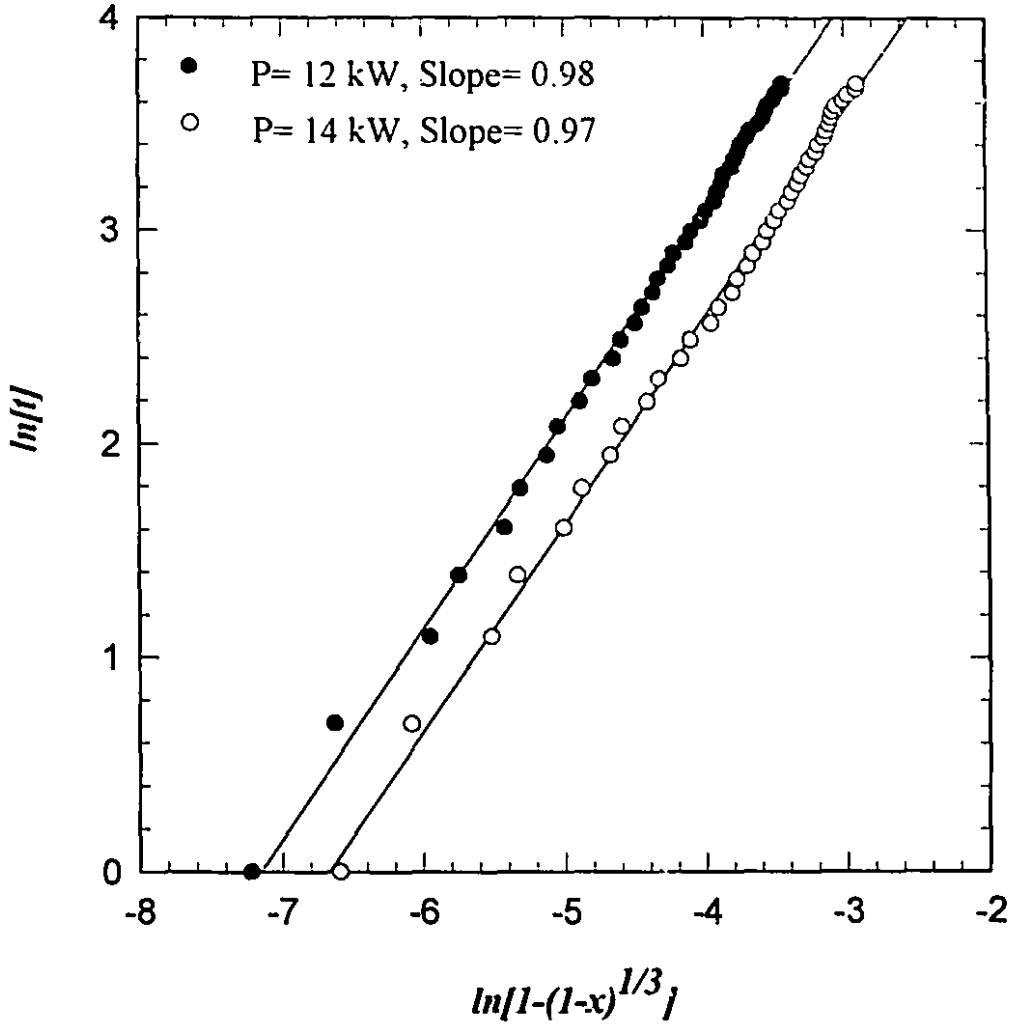

Figure 7.3: Ln[t] versus ln[1-(1-X)$^{1/3}$] for plasma powers of 12 and 14 kW.

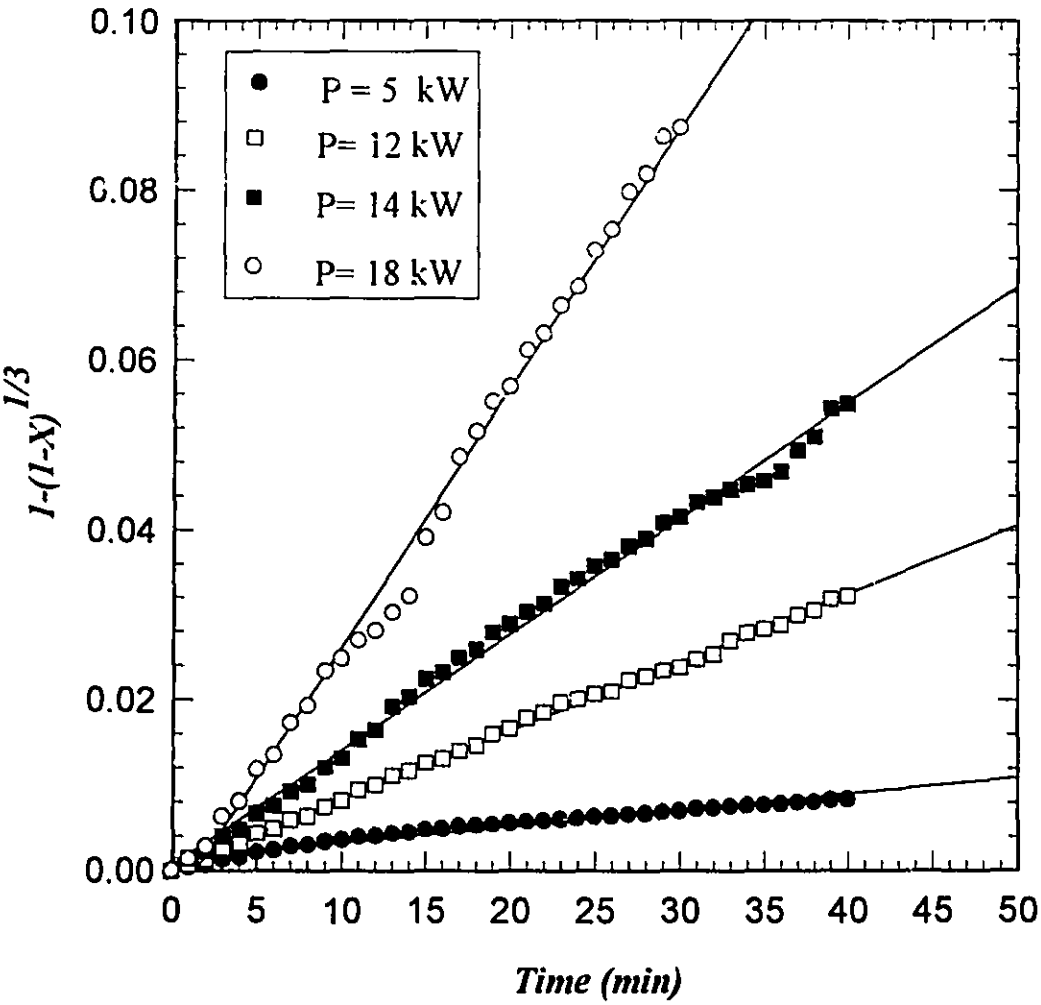

Figure 7.4: $1-(1-X)^{1/3}$ versus run time for different plasma powers.

therefore the surface area of carbon available for reaction was not the same for all conditions. Thus, the conversion is recalculated based on the particle circulation rate, Mp instead of the total bed. These adjustments resulted in new values for the global rate constants for the different conditions. A plot of the logarithm of the new rate constants against the reciprocal of the reaction temperature is shown in Figure 7.5. The apparent activation energy was calculated from the slope and found to be 90 kcal/mol. Uncertainty in this value came from errors in calculating the particle temperature and the circulation rate and was estimated to be about 10%. This high activation energy confirmed that the global rate of reaction was controlled by chemical reaction.

7.6 ESTIMATION OF TIME FOR COMPLETE CONVERSION

Reaching complete conversion is usually one of the main aims of studying any chemical reaction. Although the highest conversion achieved in the present work was of the order of 30%, experimental results and theoretical analysis indicated that higher conversions can be achieved with optimized reactor design. The positioning of the plasma torch at the lower part of the reactor created a high temperature zone at the bottom, where partially reacted particles melted and agglomerated, resulting in destabilization of the bed and impeding the reaction progress.

The reaction rate determined in the study and the reaction modelling may be applied to estimate the time needed for complete conversion. A few assumptions, however, are needed. It is assumed in this calculation that the reaction model applies to complete conversion and that the reaction rate is constant even at high conversions. This

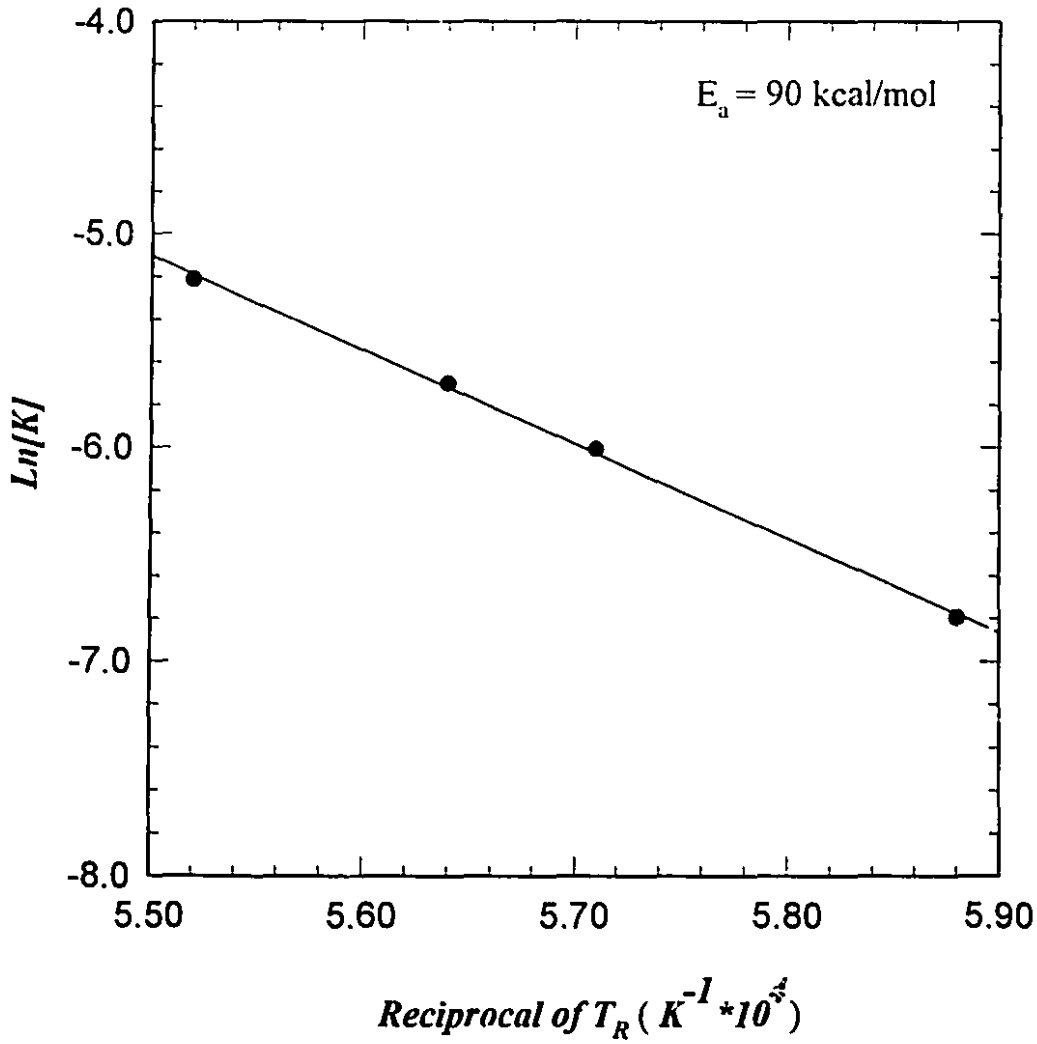

Figure 7.5: Logarithm of the global rate constants versus the reciprocal of the calculated reaction temperatures.

assumption, however, is difficult to validate, and it is only an extrapolation of the low conversion results. The aim of the calculation is to estimate the residence time needed to reach complete conversion in the plasma fluid bed reactor. The residence time of particles in the jet zone may be defined as follows:

$$\tau = \frac{(1-\varepsilon_J)V_J}{(1-\varepsilon_B)V_B}\, t \qquad (7.11)$$

where ε_J and ε_B are voidages in the jet and the bed zone respectively. V_J and V_B are volumes of the jet and the bed zone, and t is the run time. $(1-\varepsilon_J)$ represents the solids concentration in the jet zone and it is expected to be lower than that in the bed zone. For the sake of simplicity, however, the solid concentrations are assumed to be the same in both zones. The jet volume may be estimated for the different conditions assuming the jet to be a paraboloid in shape and that the volume is proportional to the plasma jet enthalpy as was discussed earlier. Values for $\frac{V_J}{V_B}$ for different conditions are shown in Table 7.5.

Table 7.5: Ratio of jet volume to bed volume for different conditions.

Power (kW) [%H_2]	*Calculated Mp (kg/min)*	*Mean Reaction Temperature (K)*	*V_J/V_B*
5 [0]	0.168	1700	0.032
12 [33]	0.402	1750	0.076
14 [45]	0.470	1774	0.089
18 [67]	0.604	1811	0.114

Substituting for t from Equation (7.11) into Equation (7.8), assuming $\varepsilon_J = \varepsilon_B$ and solving for the fractional conversion gives:

$$X = 1 - [1 - K(V_B/V_J).\tau]^3 \qquad (7.12)$$

where τ in Equation (7.12) represents the real reaction time, and for complete conversion τ is equal to $V_J/(K.V_B)$. A plot of conversion versus actual reaction time for different conditions for G-I is shown in Figure 7.6. For the highest plasma power of 18 kW (T_R = 1810), the estimated time for complete conversion is about 32 minutes. A lower time can be achieved, even at a lower temperature, for the more reactive form of graphite (G-II) as shown in Figure 7.7. It is important to note at this point that the time for complete conversion is overestimated in this calculation due to the assumption of equal solid concentrations in both the bed and the jet zone. A much lower time, therefore, can be expected. Although these calculations are based on extrapolation of experimental results and the reaction model, they indicate that complete conversion can be achieved within a reasonable time in the plasma fluid bed reactor to make it not only technically viable but also a competitive process for the solid phase formation of calcium carbide.

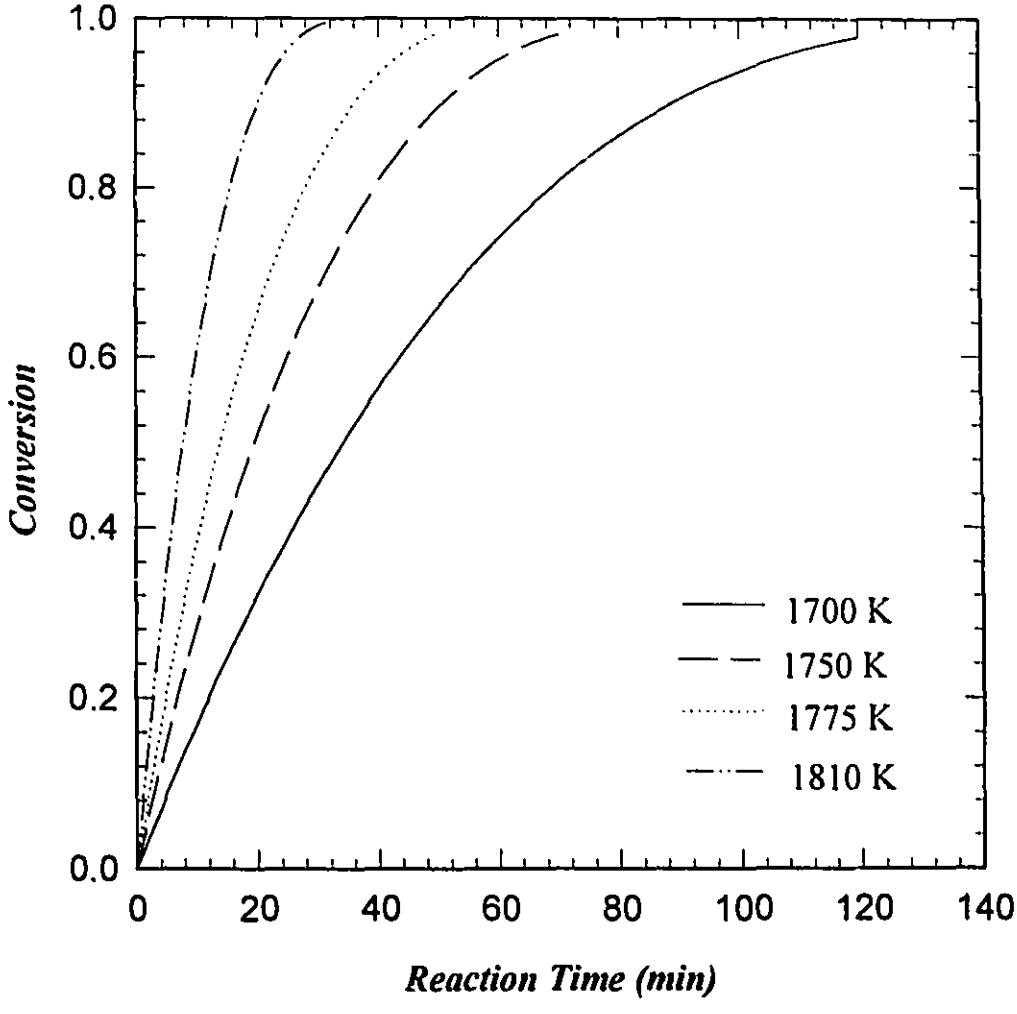

Figure 7.6: Predicted time for complete conversion at different conditions for reaction of calcium oxide with graphite I (G-I).

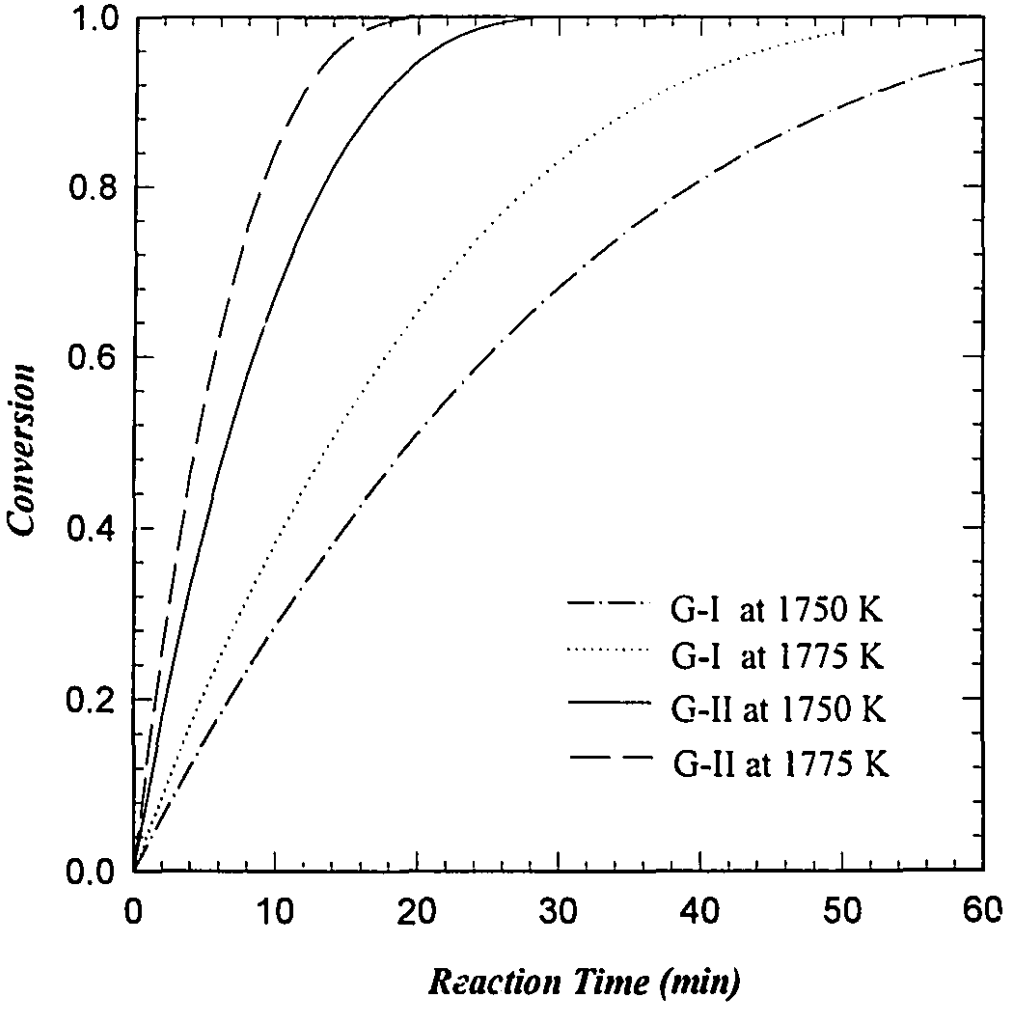

Figure 7.7: A comparison between predicted time for complete conversion for graphite I (G-I) and graphite II (G-II) at plasma powers of 12 and 14 kW (T_R= 1750 K and 1775 K).

CHAPTER EIGHT

"This is not the end.
It is not even the beginning of the end.
But it is the end of the beginning"

Winston Churchill (1874-1965)

CHAPTER VIII 8

CONCLUSIONS AND RECOMMENDATIONS

8.1 CONCLUSIONS

A new plasma spout fluid bed process for the production of calcium carbide has been studied as a replacement for the present electric arc furnace. A thermodynamic analysis of the reaction of calcium oxide and carbon was carried out using FACT. The analysis clearly confirmed the thermodynamic feasibility of the solid phase formation of calcium carbide and showed that the reaction would not proceed below 1600 K and would be complete at 2150 K. Calculation of the theoretical energy requirements for the plasma process indicated that the process could lower the energy requirements for the production of calcium carbide by up to 40%.

A semi-batch, laboratory-scale fluid bed reactor with a DC plasma torch, located at the bottom of the bed, was used for the study. Calcium oxide powder with a mean particle size of 170 μm was reacted with four forms of carbon: two types of graphite powder, coke powder and methane. Argon was used to initiate the plasma and fluidize the bed at just above the minimum fluidization velocity. The power achieved with argon plasma, however, was too low (5 kW) to obtain good conversion. Hydrogen was than added to increase power and raise the plasma enthalpy. The global rate of reaction was continuously monitored by carbon monoxide analysis of the exhaust gas. Samples of the solid products were analyzed to compute conversion and to examine product morphology.

The fluid bed reactor was found to have two different zones: a high temperature plasma jet zone and a well mixed isothermal bed zone. Experimental results showed that the reaction took place mainly in the jet zone and that conversion to calcium carbide increased linearly with reaction time. Carbon reactivity was found to be an essential factor in determining the rate of formation of calcium carbide. Reaction between calcium oxide and carbon can be considered to proceed through two main stages: *initiation* and *gas-solid reaction*. The initiation step depended mainly on the ability of carbon to ionize, diffuse into the calcium oxide particles and form calcium vapour. Coke had the highest initial rate of reaction due to the presence of volatiles which facilitated the ionization and diffusion into the oxide. The gas-solid reaction between carbon and calcium vapour depended on the ability of carbon to react with calcium and, therefore, the accessible carbon surface area was found to be the main parameter in this stage. The graphite that had the largest carbon surface area had the highest reaction rate.

Methane was reacted with calcium oxide by injecting it into the distributor as a fluidizing gas or directly into the plasma jet as a spouting gas. Direct injection of methane into the high temperature jet resulted in a higher rate of conversion. The large carbon surface area resulting from the decomposed methane (soot), makes methane more reactive than graphite. However, the difficulty with methane was its adverse effect on plasma jet temperature by physically quenching the jet and by endothermic decomposition. For this reason, methane had a minimum threshold power for the formation of calcium carbide. No carbide was formed by reacting calcium oxide and methane at less than 12 kW.

The rate of conversion to carbon monoxide was constant with time for all conditions and increased exponentially with increasing plasma jet temperature, indicating that chemical reaction was the controlling mechanism. The reaction rate was correlated to the shrinking core, reaction control model $1-(1-X)^{1/3} = Kt$, and agreement with the model was found to be excellent for conditions where hydrogen was present in the plasma gas and heat transfer limitations were negligible. The apparent activation energy of the reaction was determined to be 377 kJ/mol (90 ± 10 kcal/mol), confirming that the overall rate of formation of calcium carbide was controlled by chemical reaction. Microscopic analysis of the solid product showed that calcium carbide was formed around both reactants, indicating that the carbon-calcium vapour reaction took place at the surface of both free carbon and the carbon diffused into the oxide.

Limitations with the experimental apparatus made it difficult to achieve conversions beyond 30% in the present study. Although positioning the torch at the bottom of the reactor provided an efficient energy transfer to the reactants, it created a high temperature zone where melting of partially reacted particles occurred, before the bed reached the temperature needed for reaction. This resulted in instability of the bed and impeded the reaction progress. Higher conversions, however, can be achieved in a continuous process with optimized reactor design. Extrapolation of the reaction model and the low conversion results indicate that complete conversion can be achieved within a reasonable time in a plasma fluid bed process to make it a viable and a more efficient alternative process for the formation of calcium carbide.

8.2 RECOMMENDATIONS FOR FUTURE WORK

Although limitations with the apparatus made it rather difficult to achieve conversions higher than 30%, the experimental results obtained in the present work were promising and indicated that higher conversions could be reached even with the present apparatus with some modifications. Thus, the following improvements to the fluid bed reactor are recommended for future work:

- First, to avoid melting of particles and bed instability, the positioning of the plasma torch should be changed. The reactor should have two diametrically opposed plasma torches positioned near the bottom of the fluid bed just above the gas distributor pointing up at an angle of about 30°. This arrangement would eliminate the hot zone above the distributor where partially reacted particles would fall by gravity and melt. Also, having two diametrically opposed torches would provide more plasma power and hence more gas enthalpy. This also would avoid the disturbance of the symmetry of the bed by the plasma jet. The plasma torches should also have auxiliary gas ports that would provide a means for quenching the jet and for injecting methane.
- Second, elutriation of fine particles could make it difficult to use reactants with a small particle size. Thus, elutriation should be minimized by using an internal cyclone.

Experimentation can then be carried out to study the reaction at high bed temperatures and for longer runs. Also, attempts should be made to investigate the effect of using different sources of calcium oxide including the possibility of using calcium carbonate. Attempts should be made to estimate the reactor efficiency and the energy requirements for the reaction.

8.3 CONTRIBUTIONS TO KNOWLEDGE

Calcium oxide in the form of high calcium quick lime was reacted with solid and gaseous forms of carbon to investigate the feasibly of the solid phase synthesis of calcium carbide in a plasma reactor. Based on the experimental results and theoretical analysis of the reaction process, the following contributions to knowledge are claimed:

1. Calcium carbide was produced by reacting calcium oxide powder with four different sources of carbon in a plasma fluid bed reactor.

2. The mechanism of the reaction of calcium oxide and carbon as well as the product morphology were investigated. It was shown that calcium carbide was formed at the surface of both reactants.

3. The reaction rate was measured for different plasma conditions and correlated to a shrinking core, reaction control model. Also, it was demonstrated that the overall rate of formation of calcium carbide was controlled by chemical reaction.

4. The sintering of the calcium oxide particles at high temperature was found to lower the rate of formation of calcium carbide.

5. The surface area and the reactivity of the carbon were found to be essential factors in determining the rate of formation of calcium carbide.

REFERENCES

Ajersch, F. , "Chemical and Physical Characteristics Affecting the Reduction Kinetics of Iron oxide Pellets with Solid Carbon", Canadian Metallurgical Quarterly, Vol. 26, No., 2 (1987) PP. 137-144.

Azbe, V. J., " Science and Engineering in Lime-Burning" Industrial and Engineering Chemistry, Vol. 19, No. 5, 1927.

Baba, K. and Shohata N., "Manufacture of Calcium Carbide Micropowders by High-Frequency Plasma Method", Japanese patent 63112409, (1988).

Baldwin, B. G., "The Mechanism of the Reduction of Iron Oxide by Solid Coke" J. Iron Steel Inst., Vol. 179, (1955) PP. 30-36.

Bale, C. W., Pelton A. D. and Thompson, W. T., "Facility for Analysis of Chemical Thermodynamics, User's Guide", 1st edition, McGill University and Ecole Polytechnique (1979).

Biceroglu O., "Chlorination Kinetics of ZrO_2 in an R. F. Plasma Tailflame", Ph.D. Thesis, McGill University, 1978.

Bin, A. K., "Comments on the Minimum Fluidization Velocity of Coal-Derived Chars at Elevated Temperatures", Chem. Eng. Sci., Vol. 40, 1985.

Bin, A. K., "Minimum Fluidization Velocity at Elevated Temperatures and Pressures", Canadian Journal of Chemical Engineering Vol. 64, 1986, PP. 854-857.

Bodensein, M. , " The Mechanism of the Metallurgical Production of Zinc", Trans. Am. Electrochem. Soc, Vol. 51, 1927, PP.365-376.

Boulos, M. I., P. Fauchais and E. Pfender, *Thermal Plasmas: Fundamentals and Applications.* Volume I, Plenum Press, New York, 1994.

Boynton, R. S., *Chemistry and Technology of Lime and Limestone*, John Wiley & Sons, New York, 1980.

Brookes, C., Gall C. E. and Hudgins R. R., "A Model for the Formation of Calcium Carbide in Solid Pellets", Canadian Journal of Chemical Engineering, Vol. 53, (1975), pp 527-535.

Chin, E. J., "Carbothermic Reduction of Pyrochlore and Niobium Pentoxide in a Transferred Arc Plasma", Ph.D. Thesis, McGill University, 1989.

Doraiswamy, L. K. and M. M. Sharma, *Heterogeneous Reactions: Analysis, Examples and Reactor Design. Volume I: Gas-Solid and Solid-Solid Reactions*, John Wilcy and Sons, New York, 1984.

Eades, J. L. and P. A. Sandberg, "Scanning Electron Microscope Study of Development and Distribution of Pore Space in Calcium Oxide", Proceeding of the 2nd. annual S.E.M. Symposium, April 1969, Chicago, IL. PP.381-388.

EL-Naas, M. H., "Continuous Pyrolysis of CANMET Coprocessing Residue in Argon/Hydrogen Plasmas", M. Eng. Thesis, McGill University, 1991.

EL-Naas, M. H., R. J. Munz and F. Ajersch, "Production of Calcium Carbide in a Plasma-Jet Fluid Bed Reactor", ISPC-12, August (1995), Minneapolis, Minnesota, USA.

Eriksson, S., "Calcium carbide from powdered limestone or lime", Belgian patent 897179, (1983).

Fauchais P., M. Boulos and **E. Pfender,** "Physical and Thermodynamic Properties of Thermal Plasma", Chapter 3 in *Plasma Technology in Metallurgical Processing*, Ed. by Feinman J., Iron and Steel Society, Inc., 1987.

Flamant, G., "Hydrodynamics and Heat Transfer in a Plasma Spouted Bed Reactor", Plasma Chemistry and Plasma Processing, Vol. 10, (1990), PP. 71-85.

Flamant, G., " Plasma Fluidized and Spouted Bed Reactors: An Overview", ISPC-11, Loughborough, U.K., August, 1993.

Geldart, D, "Types of Gas Fluidization", Powder Technology, 7 (1973), PP 285-292.

Goldberger, W. M. and Oxley J. H., "Quenching the Plasma Reaction by Means of the Fluidized Bed", A.I.Ch.E. Journal, Vol. 9, (1963), PP. 778-782.

Grace, J. R., "Fluidized Bed Hydrodynamics", in *Handbook of Multiphase Systems*, G. Hetsroni, Ed., Hemisphere, Washington, DC, 1982, PP. 8-5 to 8-64.

Harrison, T. R., *Radiation Pyrometry and its Underlying Principles of Radiant Heat Transfer*, John Wiley & Sons, New York, 1960.

Hedin, R. , "Investigation of the Lime Burning Process", Swed. Cem. Conc. Res. Inst. Bull, Vol. 32, 1960.

Hellmold, P. and W. Gordziel, " Investigation of the Particular Reactions of CaC_2. 2- Investigation of the Formation of CaC_2 from Calcium Oxide and Carbon", Chem. Techn, Vol. 35, 1983, PP. 297-300.

Huber, E. F. and C. E. Holly, Journal of Physical Chemistry, 1967, PP. 408-409. [Cited in Müller, 1990a].

Incropera, F. P. and D. P. Dewitt, *Fundamentals of Heat and Mass Transfer*, 2nd Ed. John Wiley & Sons, New York, 1985.

Johnston, J. , "The Thermal Dissociation of Calcium Carbonate", J. Am. Chem. Soc., Vol. 32, 1910, PP. 938-946.

Jurewicz, J., Proulx P. and Boulos M. I., "The Plasma Spouted Bed Reactor", ISPC-7, Eindhoven, July (1985).

Kameyama, N., "Electrochemistry: Theory and Application", vol. III-2, Tokyo (1956), P. 134 [Cited in Tagawa and Sugawara, 1962].

Kampmann, F-W., Portz W., Frorath F-K., Hoechst A., Knapsack W. and Koln K., "Calcium Carbide", *Ullmann's Encyclopedia of Industrial Chemistry*, 5th Ed., VCH Verlagsgesellschaft, Weinheim (FRG), (1985).

Kim, C. S., R. Baddour, J. Howard and H. Meissner, "CaC_2 Production from Coal or Hydrocarbons in a Rotating-Arc Reactor", Ind. Eng. Chem. Process Des. Dev. Vol. 18, No. 2, 1979.

Kubaschewski, D., C. B. Alcock and P. J. Spencer, *Materials Thermochemistry*, 6th Ed., Pergamon Press, Oxford, 1993.

Kunii, D and O. Levenspiel, *Fluidization Engineering*, John Wiley & Sons, New York, 1969.

Lindblom, M., L. A. Andersson and I. Bjerle, "Water Determination in Pyrolysis Gases Using Calcium Carbide" Chem. Eng. Tech., Vol. 15, No. 2, 1992, PP. 99-102.

Labort M., Talandier F. and **Moneuse M.,** "Application des Torches á Plasma dans L'industrie", Rev. Gen. Elect., Vol. 90, No. 12, 1981, PP. 916 - 925.

March, H. and K. Kou, "Kinetics and Catalysis of Carbon Gasification", in *Introduction to Carbon Science*, H. Marsh, Ed., Butterworths, London, England, 1989, PP. 107-151.

Mayer, R. and R. Stowe, "Physical Characterization of Limestone and Lime" National Lime Association, 1964.

McEnaney, B. and T. J. Mays, " Porosity in Carbons and Graphites" in *Introduction to Carbon Science*, H. Marsh, Ed., Butterworths, London, 1989, PP. 153-196.

McTaggart, "Plasma Chemistry in Electrical Discharges", Elserier Publishing Company, Amsterdam, 1967.

Mehmetoglu T., "Characteristics of a Transferred-arc Plasma", Ph.D. Thesis, McGill University, 1980.

Mii, T, K. Yoshida and D J. Kunii, "Temperature Effects on the Characteristics of Fluidized Beds", J. Chem. Eng. of Japan, Vol. 6, No. 1 (1973), PP 100-102.

Mitchell, J., J. Am. Chem. Soc., Vol. 45, 1055, 1923. [Cited in Boynton, 1980].

Mu, J. J. and Hard R. A., "A Rotary Kiln Process for Making Calcium Carbide", Ind. Eng. Chem. Res., Vol. 26, (1987), PP. 2063-2069.

Mukaibo, T. and Y. Yamanka, J. Chem. Soc. Japan, Ind. Chem. Sec., Vol. 58, 1955. [Cited in Tagawa & Sugawara, 1962]

Müller, M. B., "Structure, Properties and Reactions of CaO In Burnt Lime, Part I: Design of a New Model of Burnt Lime ", Scandinavian Journal of Metallurgy, Vol. 19, 1990a, PP 64-70.

Müller, M. B., "Structure, Properties and Reactions of CaO In Burnt Lime, Part II: Diffusion of Carbon into Solid Lime", Scandinavian Journal of Metallurgy, Vol. 19, 1990b, PP 191-200.

Müller, M. B., "Structure, Properties and Reactions of CaO in Burnt Lime, Part III: Composite Reactions of CaO and C in Solid and Liquid State", Scandinavian Journal of Metallurgy, Vol. 19, 1990c, PP 210-217.

Munz, R. J., "Decomposition of Molybdenum Disulphide in an Induction Plasma Tailflame", Ph.D. Thesis, McGill University, 1974.

Munz, R. J. and E. J. Chin, "The Carbothermic Reduction of Niobium Pentoxide and Pyrochlore in a Transferred Arc Argon Plasma" Canadian Metallurgical Quarterly, Vol. 30, No., 1, 1991, PP. 21-29.

Munz, R. J. and E. J. Chin, "The Carbothermic Reduction of Niobium Pentoxide and Pyrochlore in the Presence of Iron in a Transferred Arc Argon Plasma" Canadian Metallurgical Quarterly, Vol. 31, No., 1, 1992, PP. 17-24.

Munz, R. J. and Mersereau O. S., "A Plasma Spout-Fluid Bed for the Recovery of Vanadium from Vanadium Ore", Chem. Eng. Sci., Vol. 45, (1990), PP. 2489-95.

Nakamura, M., Y. Hamada, S. Toyama, A. Fouda and C. Capes, "An Experimental Investigation of Minimum Fluidization Velocity at Elevated Temperature and Pressures", Canadian Journal of Chemical Engineering, Vol. 63, 1985, PP. 8-13.

Nienow, A. W. and D. J. Cheesman, in "Fluidization" ed. by J. R. Grace and J. R. Matsen, Plenum Press, New York (1980), PP. 373-380.

Okubo, T., Kawamura H., Kusakabe K. and Morooka S., "Plasma Nitriding of Titanium Particles in a Fluidized Bed Reactor at Reduced Pressure", J. Am. Ceram. Soc., Vol. 73, (1990), PP. 1150-1152.

Otsuka, K. and D. Kunii, "Reduction of Powdery Ferric Oxide Mixed with Graphite Particles" J. Chem. Eng. Japan, Vol. 2, No. 1, 1969.

Patterson P. A., "Laser Doppler Anemometry in Transferred-arc Plasma", M. Eng., McGill University, 1983.

Pattipati, R. R. and C. Y. Wen, "Minimum Fluidization Velocity at High Temperature", Ind. Eng. Chem. Process. Des. Dev., Vol. 20, 1981, PP. 705-708.

Pell, M., *Gas Fluidization*, Volume 8 in *Handbook of Powder Technology*, Elsevier Publishing Company, Amsterdam, 1990.

Pfender E., Boulos M., Fauchais P., "Methods and Principles of Plasma Generation", Chapter 4 in *Plasma Technology in Metallurgical Processing*, Ed. by Feinman J., Iron and Steel Society Inc., 1987.

Rao, Y. K., " The Kinetics of Reduction of Hematite by Carbon", Met. Trans., Vol. 2, 1971, PP. 1439-1447.

Rao, Y. K., "A Physico-chemical model for reactions between particulate Solids Occurring Through Gaseous Intermediates-I: Reduction of Hematite by Carbon" Chemical Engineering Science, Vol. 29, 1974.

Rogers, T. and Morin T. J., "Slip Flow in Fixed and Fluidized Bed Plasma Reactors", Plasma Chemistry and Plasma Processing, Vol. 11, (1991), PP. 203-228.

Roine, A., "Outokumpu HSC Chemistry for Windows", User's guide, Outokumpu Research Oy, 1994.

Rootare, H. M. and C. F. Prenzlow, "Surface Areas from Mercury Porosimeter Measurements" J. Phys. Chem., Vol. 71 (1967) PP. 2733-2736.

Rowe, P. N., A. W. Nienow and A. J. Agbim, Trans. Inst. Chem. Engrs., Vol 50 (1972a), PP. 310-323.

Rowe, P. N., A. W. Nienow and A. J. Agbim, Trans. Inst. Chem. Engrs., Vol 50 (1972b), PP. 323-333.

Sayegh N. N., "Variable Property Flow and Heat Transfer to Single Spheres", Ph.D. Thesis, McGill University, 1977.

Sharma, R. A., P. P. Bhatngar and T. J. Banerjee, Sci. Ind. Res., New Delhi, India, Vol. 16A, 1957.

Shine, N. B.,"Calcium Carbide", *Kirk-Othmer Encyclopedia of Chemical Technology*, Vol. 4, John Wiley & Sons, (1987).

Smith W. R. and **Missen R. W.,** *Chemical Reaction Equilibrium Analysis: Theory and Algorithms*, John Wiley & Sons, New York, 1982.

Sohn, H. Y. and J. Szekely, "Reactions Between Solids Through Gaseous Intermediates-I: Reactions Controlled by Chemical Kinetics", Chem. Eng. Sci., Vol. 28, 1973, PP. 1789-1801.

Stubington, J., D. Barrett and G. Lowry, "Minimum Fluidizing Velocity of Coal-derived Chars at Elevated Temperatures", Chem. Eng. Sci., Vol. 39, 1984, PP. 1516-1518.

Szekely, J. , J. W. Evans and H. Y. Sohn, *Gas-Solid Reactions*, Academic Press, New York, 1976.

Tagawa, H. and Sugawara H., "The Kinetics of the Formation of Calcium Carbide in Solid-Solid Reaction", Bull. Chem. Soc. Jap, vol. 35, (1962), PP. 1276-1279.

Tamhankar, S. S. and L. K. Doraiswamy, "Analysis of Solid-Solid Reactions: A Review", AIChE, Vol. 25, 1979.

Touloukian, Y. S., R. W. Powell, C. Y. Ho and P. G. Klemens, *Thermophysical Properties of Matter. Volume II: Thermal Conductivity of Non-metallic Solids*, IFI/Plenum Data Co., New York, 1970.

Tsikarev, D. A., "Determination of Reactivity of Coke for Calcium Carbide Production", Coke and Chemistry, No. 12 , December 1991, P 48.

Tuot, J., "The Electrothermal Fluidized Bed and Its Application to the Production of Titanium Carbide", Ph.D. Thesis, McGill University, 1976.

Wasburn, E. W., "Note on a Method of Determining the Distribution of Pore Sizes in a Porous Material", Proc. Nat. Acad. Sci., Vol. 7 (1921) PP. 115-116.

Wen, C. Y., " Non-cataiytic Heterogeneous Solid Fluid Reaction Models", Industrial and Engineering Chemistry, Vol. 60, No. 9, 1968, PP. 34-52.

White W. B., Johnson S. M. and **Dantzig G. B.,** "Chemical Equilibrium in Complex Mixtures", J. Chem. Phys., Vol. 28, No. 5, 1958, PP. 751 - 755.

Wierenga, C. R. and Morin T. J., "Characterization of a Plasma Fluidized Bed Reactor", AIChE Journal, Vol. 35, (1989), PP. 1555-1560.

Ye, B., C. J. Lim and J. R. Grace, "Hydrodynamics of Spouted and Spout-Fluidized Beds at High temperature", Canadian Journal of Chemical Engineering, Vol. 70, 1992, PP. 840-847.

Zhu, C. W., G. Y. Zhao and V. Hlavacek, "A d.c. Plasma-Fluidized Bed Reactor for the Production of Calcium Carbide", J. Mater. Sci., Vol. 30, 1995, PP. 2412-2419.

APPENDICES

APPENDIX A:

A sample thermodynamic analysis using FACT for Reaction (4.1)

$$CaO + 3C \rightarrow CaC_2 + CO$$

with the addition of two and twenty moles of Argon.

APPENDIX B:

Output data from mercury porosimetry analysis for a calcium oxide sample

APPENDIX C:

Raw data for fractional conversion for Figures 5.3, 5.7, 5.8, 5.9, 6.10, 6.14 and 6.15

APPENDIX A

```
>fact

F*A*C*T - Version 2.1
Montreal, Quebec, Canada
Copyright 1986-1996 Thermfact TD/LTEE
W.T. Thompson, A.D. Pelton, C.W. Bale


Welcome to FACT 2.1 - type "N" for the News of changes
   Type "I" for Info on WWW, graphics, Internet, ftp, capturing text, etc


*** Select a program - press <Enter> for the F*A*C*T menu
(or enter /Q to quit followed by /OFF to logoff)
>EQUIL

- loading

EQUILIBRIUM PRODUCT CALCULATION <F*A*C*T 2.1>
*********************************************

        - incorporating the thermochemical functions of ChemSage developed by
Dr. G. Eriksson in association with GTT GmbH, Aachen, Germany.

F*A*C*T database(s)      : COMPOUND, SOLUTION
        Private compounds database:
                USERBASE.DAT
Private solutions database: - none -
Site compounds database   : - none -

OPTIONS:  T(K).  P(atm).  Energy(J).
Reactants/Products(X).
 Thermodynamic properties (TH).  No compressibilities
(NOCOMP).
    No gas ions (NOGION).  Ideal gas (NOGREAL).  Aqueous species (AQUA).
 Maximum organic carbon atoms (CXHY) x =  2.  NoCC.  NoExt.
 Printing cut-off (CUT)= 1.E-10.  Printing pause (LINES)=  24
 Regular version - up to 16 elements.

Last reaction:
   CA*O + 3C + 2AR=
 L) Load the last reaction
 N) enter a New reaction
 I) quick Introduction to getting
started
 W) Worked examples & sample
```

calculations
C) go to Command level

· LIST (Help ALL G LIQ AQ SOLID SOLN LOC ACT MOL DIST DATA) >L G

	#	SPECIES	PHASE	CP RANGE (K)
	1	C	<- G1 Gas	298 - 6000
	2	C2	<- G1 Gas	298 - 6000
	3	C3	<- G1 Gas	298 - 6000
	4	C4	<- G1 Gas	298 - 6000
	5	C5	<- G1 Gas	298 - 6000
	6	O	<- G1 Gas	298 - 6000
	7	O2	<-	298 - 6000
	8	O3	<- G1 Gas	298 - 6000
	9	C1O1	<- G1 Gas	298 - 6000
	10	C2O	<- G1 Gas	298 - 6000
	11	C1O2	<- G1 Gas	298 - 6000
	12	C3O2	<- G1 Gas	298 - 6000
	13	C	G1 Gas	298 - 6000
	14	C2	G1 Gas-1	298 - 6000
	15	C3	G1 Gas-1	298 - 6000
	16	C4	G1 Gas-1	298 - 6000
	17	C5	G1 Gas-1	298 - 6000
	18	O	G1 Gas-1	298 - 6000
	19	O2	v G1 Gas	298 - 6000
	20	O3	v G1 Gas-1	298 - 6000
+	21	CO	v G1 Gas-1	298 - 6000
>				
	22	C2O	G1 Gas-1	298 - 6000
	23	CO2	v G1 Gas	298 - 6000
+	24	C3O2		298 - 6000
+	25	Ar	v G1 Gas-1	298 - 6000
	26	Ca	G1 Gas-1	298 - 6000
	27	Ca2	G1 Gas-1	298 - 6000
	28	CaO	G1 gas	298 - 6000

"<-" denotes private user-supplied data
"+" denotes current species selection
"v" denotes virial (gas) or compressibility (s, liq) data available
- see Options GREAL/NOGREAL or COMP/NOCOMP

- LIST (Help ALL G LIQ AQ SOLID SOLN LOC ACT MOL DIST DATA) -L S

	#	SPECIES	PHASE	CP RANGE(K)
--				
	31	C <-	S1 Graphite	298 -6000
+	32	C	Graphite	298 - 6000
	33	C	S2 diamond	298 - 1200 T
	34	Ca	S1 Solid Alph	298 - 1501 T
	35	Ca	S2 Solid Beta	298 - 1501 T
	36	CaC2	S1 Solid-A	298 - 720 T
+	37	CaC2	S2 Solid-B	720 - 1275 T
+	38	CaO	S1 lime	298 - 3500
	40	CaCO3	S1 Aragonite	298 - 1200 T
	41	CaCO3	S2 Calcite	298 - 1200 T

"<-" denotes private user-supplied data
"+" denotes current species selection
"T" denotes temperature outside Cp range at 2200 00 (K)
+ LIST (Help ALL G LIQ AQ SOLID SOLN LOC ACT MOL DIST
DATA..) >
!
CaO + 3C + 2Ar=
(298.15K,1ATM,S1) (298.15K,1ATM,S1) (298.15K,1ATM,G)
(
1500,2200,50) 1
1 - 28 GASES (private: 1 - 12)
29 - 30 LIQUIDS
31 - 41 SOLIDS (private: 31 - 31)

21,25,26/32,37,38

ENTER FINAL STATES (/H)

****

`(1500,2200,50) 1
+ FINAL CONDITIONS (Help)

>(1500,2200,50) 1
- total number of calculations from parentheses () = 15
+ ENTER COMMAND (Help, W, R, F, S, L, O, E, EX)
>E

EQUILIBRIUM (Help, EXecute, MAp, OPEN, CLIMit)
-EX

CaO + 3C + 2Ar=

2.0001 mol (0.99993 Ar
+ 0.36386E-04 CO
+ 0.36386E-04 Ca)
(1500.00 K, 1.0000 atm, gas_ideal)

+ 2.9999 mol C
(1500.00 K, 1.0000 atm, S1, a= 1.0000)
+ 0.99993 mol CaO
(1500.00 K, 1.0000 atm, S1, a= 1.0000)

+ 0.00000E+00 mol CaC2
(1500.00 K, 1.0000 atm, S2, a=0.64981)

The cutoff concentration has been specified to 1.000E-10 .
Data on 1 product species identified with "T" have been extrapolated Data on 1 product species identified with "<---" or "<--s" have been drawn from your private data collection

>

CaO + 3C + 2Ar=

2.0004 mol (0.99982 Ar
+ 0.87670E-04 CO
+ 0.87670E-04 Ca)
(1550.00 K, 1.0000 atm, gas_ideal)

+ 2.9998 mol C
(1550.00 K, 1.0000 atm, S1, a= 1.0000)
+ 0.99982 mol CaO
(1550.00 K, 1.0000 atm, S1, a= 1.0000)

+ 0.00000E+00 mol CaC2
(1550.00 K, 1.0000 atm, S2, a=0.89574)

The cutoff concentration has been specified to 1.000E-10
Data on 1 product species identified with "T" have been extrapolated Data on 1 product species identified with "<---" or "<--s" have been drawn from your private data collection

>

CaO + 3C + 2Ar=

2.0008 mol (0.99959 Ar
+ 0.24148E-03 CO
+ 0.16509E-03 Ca)
(1600.00 K, 1.0000 atm, gas_ideal)
+ 2.9992 mol C
(1600.00 K, 1.0000 atm, S1, a= 1.0000)
+ 0.99952 mol CaO
(1600.00 K, 1.0000 atm, S1, a= 1.0000)

+ 0.15285E-03 mol CaC2
(1600.00 K, 1.0000 atm, S2, a=1.0000)

The cutoff concentration has been specified to 1.000E-10
Data on 1 product species identified with "T" have been extrapolated Data on 1 productspecies identified with "<---" or "<--s" have been drawn from your private data collection

>

CaO + 3C + 2Ar=

2.0019 mol (0.99904 Ar
+ 0.69236E-03 CO
+ 0.26959E-03 Ca)
(1650.00 K, 1.0000 atm, gas_ideal)

+ 2.9969mol C
(1650.00 K, 1.0000 atm, S1, a= 1.0000)
+ 0.99861mol CaO
(1650.00 K, 1.0000 atm, S1, a= 1.0000)

+ 0.84635E-03 mol CaC2 T
(1650.00 K, 1.0000 atm, S2, a= 1.0000)

The cutoff concentration has been specified to 1.000E-10
Data on 1 product species identified with "T" have been extrapolated Data on 1 product species identified with "<---" or "<--s" have been drawn from your private data collection

>

CaO + 3C + 2Ar=

2.0046 mol (0.99771 Ar
+ 0.18623E-02 CO

+ 0.42746E-03 Ca)
(1700.00 K, 1.0000 atm, gas_ideal)
+ 2.9905mol C
(1700.00 K, 1.0000 atm, S1, a= 1.0000)

+ 0.99627mol CaO
(1700.00 K, 1.0000 atm, S1, a= 1.0000)

+ 0.28763E-02 mol CaC2 T
(1700.00 K, 1.0000 atm, S2, a= 1.0000)

The cutoff concentration has been specified to 1.000E-10
Data on 1 product species identified with "T" have been extrapolated Data on 1 product species identified with "<---" or "<--s" have been drawn from your private data collection

>

CaO + 3C + 2Ar=

2.0108 mol (0.99461 Ar
+ 0.47256E-02 CO
+ 0.65981E-03 Ca)
(1750.00 K, 1.0000 atm, gas_ideal)
+ 2.9741mol C
(1750.00 K, 1.0000 atm, S1, a= 1.0000)

+ 0.99050mol CaO
(1750.00 K, 1.0000 atm, S1, a= 1.0000)

+ 0.81755E-02 mol CaC_2 T
(1750.00 K, 1.0000 atm, S2, a= 1.0000)

The cutoff concentration has been specified to 1.000E-10
Data on 1 product species identified with "T" have been extrapolated Data on 1 product species identified with "<---" or "<--s" have been drawn from your private data collection

>

CaO + 3C + 2Ar=

2.0250 mol (0.98764 Ar
+ 0.11367E-01 CO
+ 0.99368E-03 Ca)
(1800.00 K, 1.0000 atm, gas_ideal)
+ 2.9350 mol C
(1800.00 K, 1.0000 atm, S1, a= 1.0000)

+ 0.97698mol CaO
(1800.00 K, 1.0000 atm, S1, a= 1.0000)

+ 0.21006E-01 mol CaC_2 T
(1800.00 K, 1.0000 atm, S2, a= 1.0000)

The cutoff concentration has been specified to 1.000E-10
Data on 1 product species identified with "T" have been extrapolated Data on 1 product species identified with "<---" or "<--s" have been drawn from your private data collection

>

CaO + 3C + 2Ar=

2.0565 mol (0.97251 Ar
+ 0.26031E-01 CO
+ 0.14631E-02 Ca)
(1850.00 K, 1.0000 atm, gas_ideal)
+ 2.8454mol C
(1850.00 K, 1.0000 atm, S1, a= 1.0000)

+ 0.94647mol CaO
(1850.00 K, 1.0000 atm, S1, a= 1.0000)

+ 0.50525E-01 mol CaC_2 T
(1850.00 K, 1.0000 atm, S2, a= 1.0000)

The cutoff concentration has been specified to 1.000E-10
Data on 1 product species identified with "T" have been extrapolated Data on 1 product species identified with "<---" or "<--s" have been drawn from your private data collection

>

CaO + 3C + 2Ar=

2.1256 mol (0.94091 Ar
+ 0.56979E-01 CO
+ 0.21100E-02 Ca)
(1900.00 K, 1.0000 atm, gas_ideal)

+ 2.6456mol C
(1900.00 K, 1.0000 atm, S1, a= 1.0000)

+ 0.87888mol CaO
(1900.00 K, 1.0000 atm, S1, a= 1.0000)
+ 0.11663mol CaC_2 T
(1900.00 K, 1.0000 atm, S2, a= 1.0000)

The cutoff concentration has been specified to 1.000E-10
Data on 1 product species identified with "T" have been extrapolated Data on 1 product species identified with "<---" or "<--s" have been drawn from your private data collection

CaO + 3C + 2Ar=

2.2795 mol (0.87739 Ar
+ 0.11963 CO
+ 0.29852E-02 Ca)
(1950.00 K, 1.0000 atm, gas_ideal)

+ 2.1955mol C
(1950.00 K, 1.0000 atm, S1, a= 1.0000)

+ 0.72731mol CaO
(1950.00 K, 1.0000 atm, S1, a= 1.0000)

+ 0.26588 mol CaC_2 T
(1950.00 K, 1.0000 atm, S2, a=1.0000)

The cutoff concentration has been specified to 1.000E-10
Data on 1 product species identified with "T" have been extrapolated Data on 1 product species identified with "<---" or "<--s" have been drawn from your private data collection

CaO + 3C + 2Ar=

2.6518 mol (0.75420 Ar
+ 0.24165 CO
+ 0.41495E-02 Ca)
(2000.00 K, 1.0000 atm, gas_ideal)
+ 1.0995 mol C
(2000.00 K, 1.0000 atm, S1, a= 1.0000)

+ 0.62982 mol CaC_2 T
(2000.00 K, 1.0000 atm, S2, a= 1.0000)
+ 0.35917 mol CaO
(2000.00 K, 1.0000 atm, S1, a= 1.0000)

The cutoff concentration has been specified to 1.000E-10
Data on 1 product species identified with "T" have been extrapolated Data on 1 productspecies identified with "<---" or "<--s" have been drawn from your private data collection

CaO + 3C + 2Ar=

3.0171 mol (0.66288 Ar
+ 0.33144 CO
+ 0.56742E-02 Ca)
(2050.00 K, 1.0000 atm, gas_ideal)

+ 0.98288 mol CaC_2 T
(2050.00 K, 1.0000 atm, S2, a = 1.0000)

+ 0.34240E-01 mol C
(2050.00 K, 1.0000 atm, S1, a= 1.0000)

+ 0.00000E+00 mol CaO
(2050.00 K, 1.0000 atm, S1, a=0.70366)

The cutoff concentration has been specified to 1.000E-10
Data on 1 product species identified with "T" have been extrapolated Data on 1 product species identified with "<---" or "<--s" have been drawn from your private data collection

>

CaO + 3C + 2Ar=

3.0231 mol (0.66157 Ar
+ 0.33079 CO
+ 0.76425E-02 Ca)
(2100.00 K, 1.0000 atm, gas_ideal)

+ 0.97690 mol CaC_2 T
(2100.00 K, 1.0000 atm, S2, a= 1.0000)

+ 0.46208E-01 mol C
(2100.00 K, 1.0000 atm, S1, a= 1.0000)

+ 0.00000E+00 mol CaO
(2100.00 K, 1.0000 atm, S1, a=0.37243)

The cutoff concentration has been specified to 1.000E-10
Data on 1 product species identified with "T" have been extrapolated Data on 1 product species identified with "<---" or "<--s" have been drawn from your private data collection

CaO + 3C + 2Ar=

3.0000 mol (0.66667 Ar
+ 0.33333 CO)
(2150.00 K, 1.0000 atm, gas_ideal)
+ 1.0000 mol CaC_2 T
(2150.00 K, 1.0000 atm, S2, a= 1.0000)

The cutoff concentration has been specified to 1.000E-10
Data on 1 product species identified with "T" have been extrapolated

CaO + 3C + 2Ar=

3.0000 mol (0.66667 Ar
+ 0.33333 CO)
(2200.00 K, 1.0000 atm, gas_ideal)
+ 1.0000 mol CaC_2 T
(2200.00 K, 1.0000 atm, S2, a= 1.0000)

The cutoff concentration has been specified to 1.000E-10
Data on 1 product species identified with "T" have been extrapolated

****
**
*

+ REACTION (Help, NEW, EDit, OLD, SAve, DIR, VIew, DEL, REN)
>ED

`CA*O + 3C + 2AR=
+ REACTION (Help, NEW, EDit, OLD, SAve, DIR, VIew, DEL, REN)

>CA*O + 3C + 20AR=
+ REACTION (Help, NEW, EDit, OLD, SAve, DIR, VIew, DEL, REN)
****
**

(1500,2200,50) 1
1 - 28 GASES (private: 1 - 12)
29 - 30 LIQUIDS
31 - 41 SOLIDS (private: 31 - 31)

/21,25,26/32,37,38
+ EQUILIBRIUM (Help, EXecute, MAp, OPEN, CLIMit)

EX

CaO + 3C + 20Ar=

20.001 mol (0.99993 Ar
- 0.36386E-04 CO
- 0.36386E-04 Ca)
(1500.00 K, 1.0000 atm,gas ideal)

+ 2.9993 mol C
(1500.00 K, 1.0000 atm, S1, a= 1.0000)
+ 0.99927 mol CaO
(1500.00 K, 1.0000 atm, S1, a= 1.0000)

+ 0.00000E+00 mol CaC_2 T
(1500.00 K, 1.0000 atm, S2, a=0.64981)

The cutoff concentration has been specified to 1.000E-10
Data on 1 product species identified with "T" have been extrapolated Data on 1 product species identified with "<---" or "<--s" have been drawn from your private data collection

>

CaO + 3C + 20Ar=

20.004 mol (0.99982 Ar
+ 0.87670E-04 CO
+ 0.87670E-04 Ca)
(1550.00 K, 1.0000 atm, gas_ideal)

+ 2.9982 mol C
(1550.00 K, 1.0000 atm, S1, a= 1.0000)
+ 0.99825 mol CaO
(1550.00 K, 1.0000 atm, S1, a= 1.0000)

+ 0.00000E+00 mol CaC_2 T
(1550.00 K, 1.0000 atm, S2, a=0.89574)

The cutoff concentration has been specified to 1.000E-10
Data on 1 product species identified with "T" have been extrapolated Data on 1 product species identified with "<---" or "<--s" have been drawn from your private data collection

>

CaO + 3C + 20Ar=

20.008 mol (0.99959 Ar
- 0.24148E-03 CO
- 0.16509E-03 Ca)
(1600.00 K, 1.0000 atm, gas_ideal)

- 2.9921 mol C
(1600.00 K, 1.0000 atm, S1, a= 1.0000)
- 0.99517 mol CaO
(1600.00 K, 1.0000 atm, S1, a= 1.0000)

- 0.15285E-02 mol CaC_2 T
(1600.00 K, 1.0000 atm, S2, a= 1.0000)

The cutoff concentration has been specified to 1.000E-10
Data on 1 product species identified with "T" have been extrapolated Data on 1 product species identified with "<---" or "<--s" have been drawn from your private data collection

>

CaO + 3C + 20Ar=

20.019 mol (0.99904 Ar
+ 0.69236E-03 CO
+ 0.26959E-03 Ca)
(1650.00 K, 1.0000 atm, gas_ideal)
+ 2.9692 mol C
(1650.00 K, 1.0000 atm, S1, a= 1.0000)

+ 0.98614 mol CaO
(1650.00 K, 1.0000 atm, S1, a= 1.0000)

+ 0.84635E-02 mol CaC_2 T
(1650.00 K, 1.0000 atm, S2, a= 1.0000)

The cutoff concentration has been specified to 1.000E-10
Data on 1 product species identified with "T" have been extrapolated Data on 1 product species identified with "<---" or "<--s" have been drawn from your private data collection

>

CaO + 3C + 20Ar=
20.046 mol (0.99771 Ar
+ 0.18623E-02 CO
+ 0.42746E-03 Ca)
(1700.00 K, 1.0000 atm, gas_ideal)

- 2.9051mol C
  (1700.00 K, 1.0000 atm, S1, a 1.0000)

- 0.96267mol CaO
  (1700.00 K, 1.0000 atm, S1, a 1.0000)

- 0.28763E-01 mol CaC_2 T
  (1700.00 K, 1.0000 atm, S2, a 1.0000)

The cutoff concentration has been specified to 1.000E-10
Data on 1 product species identified with "T" have been extrapolated Data on 1 product species identified with "<---" or "<--s" have been drawn from your private data collection

CaO + 3C + 20Ar=

20.108 mol (0.99461 Ar
- 0.47256E-02 CO
+ 0.65981E-03 Ca)
(1750.00 K, 1.0000 atm, gas_ideal)

+ 2.7415mol C
(1750.00 K, 1.0000 atm, S1, a=1.0000)
+ 0.90498mol CaO
(1750.00 K, 1.0000 atm, S1, a=1.0000)

+ 0.81755E-01 mol CaC_2 T
(1750.00 K, 1.0000atm, S2, a=1.0000)

The cutoff concentration has been specified to 1.000E-10
Data on 1 product species identified with "T" have been extrapolated Data on 1 product species identified with "<---" or "<--s" have been drawn from your private data collection

CaO + 3C + 20Ar=

20.250 mol (0.98764 Ar
+ 0.11367E-01 CO
+ 0.99368E-03 Ca)
(1800.00 K, 1.0000 atm, gas_ideal)

+ 2.3497mol C
(1800.00 K, 1.0000 atm, S1, a=1.0000)

+ 0.76982mol CaO
(1800.00 K, 1.0000 atm, S1, a=1.0000)

+ 0.21006mol CaC_2 T
(1800.00 K, 1.0000 atm, S2, a=1.0000)

The cutoff concentration has been specified to 1.000E-10
Data on 1 product species identified with "T" have been extrapolated Data on 1 product species identified with "<---" or "<--s" have been drawn from your private data collection

CaO + 3C + 20Ar=

20.565 mol (0.97251 Ar
+ 0.26031E-01 CO
+ 0.14631E-02 Ca)

(1850.00 K, 1.0000 atm, gas_ideal)

+ 1.4542mol C
(1850.00 K, 1.0000 atm, S1, a=1.0000)
+ 0.50525mol CaC2 T
(1850.00 K, 1.0000 atm, S2, a= 1.0000)
+ 0.46466mol CaO
(1850.00 K, 1.0000atm)

The cutoff concentration has been specified to 1.000E-10
Data on 1 product species identified with "T" have been extrapolated Data on 1 product species identified with "<---" or "<--s" have been drawn from your private data collection

CaO + 3C + 20Ar=

21.044 mol (0.95037 Ar
+ 0.47519E-01 CO
+ 0.21100E-02 Ca)
(1900.00 K, 1.0000 atm, gas_ideal)

+ 0.95560mol CaC_2 T
(1900.00 K, 1.0000 atm, S2, a= 1.0000)
+ 0.88807E-01 mol C
(1900.00 K, 1.0000 atm, S1, a= 1.0000)

+ 0.00000E+00 mol CaO
(1900.00 K, 1.0000 atm, S1, a=0.83396)

The cutoff concentration has been specified to 1.000E-10

Data on 1 product species identified with "T" have been extrapolated Data on 1 product species identified with "<---" or "<--s" have been drawn from your private data collection

CaO + 3C + 20Ar=

21.063 mol

(0.94954 Ar
+ 0.47477E-01 CO
+ 0.29852E-02 Ca)
(1950.00 K, 1.0000 atm, gas_ideal)

+ 0.93712mol CaC_2 T
(1950.00 K, 1.0000 atm, S2, a= 1.0000)
+ 0.12575mol C
(1950.00 K, 1.0000 atm, S1, a= 1.0000)

+ 0.00000E+00 mol CaO
(1950.00 K, 1.0000 atm, S1, a=0.39687)

The cutoff concentration has been specified to 1.000E-10
Data on 1 product species identified with "T" have been extrapolated Data on 1 product species identified with "<---" or "<--s" have been drawn from your private data collection

CaO + 3C + 20Ar=

21.088 mol

(0.94843 Ar
+ 0.47421E-01 CO
+ 0.41495E-02 Ca)
(2000.00 K, 1.0000 atm, gas_ideal)
+ 0.91250mol CaC_2 T
(2000.00 K, 1.0000 atm, S2, a= 1.0000)
+ 0.17500mol C
(2000.00 K, 1.0000 atm, S1, a= 1.0000)

+ 0.00000E+00 mol CaO

(2000.00 K, 1.0000 atm, S1, a= 0.19624)

The cutoff concentration has been specified to 1.000E-10
Data on 1 product species identified with "T" have been extrapolated Data on 1 product species identified with "<---" or "<--s" have been drawn from your private data collection

CaO + 3C + 20Ar=

21.120 mol (0.94698 Ar
+ 0.47349E-01 CO
+ 0.56742E-02 Ca)
(2050.00 K, 1.0000 atm, gas_ideal)

+ 0.88016mol CaC_2 T
(2050.00 K, 1.0000 atm, S2, a= 1.0000)
+ 0.23968mol C
(2050.00 K, 1.0000 atm, S1, a= 1.0000)

+ 0.00000E+00 mol CaO
(2050.00 K, 1.0000 atm, S1, a=0.10052)

The cutoff concentration has been specified to 1.000E-10
Data on 1 product species identified with "T" have been extrapolated Data on 1 product species identified with "<---" or "<--s" have been drawn from your private data collection

CaO + 3C + 20Ar=

21.162 mol (0.94510 Ar
+ 0.47255E-01 CO
+ 0.76425E-02 Ca)
(2100.00 K, 1.0000 atm, gas_ideal)

+ 0.83827 mol CaC_2 T
(2100.00 K,1.0000 atm, S2, a= 1.0000)

+ 0.32346 mol C
(2100.00 K,1.0000 atm, S1, a= 1.0000)

+ 0.00000E+00 mol CaO
(2100.00 K,1.0000 atm, S1, a=0.053)

The cutoff concentration has been specified to 1.000E-10
Data on 1 product species identified with "T" have been extrapolated Data on 1 product species identified with "<---" or "<--s" have been drawn from your private data collection

CaO + 3C + 20Ar=

21.000 mol (0.95238 Ar
+ 0.47619E-01 CO)
(2150.00 K, 1.0000 atm, gas_ideal)

+ 1.0000 mol CaC_2 T

(2150.00 K, 1.0000 atm, S2, a= 1.0000)

The cutoff concentration has been specified to 1.000E-10
Data on 1 product species identified with "T" have been extrapolated

CaO + 3C + 20Ar=
21.000 mol (0.95238 Ar
+ 0.47619E-01 CO)
(2200.00 K, 1.0000 atm, gas_ideal)

+ 1.0000 mol CaC_2 T
(2200.00 K, 1.0000 atm, S2, a= 1.0000)

The cutoff concentration has been specified to 1.000E-10
Data on 1 product species identified with "T" have been extrapolated

APPENDIX B

```
PORESIZER 9320 V2 05
SAMPLE DIRECTORY/NUMBER: MUFTAH  /5
OPERATOR: M.E.
SAMPLE ID: CaO RUN3
SUBMITTER: M.E.

PENETROMETER NUMBER:          14-0379
ADVANCING CONTACT ANGLE:      130.0 deg
PENETROMETER CONSTANT:        10.79 µL/pF
RECEDING CONTACT ANGLE:       130.0 deg
PENETROMETER WEIGHT:          69.5718 g
MERCURY SURFACE TENSION:      485.0 dyn/cm
STEM VOLUME:                  0.4120 mL
MERCURY DENSITY:              13.5426 g/mL
MAXIMUM HEAD PRESSURE:        4.6800 psi
SAMPLE WEIGHT:                0.4027 g
PENETROMETER VOLUME:          3.2725 mL

SAMPLE+PEN+Hg WEIGHT: 108.8282 g

LOW PRESSURE:
       MERCURY FILLING PRESSURE:          1.6353 psia
         LAST LOW PRESSURE POINT:           5.9629 psia

  HIGH PRESSURE:
  RUN TYPE:                  AUTOMATIC
  RUN METHOD:                EQUILIBRATED
EQUILIBRATION TIME:           10 seconds
                  INTRUSION DATA SUMMARY
             TOTAL INTRUSION VOLUME =    0.6409 mL/g
                    TOTAL PORE AREA =     1.153 sq-m/g
       MEDIAN PORE DIAMETER (VOLUME) =    2.3995 µm
         MEDIAN PORE DIAMETER (AREA) =    0.9948 µm
        AVERAGE PORE DIAMETER (4V/A) =    1.6672 µm
                         BULK DENSITY =    0.9980 g/mL
       APPARENT (SKELETAL) DENSITY =      2.7690 g/mL
                           POROSITY =      63.96 %
                  STEM VOLUME USED =         63 %
```

POROSIZER 9320 V2.05
SAMPLE DIRECTORY/NUMBER: MUFTAH /5
OPERATOR: M.E.
SUBMITTER: M.E.

PRES. psia	PORE DIAMETER µm	INCREMENTAL VOLUME mL/g	DIFFEREN. VOL dV/dD mL/g-µm	CUMUL. PORE AREA sq-m/g	INC. P.AREA sq-m/g
1.64	110.5971	0.0000	1.954E-04	0.000	0.000
3.22	56.1367	0.0149	5.313E-04	0.001	0.001
7.10	25.4803	0.0612	3.137E-03	0.007	0.006
11.50	15.7281	0.0376	4.960E-03	0.014	0.007
13.85	13.0615	0.0150	6.089E-03	0.018	0.004
16.03	11.2862	0.0119	6.205E-03	0.022	0.004
18.92	9.5611	0.0103	7.960E-03	0.026	0.004
22.02	8.2153	0.0142	1.059E-02	0.032	0.006
24.13	7.4945	0.0074	9.766E-03	0.036	0.004
25.96	6.9662	0.0065	8.631E-03	0.040	0.004
28.85	6.2698	0.0030	9.971E-03	0.042	0.002
30.50	5.9308	0.0040	1.238E-02	0.044	0.003
35.42	5.1055	0.0154	2.010E-02	0.055	0.011
40.53	4.4629	0.0143	2.613E-02	0.067	0.012
45.13	4.0077	0.0139	3.374E-02	0.080	0.013
50.22	3.6012	0.0160	4.243E-02	0.097	0.017
54.99	3.2890	0.0143	5.033E-02	0.114	0.017
60.08	3.0102	0.0160	5.877E-02	0.134	0.020
64.85	2.7888	0.0139	6.712E-02	0.153	0.019
70.45	2.5674	0.0160	7.630E-02	0.177	0.024
74.72	2.4205	0.0127	8.277E-02	0.198	0.020
90.21	2.0048	0.0386	1.021E-01	0.267	0.070
100.77	1.7948	0.0235	1.200E-01	0.317	0.049
120.58	1.4999	0.0419	1.658E-01	0.419	0.102
150.31	1.2033	0.0595	2.149E-01	0.595	0.176
175.63	1.0298	0.0396	2.243E-01	0.736	0.142
200.99	0.8998	0.0293	2.116E-01	0.858	0.121
250.83	0.7211	0.0356	1.775E-01	1.033	0.176
274.95	0.6578	0.0109	1.583E-01	1.097	0.063
301.08	0.6007	0.0082	1.404E-01	1.149	0.052
325.88	0.5550	0.0063	1.279E-01	1.193	0.044
351.03	0.5152	0.0049	1.164E-01	1.230	0.037
400.33	0.4518	0.0067	9.463E-02	1.285	0.055
450.81	0.4012	0.0044	7.704E-02	1.326	0.041
501.63	0.3606	0.0028	6.491E-02	1.355	0.029

600.78	0.3010	0.0035	5.093E-02	1.398	0.042
801.43	0.2257	0.0032	3.452E-02	1.446	0.048
998.76	0.1811	0.0014	2.881E-02	1.473	0.028
1199.76	0.1508	0.0008	2.482E-02	1.494	0.020
1399.09	0.1293	0.0005	1.721E-02	1.507	0.014
1597.75	0.1132	0.0002	1.244E-02	1.514	0.007
1795.42	0.1007	0.0001	1.316E-02	1.520	0.006
1995.75	0.0906	0.0001	1.483E-02	1.526	0.006
2498.09	0.0724	0.0002	5.333E-03	1.538	0.012
2996.42	0.0604	0.0000	0.000E+00	1.538	0.000
3494.76	0.0518	0.0000	0.000E+00	1.538	0.000
3991.76	0.0453	0.0000	0.000E+00	1.538	0.000
4493.09	0.0403	0.0000	0.000E+00	1.538	0.000
4988.93	0.0363	0.0000	0.000E+00	1.538	0.000
5988.26	0.0302	0.0000	0.000E+00	1.538	0.000
6984.43	0.0259	0.0000	0.000E+00	1.538	0.000
7982.77	0.0227	0.0000	0.000E+00	1.538	0.000
8988.77	0.0201	0.0000	0.000E+00	1.538	0.000
9987.28	0.0181	0.0000	0.000E+00	1.538	0.000
11980.78	0.0151	0.0000	0.000E+00	1.538	0.000
14976.12	0.0121	0.0000	0.000E+00	1.538	0.000
16971.13	0.0107	0.0000	0.000E+00	1.538	0.000
18970.80	0.0095	0.0000	0.000E+00	1.538	0.000
21966.97	0.0082	0.0000	0.000E+00	1.538	0.000
24957.65	0.0072	0.0000	0.000E+00	1.538	0.000
29948.16	0.0060	0.0000	0.000E+00	1.538	0.000
24990.98	0.0072	-0.0026	6.459E-01	-0.041	-1.579
21999.46	0.0082	0.0000	6.993E-05	-0.041	0.000
18999.62	0.0095	0.0000	0.000E+00	-0.041	0.000
17004.77	0.0106	0.0000	0.000E+00	-0.041	0.000
15003.27	0.0121	0.0000	0.000E+00	-0.041	0.000
12009.25	0.0151	0.0000	0.000E+00	-0.041	0.000
10005.41	0.0181	0.0000	0.000E+00	-0.041	0.000
9010.74	0.0201	0.0000	0.000E+00	-0.041	0.000
8007.41	0.0226	0.0000	0.000E+00	-0.041	0.000
7006.40	0.0258	0.0000	0.000E+00	-0.041	0.000
6004.40	0.0301	0.0000	0.000E+00	-0.041	0.000
5008.73	0.0361	0.0000	0.000E+00	-0.041	0.000
4503.73	0.0402	0.0000	0.000E+00	-0.041	0.000
4001.23	0.0452	0.0000	0.000E+00	-0.041	0.000
3503.23	0.0516	0.0000	0.000E+00	-0.041	0.000
3002.23	0.0602	0.0000	0.000E+00	-0.041	0.000
2505.06	0.0722	0.0000	0.000E+00	-0.041	0.000
1998.73	0.0905	0.0000	0.000E+00	-0.041	0.000
1804.56	0.1002	0.0000	0.000E+00	-0.041	0.000
1603.06	0.1128	0.0000	0.000E+00	-0.041	0.000
1405.40	0.1287	0.0000	0.000E+00	-0.041	0.000
1199.57	0.1508	0.0000	0.000E+00	-0.041	0.000

999.90	0.1809	0.0000	0.000E+00	-0.041	0.000
799.90	0.2261	0.0000	0.000E+00	-0.041	0.000
597.07	0.3029	0.0000	0.000E+00	-0.041	0.000
501.57	0.3606	0.0000	0.000E+00	-0.041	0.000
445.07	0.4064	0.0000	0.000E+00	-0.041	0.000
389.58	0.4643	0.0000	0.000E+00	-0.041	0.000
346.41	0.5221	0.0000	0.000E+00	-0.041	0.000
324.08	0.5581	0.0000	0.000E+00	-0.041	0.000
300.58	0.6017	0.0000	0.000E+00	-0.041	0.000
273.75	0.6607	0.0000	5.831E-07	-0.041	0.000
249.76	0.7242	0.0000	3.352E-04	-0.041	0.000
199.76	0.9054	-0.0007	8.928E-03	-0.044	-0.003
174.27	1.0378	-0.0014	1.067E-02	-0.050	-0.006
150.78	1.1995	-0.0016	9.650E-03	-0.056	-0.006
120.29	1.5036	-0.0027	8.618E-03	-0.064	-0.008
100.30	1.8032	-0.0026	9.527E-03	-0.070	-0.006
90.48	1.9990	-0.0020	1.116E-02	-0.074	-0.004
75.66	2.3903	-0.0044	1.087E-02	-0.082	-0.008
70.34	2.5713	-0.0019	1.117E-02	-0.085	-0.003
64.85	2.7889	-0.0025	1.253E-02	-0.089	-0.004
59.37	3.0466	-0.0034	1.428E-02	-0.094	-0.005
55.38	3.2658	-0.0032	1.562E-02	-0.098	-0.004
49.58	3.6482	-0.0063	1.777E-02	-0.105	-0.007
45.11	4.0097	-0.0066	1.961E-02	-0.112	-0.007
40.15	4.5043	-0.0102	2.305E-02	-0.121	-0.010
34.57	5.2320	-0.0179	2.517E-02	-0.136	-0.015
29.51	6.1296	-0.0229	2.977E-02	-0.152	-0.016
28.22	6.4090	-0.0103	2.977E-02	-0.159	-0.007
25.96	6.9682	-0.0150	2.737E-02	-0.168	-0.009

APPENDIX C

Table C1: Fractional conversion (X) at different conditions Raw data for Figure 5.3

Run Time (min)	*H_2= 0% P=5 kW*	*H_2= 33% P=12 kW*	*H_2=45% P=14 kW*	*H_2= 67% P=18 kW*
0.0000	0.0000	0.0000	0.0000	0.0000
1.0000	1.0932e-3	2.1863e-3	4.0994e-3	4.0994e-3
2.0000	2.0497e-3	3.9627e-3	6.8323e-3	8.6087e-3
3.0000	3.9627e-3	7.7888e-3	0.0120	0.0190
4.0000	4.9192e-3	9.5652e-3	0.0145	0.0243
5.0000	6.5590e-3	0.0131	0.0200	0.0353
6.0000	7.3789e-3	0.0148	0.0228	0.0403
7.0000	8.7453e-3	0.0178	0.0277	0.0512
8.0000	9.2919e-3	0.0191	0.0301	0.0570
9.0000	0.0104	0.0224	0.0361	0.0687
10.0000	0.0109	0.0245	0.0391	0.0728
11.0000	0.0120	0.0283	0.0456	0.0791
12.0000	0.0124	0.0299	0.0488	0.0823
13.0000	0.0133	0.0332	0.0567	0.0883
14.0000	0.0137	0.0348	0.0600	0.0937
15.0000	0.0145	0.0376	0.0660	0.1129
16.0000	0.0149	0.0389	0.0682	0.1211
17.0000	0.0157	0.0417	0.0731	0.1388
18.0000	0.0160	0.0435	0.0760	0.1470
19.0000	0.0165	0.0476	0.0817	0.1566
20.0000	0.0168	0.0493	0.0843	0.1611
21.0000	0.0174	0.0529	0.0884	0.1726
22.0000	0.0176	0.0548	0.0911	0.1776
23.0000	0.0182	0.0581	0.0969	0.1864
24.0000	0.0184	0.0593	0.0995	0.1921
25.0000	0.0190	0.0609	0.1036	0.2033
26.0000	0.0193	0.0618	0.1058	0.2096
27.0000	0.0198	0.0656	0.1101	0.2208
28.0000	0.0201	0.0670	0.1126	0.2263
29.0000	0.0206	0.0689	0.1178	0.2372
30.0000	0.0210	0.0700	0.1196	0.2399
31.0000	0.0219	0.0727	0.1245	--
32.0000	0.0221	0.0742	0.1260	--
33.0000	0.0227	0.0788	0.1284	--
34.0000	0.0230	0.0816	0.1301	--
35.0000	0.0231	0.0827	0.1312	--
36.0000	0.0234	0.0841	0.1341	--
37.0000	0.0239	0.0874	0.1409	--
38.0000	0.0242	0.0890	0.1453	--
39.0000	0.0247	0.0926	0.1541	--
40.0000	0.0249	0.0935	0.1556	--

Table C2: Fractional conversion (X) at different conditions Raw data for Figure 5.7

Run Time (min)	*H_2= 33%, I= 240 A P=12 kW*	*H_2= 33%, I= 280 A P=14 kW*	*H_2=45%, I= 240 A P=14 kW*
0.0000	0.0000	0.0000	0.0000
1.0000	2.1863e-3	4.2623e-3	4.0994e-3
2.0000	3.9627e-3	7.0023e-3	6.8323e-3
3.0000	7.7888e-3	0.0125	0.0120
4.0000	9.5652e-3	0.0152	0.0145
5.0000	0.0131	0.0201	0.0200
6.0000	0.0148	0.0224	0.0228
7.0000	0.0178	0.0263	0.0277
8.0000	0.0191	0.0285	0.0301
9.0000	0.0224	0.0333	0.0361
10.0000	0.0245	0.0356	0.0391
11.0000	0.0283	0.0402	0.0456
12.0000	0.0299	0.0425	0.0488
13.0000	0.0332	0.0467	0.0567
14.0000	0.0348	0.0493	0.0600
15.0000	0.0376	0.0548	0.0660
16.0000	0.0389	0.0578	0.0682
17.0000	0.0417	0.0642	0.0731
18.0000	0.0435	0.0670	0.0760
19.0000	0.0476	0.0709	0.0817
20.0000	0.0493	0.0725	0.0843
21.0000	0.0529	0.0761	0.0884
22.0000	0.0548	0.0792	0.0911
23.0000	0.0581	0.0865	0.0969
24.0000	0.0593	0.0895	0.0995
25.0000	0.0609	0.0947	0.1036
26.0000	0.0618	0.0971	0.1058
27.0000	0.0656	0.1032	0.1101
28.0000	0.0670	0.1073	0.1126
29.0000	0.0689	0.1161	0.1178
30.0000	0.0700	0.1207	0.1196
31.0000	0.0727	0.1271	0.1245
32.0000	0.0742	0.1300	0.1260
33.0000	0.0788	0.1355	0.1284
34.0000	0.0816	0.1393	0.1301
35.0000	0.0827	0.1406	0.1312
36.0000	0.0841	0.1430	0.1341
37.0000	0.0874	0.1494	0.1409
38.0000	0.0890	0.1537	0.1453
39.0000	0.0926	0.1616	0.1541
40.0000	0.0935	0.1632	0.1556

Table C3: Fractional conversion (X) at different conditions Raw data for Figure 5.8, up to 40 minutes

Run Time (min)	*H_2= 67% I= 240 A*	*H_2=67% CH4 added at 11 min.*	*H_2=67% Current lowered to 200 A at 17 min.*
0.0000	0.0000	0.0000	0.0000
1.0000	4.0994e-3	5.0176e-3	2.1864e-3
2.0000	8.6087e-3	9.7401e-3	6.0127e-3
3.0000	0.0190	0.0213	0.0164
4.0000	0.0243	0.0272	0.0210
5.0000	0.0353	0.0381	0.0312
6.0000	0.0403	0.0431	0.0366
7.0000	0.0512	0.0519	0.0478
8.0000	0.0570	0.0559	0.0534
9.0000	0.0687	0.0627	0.0633
10.0000	0.0728	0.0661	0.0676
11.0000	0.0791	0.0723	0.0775
12.0000	0.0823	0.0753	0.0827
13.0000	0.0883	0.0803	0.0955
14.0000	0.0937	0.0821	0.1022
15.0000	0.1129	0.0850	0.1134
16.0000	0.1211	0.0866	0.1203
17.0000	0.1388	0.0902	0.1326
18.0000	0.1470	0.0919	0.1388
19.0000	0.1566	0.0955	0.1470
20.0000	0.1611	0.0975	0.1498
21.0000	0.1726	0.1026	0.1541
22.0000	0.1776	0.1054	0.1559
23.0000	0.1864	0.1098	0.1595
24.0000	0.1921	0.1116	0.1617
25.0000	0.2033	0.1154	0.1649
26.0000	0.2096	0.1164	0.1663
27.0000	0.2208	0.1182	0.1693
28.0000	0.2263	0.1197	0.1707
29.0000	0.2372	0.1253	0.1748
30.0000	0.2399	0.1275	0.1782
31.0000	--	0.1299	0.1848
32.0000	--	0.1321	0.1875
33.0000	--	0.1392	0.1924
34.0000	--	0.1414	0.1945
35.0000	--	--	0.1958
36.0000	--	--	0.1977
37.0000	--	--	0.2010
38.0000	--	--	0.2031
39.0000	--	--	0.2074
40.0000	--	--	0.2095

Table C4: Fractional conversion (X) at different stoichiometries Raw data for Figure 5.9

Run Time (min)	*H_2=45%, P=14 kW 1CaO : 1.5C*	*H_2=45%, P=14 kW 1CaO : 3C*	*H_2=45%, P=14 kW 1CaO : 6C*
0.0000	0.0000	0.0000	0.0000
1.0000	2.8698e-3	4.0994e-3	5.3030e-3
2.0000	5.6291e-3	6.8323e-3	9.2803e-3
3.0000	0.0116	0.0120	0.0172
4.0000	0.0141	0.0145	0.0208
5.0000	0.0185	0.0200	0.0273
6.0000	0.0204	0.0228	0.0301
7.0000	0.0242	0.0277	0.0354
8.0000	0.0259	0.0301	0.0375
9.0000	0.0292	0.0361	0.0417
10.0000	0.0308	0.0391	0.0438
11.0000	0.0341	0.0456	0.0479
12.0000	0.0357	0.0488	0.0500
13.0000	0.0390	0.0567	0.0545
14.0000	0.0407	0.0600	0.0566
15.0000	0.0436	0.0660	0.0616
16.0000	0.0450	0.0682	0.0634
17.0000	0.0481	0.0731	0.0672
18.0000	0.0498	0.0760	0.0695
19.0000	0.0529	0.0817	0.0733
20.0000	0.0544	0.0843	0.0769
21.0000	0.0575	0.0884	0.0803
22.0000	0.0591	0.0911	0.0826
23.0000	0.0619	0.0969	0.0864
24.0000	0.0635	0.0995	0.0881
25.0000	0.0672	0.1036	0.0915
26.0000	0.0695	0.1058	0.0932
27.0000	0.0735	0.1101	0.0970
28.0000	0.0757	0.1126	0.0991
29.0000	0.0801	0.1178	0.1032
30.0000	0.0821	0.1196	0.1047
31.0000	0.0868	0.1245	0.1085
32.0000	0.0889	0.1260	0.1110
33.0000	0.0922	0.1284	0.1152
34.0000	0.0937	0.1301	0.1167
35.0000	0.0947	0.1312	0.1171
36.0000	0.0965	0.1341	0.1181
37.0000	0.0998	0.1409	0.1219
38.0000	0.1012	0.1453	0.1236
39.0000	0.1050	0.1541	0.1270
40.0000	0.1061	0.1556	0.1278

Table C5: Fractional conversion (X) for reaction with methane at different plasma powers Raw data for Figure 610

Run Time (min)	*H_2=33%, P=14 kW*	*H_2=45%, P=14 kW*	*H_2=67%, P=18 kW*
0.0000	0.0000	0.0000	0.0000
1.0000	1.4758e-3	2.9517e-3	3.9354e-3
2.0000	2.7056e-3	4.4275e-3	6.5590e-3
3.0000	5.1652e-3	7.7071e-3	0.0118
4.0000	6.3950e-3	9.5109e-3	0.0146
5.0000	8.8546e-3	0.0134	0.0202
6.0000	0.0101	0.0154	0.0230
7.0000	0.0125	0.0193	0.0282
8.0000	0.0138	0.0213	0.0307
9.0000	0.0162	0.0256	0.0362
10.0000	0.0175	0.0279	0.0394
11.0000	0.0199	0.0328	0.0459
12.0000	0.0212	0.0353	0.0495
13.0000	0.0233	0.0398	0.0571
14.0000	0.0244	0.0421	0.0612
15.0000	0.0268	0.0467	0.0703
16.0000	0.0280	0.0490	0.0748
17.0000	0.0305	0.0533	0.0820
18.0000	0.0317	0.0554	0.0839
19.0000	0.0339	0.0597	--
20.0000	0.0349	0.0618	--
21.0000	0.0371	0.0661	--
22.0000	0.0381	0.0682	--
23.0000	0.0403	0.0722	--
24.0000	0.0413	0.0741	--
25.0000	0.0435	0.0777	--
26.0000	0.0445	0.0795	--
27.0000	0.0467	0.0831	--
28.0000	0.0477	0.0849	--
29.0000	0.0495	0.0885	--
30.0000	0.0504	0.0893	--

Table C6: Fractional conversion (X) at different conditions for G-I and G-II Raw data for Figure 6.14 and Figure 6.15

Run Time (min)	*G-I P=12 kW*	*G-II P=12 kW*	*G-I P=16 kW*	*G-II P=16 kW*
0.0000	0.0000	0.0000	0.0000	0.0000
1.0000	2.1863e-3	1.6397e-3	2.7329e-3	2.7329e-3
2.0000	3.9627e-3	2.4596e-3	6.1491e-3	6.8323e-3
3.0000	7.7888e-3	4.0994e-3	0.0143	0.0178
4.0000	9.5652e-3	5.1925e-3	0.0182	0.0235
5.0000	0.0131	9.2919e-3	0.0258	0.0413
6.0000	0.0148	0.0107	0.0294	0.0515
7.0000	0.0178	0.0137	0.0365	0.0747
8.0000	0.0191	0.0159	0.0402	0.0876
9.0000	0.0224	0.0227	0.0462	0.1032
10.0000	0.0245	0.0276	0.0497	0.1137
11.0000	0.0283	0.0374	0.0568	0.1252
12.0000	0.0299	0.0424	0.0600	0.1323
13.0000	0.0332	0.0547	0.0660	0.1492
14.0000	0.0348	0.0604	0.0691	0.1582
15.0000	0.0376	0.0680	0.0782	0.1746
16.0000	0.0389	0.0719	0.0819	0.1816
17.0000	0.0417	0.0812	0.0895	0.1953
18.0000	0.0435	0.0854	0.0932	0.2022
19.0000	0.0476	0.0936	0.0992	0.2154
20.0000	0.0493	0.0984	0.1019	0.2212
21.0000	0.0529	0.1080	0.1090	0.2335
22.0000	0.0548	0.1120	0.1126	0.2387
23.0000	0.0581	0.1208	0.1200	0.2472
24.0000	0.0593	0.1252	0.1237	0.2492
25.0000	0.0609	0.1325	0.1324	--
26.0000	0.0618	0.1346	0.1383	--
27.0000	0.0656	--	0.1446	--
28.0000	0.0670	--	0.1469	--
29.0000	0.0689	--	0.1513	--
30.0000	0.0700	--	0.1533	--
31.0000	0.0727	--	0.1588	--
32.0000	0.0742	--	0.1615	--
33.0000	0.0788	--	0.1664	--
34.0000	0.0816	--	0.1699	--
35.0000	0.0862	--	0.1722	--
36.0000	0.0876	--	0.1774	--
37.0000	0.0909	--	0.1867	--
38.0000	0.0925	--	0.1925	--
39.0000	0.0961	--	0.2026	--
40.0000	0.0970	--	0.2074	--